872

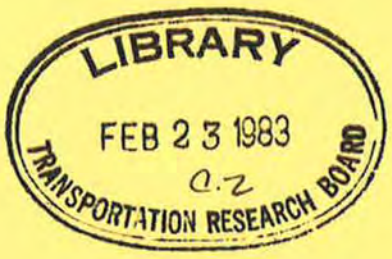

TRANSPORTATION
RESEARCH RECORD 872

Centrifuge-Soil Testing, Soil Mechanics, and Soil Properties

001411671
Transportation Research Record Issue:
872

TRB
TRANSPORTATION RESEARCH BOARD
NATIONAL ACADEMY OF SCIENCES

1982
TRANSPORTATION RESEARCH BOARD EXECUTIVE COMMITTEE

Officers

DARRELL V MANNING, *Chairman*
LAWRENCE D. DAHMS, *Vice Chairman*
THOMAS B. DEEN, *Executive Director*

Members

RAY A. BARNHART, JR., *Administrator, Federal Highway Administration, U.S. Department of Transportation* (ex officio)
FRANCIS B. FRANCOIS, *Executive Director, American Association of State Highway and Transportation Officials* (ex officio)
WILLIAM J. HARRIS, JR., *Vice President, Research and Test Department, Association of American Railroads* (ex officio)
J. LYNN HELMS, *Administrator, Federal Aviation Administration, U.S. Department of Transportation* (ex officio)
THOMAS D. LARSON, *Secretary of Transportation, Pennsylvania Department of Transportation* (ex officio, Past Chairman, 1981)
RAYMOND A. PECK, JR., *Administrator, National Highway Traffic Safety Administration, U.S. Department of Transportation* (ex officio)
ARTHUR E. TEELE, JR., *Administrator, Urban Mass Transportation Administration, U.S. Department of Transportation* (ex officio)
CHARLEY V. WOOTAN, *Director, Texas Transportation Institute, Texas A&M University* (ex officio, Past Chairman, 1980)

GEORGE J. BEAN, *Director of Aviation, Hillsborough County (Florida) Aviation Authority*
JOHN R. BORCHERT, *Professor, Department of Geography, University of Minnesota*
RICHARD P. BRAUN, *Commissioner, Minnesota Department of Transportation*
ARTHUR J. BRUEN, JR., *Vice President, Continental Illinois National Bank and Trust Company of Chicago*
JOSEPH M. CLAPP, *Senior Vice President and Member, Board of Directors, Roadway Express, Inc.*
ALAN G. DUSTIN, *President, Chief Executive, and Chief Operating Officer, Boston and Maine Corporation*
ROBERT E. FARRIS, *Commissioner, Tennessee Department of Transportation*
ADRIANA GIANTURCO, *Director, California Department of Transportation*
JACK R. GILSTRAP, *Executive Vice President, American Public Transit Association*
MARK G. GOODE, *Engineer-Director, Texas State Department of Highways and Public Transportation*
WILLIAM C. HENNESSY, *Commissioner of Transportation, New York State Department of Transportation*
LESTER A. HOEL, *Hamilton Professor and Chairman, Department of Civil Engineering, University of Virginia*
MARVIN L. MANHEIM, *Professor, Department of Civil Engineering, Massachusetts Institute of Technology*
FUJIO MATSUDA, *President, University of Hawaii*
DANIEL T. MURPHY, *County Executive, Oakland County, Michigan*
ROLAND A. OUELLETTE, *Director of Transportation Affairs for Industry-Government Relations, General Motors Corporation*
RICHARD S. PAGE, *General Manager, Washington (D.C.) Metropolitan Area Transit Authority*
MILTON PIKARSKY, *Director of Transportation Research, Illinois Institute of Technology*
GUERDON S. SINES, *Vice President, Information and Control Systems, Missouri Pacific Railroad*
JOHN E. STEINER, *Vice President, Corporate Product Development, The Boeing Company*
RICHARD A. WARD, *Director-Chief Engineer, Oklahoma Department of Transportation*

The **Transportation Research Record** series consists of collections of papers in a given subject. Most of the papers in a Transportation Research Record were originally prepared for presentation at a TRB Annual Meeting. All papers (both Annual Meeting papers and those submitted solely for publication) have been reviewed and accepted for publication by TRB's peer review process according to procedures approved by a Report Review Committee consisting of members of the National Academy of Sciences, the National Academy of Engineering, and the Institute of Medicine.

The views expressed in these papers are those of the authors and do not necessarily reflect those of the sponsoring committee, the Transportation Research Board, the National Academy of Sciences, or the sponsors of TRB activities.

Transportation Research Records are issued irregularly; approximately 50 are released each year. Each is classified according to the modes and subject areas dealt with in the individual papers it contains. TRB publications are available on direct order from TRB, or they may be obtained on a regular basis through organizational or individual affiliation with TRB. Affiliates or library subscribers are eligible for substantial discounts. For further information, write to the Transportation Research Board, National Academy of Sciences, 2101 Constitution Avenue, N.W., Washington, DC 20418.

TRANSPORTATION RESEARCH RECORD 872

Centrifuge-Soil Testing, Soil Mechanics, and Soil Properties

TRANSPORTATION RESEARCH BOARD

NATIONAL RESEARCH COUNCIL

NATIONAL ACADEMY OF SCIENCES
WASHINGTON, D.C. 1982

Transportation Research Record 872
Price $10.40
Edited for TRB by Naomi Kassabian

modes
1 highway transportation
3 rail transportation

subject area
63 soil and rock mechanics

Library of Congress Cataloging in Publication Data
National Research Council. Transportation Research Board.
Centrifuge-soil testing, soil mechanics, and soil properties.

(Transportation research record; 872)
1. Soils–Testing–Addresses, essays, lectures. 2. Soil mechanics–Addresses, essays, lectures. I. National Research Council (U.S.). Transportation Research Board. II. Series.
TE7.H5 no. 872 [TA710.5] 380.5s [624.1'51] 83-2232
ISBN 0-309-03401-9 ISSN 0361-1981

Sponsorship of the Papers in This Transportation Research Record

GROUP 2–DESIGN AND CONSTRUCTION OF TRANSPORTATION FACILITIES
R. V. LeClerc, consultant, Olympia, Washington, chairman

Evaluations, Systems, and Procedures Section
Charles S. Hughes III, Virginia Highway and Transportation Research Council, chairman

Committee on Mineral Aggregates
T. Paul Teng, Federal Highway Administration, chairman
Grant J. Allen, David A. Anderson, Gordon W. Beecroft, Robert J. Collins, Sabir H. Dahir, Stephen W. Forster, Richard D. Gaynor, David L. Gress, Donn E. Hancher, Robert F. Hinshaw, William W. Hotaling, Jr., Eugene Y. Huang, Richard C. Ingberg, William B. Ledbetter, Donald W. Lewis, Charles R. Marek, Vernon J. Marks, John T. Paxton, Hisao Tomita, Richard D. Walker

Soil Mechanics Section
Lyndon H. Moore, New York State Department of Transportation, chairman

Committee on Mechanics of Earth Masses and Layered Systems
Robert D. Stoll, Columbia University, chairman
Dimitri Athanasiou-Grivas, Walter R. Barker, Richard D. Barksdale, Jerry C. Chang, Umakant Dash, Milton E. Harr, Gerald P. Raymond, Surendra K. Saxena, Robert L. Schiffman, Harvey E. Wahls, John L. Walkinshaw, William G. Weber, Jr., T. H. Wu

Geology and Properties of Earth Materials Section
David L. Royster, Tennessee Department of Transportation, chairman

Committee on Soil and Rock Properties
C. William Lovell, Purdue University, chairman
C. O. Brawner, William F. Brumund, Carl D. Ealy, James P. Gould, Ernest Jonas, T. Cameron Kenney, Charles C. Ladd, Gerald P. Raymond, Robert L. Schiffman, Hassan A. Sultan, William D. Trolinger, David J. Varnes, Harvey E. Wahls, John L. Walkinshaw

Committee on Frost Action
Wilbur M. Haas, Michigan Technological University, chairman
Stephen A. Cannistra, Jorge L. Cowley, Barry J. Dempsey, Paul J. Diethelm, Albert F. Dimillio, Wilbur J. Dunphy, Jr., David C. Esch, Philip F. Frandina, Gary L. Hoffman, Glenn E. Johns, Thaddeus C. Johnson, R. H. Jones, Hiroshi Kubo, Clyde N. Laughter, C. William Lovell, George W. McAlpin, Richard W. McGaw, Robert G. Packard, Alex Rutka

John W. Guinnee, Transportation Research Board staff

Sponsorship is indicated by a footnote at the end of each report. The organizational units, officers, and members are as of December 31, 1981.

Contents

PHYSICAL MODELING OF CLAY SLOPES IN THE DRUM CENTRIFUGE
James A. Cheney and Ali Mohamad Oskoorouchi 1

CENTRIFUGAL TESTING OF SOIL SLOPE MODELS
Myoung Mo Kim and Hon-Yim Ko 7

RECTANGULAR OPEN-PIT EXCAVATIONS MODELED IN GEOTECHNICAL CENTRIFUGE
O. Kusakabe and A.N. Schofield 15

PRELIMINARY INVESTIGATION OF BEARING CAPACITY OF LAYERED SOILS BY CENTRIFUGAL MODELING
A.C. Herdy and F.C. Townsend 20

FIELD-PERFORMANCE COMPARISON OF TWO EARTHWORK REINFORCEMENT SYSTEMS
Joseph B. Hannon, Raymond A. Forsyth, and Jerry C. Chang 24

DESIGN AND CONSTRUCTION OF FABRIC-REINFORCED RETAINING WALLS BY NEW YORK STATE
Gary E. Douglas 32

STABILIZATION OF WEDGE FAILURE IN ROCK SLOPE
Duncan C. Wyllie 37

REPETITIVE-LOAD BEHAVIOR OF UNSATURATED SOILS
E. Sabri Motan and Tuncer B. Edil 41

SOLAR RADIATION EFFECTS ON FROST ACTION IN SOILS
Chester W. Jones 49

FACTORS AFFECTING COATING OF AGGREGATES WITH PORTLAND CEMENT
O.E.K. Daoud, H.R. Guirguis, and S.K. Hamdani 56

ROCK AGGREGATE MANAGEMENT PLANNING FOR ENERGY CONSERVATION: OPTIMIZATION METHODOLOGY
Fong-Lieh Ou, Wallace Cox, and Lee Collett 63

SOIL SUPPORT VALUE–A NEW HORIZON
Gilbert Y. Baladi and Tesfai Goitom 69

Authors of the Papers in This Record

Baladi, Gilbert Y., Department of Civil Engineering, Michigan State University, East Lansing, MI 48824; formerly with Federal Highway Administration, Washington, DC

Chang, Jerry C., Sacramento Municipal Utilities District, Engineering Department, 6201 S Street, Sacramento, CA 95819

Cheney, James A., Department of Civil Engineering, University of California, Davis, CA 95616

Collett, Lee, Gifford Pinchot National Forest, Forest Service, United States Department of Agriculture, 500 West 12th Street, Vancouver, WA 98660

Cox, Wallace, Gifford Pinchot National Forest, Forest Service, United States Department of Agriculture, 500 West 12th Street, Vancouver, WA 98660

Daoud, O.E.K., c/o Mr. Sadi Farwana, Ministry of Public Works, Kuwait

Douglas, Gary E., New York State Department of Transportation, 1220 Washington Avenue, Albany, NY 12232

Edil, Tuncer B., Department of Civil and Environmental Engineering, University of Wisconsin-Madison, Madison, WI 53706

Forsyth, Raymond A., Department of Transportation, 5900 Folsom Boulevard, P.O. Box 19128, Sacramento, CA 95819

Goitom, Tesfai, Department of Civil Engineering, California State University, Long Beach, CA 90840

Guirguis, H.R., P.O. Box 8021, Salmya, Kuwait

Hamdani, S.K., P.O. Box 8021, Salmya, Kuwait

Hannon, Joseph B., Department of Transportation, 5900 Folsom Boulevard, P.O. Box 19128, Sacramento, CA 95819

Herdy, A.C., Department of Civil Engineering, University of Florida, Gainesville, FL 32611

Jones, Chester W., Bureau of Reclamation, U.S. Department of the Interior, P.O. Box 25007, Building 67, Denver Federal Center, Denver, CO 80225

Kim, Myoung Mo, Seoul National University, Seoul, South Korea

Ko, Hon-Yim, Department of Civil, Environmental, and Architectural Engineering, University of Colorado, Campus Box 428, Boulder, CO 80309

Kusakabe, O., Engineering Department, Trumpington Street, Cambridge University, Cambridge CB2 1PZ, England

Motan, E. Sabri, Department of Civil and Environmental Engineering, Clarkson College of Technology, Potsdam, NY 13676

Oskoorouchi, Ali Mohamad, Department of Civil Engineering, Kerman University, Kerman, Iran

Ou, Fong-Lieh, Gifford Pinchot National Forest, Forest Service, United States Department of Agriculture, 500 West 12th Street, Vancouver, WA 98660

Schofield, A.N., Engineering Department, Trumpington Street, Cambridge University, Cambridge CB2 1PZ, England

Townsend, F.C., Department of Civil Engineering, University of Florida, Gainesville, FL 32611

Wyllie, Duncan C., Golder Associates, 224 West 8th Avenue, Vancouver, B.C., Canada

Physical Modeling of Clay Slopes in the Drum Centrifuge

JAMES A. CHENEY AND ALI MOHAMAD OSKOOROUCHI

The modeling-of-models technique is used in the physical modeling of overconsolidated kaoline clay embankments by utilizing a drum centrifuge. The clay is consolidated from a slurry in a *g*-field up to 400 times gravity, and then 60° slope embankments from 2 to 8 cm in height are cut and tested for the failure *g*-level. Three types of failure are observed: (a) a quick strength, wherein the *g*-level is raised quickly to failure; (b) a short-term strength, wherein failure takes place in 5-10 min; and (c) long-term failures, which take many hours. The extension of these data to prototype size is tentatively established by tests that vary over a range of scales. This is especially important in establishing a scaling relationship for time. The time-scaling relationship is investigated by observing changes in time to failure as a function of model size for constant prototype dimensions.

The stability of overconsolidated clay slopes was physically modeled by Fragaszy and Cheney (1,2) in a drum centrifuge, shown in Figure 1. Their results indicated that the short-term strength of the slope can be assessed by using the Cam-Clay theory for the yield surface on the dry side of the critical-state line. It was also shown that lower strengths are exhibited in the centrifuge models after a long time (1-12 h) at constant g-level. This experimental finding suggests that it might be possible to model a phenomenon observed in prototype slopes of overconsolidated clay, that of slopes failing after many years of stabile behavior. The results reported (1), however, were not sufficient to establish a scaling relationship between time in the centrifuge and prototype time.

The approach used by Fragaszy and Cheney in centrifuge modeling was to analyze the centrifuge results with a Bishop's-method stability-analysis program by using various choices for the strength parameters. The strength parameters giving factors of safety closest to unity were considered to be closest to correct.

Another approach in centrifuge modeling is to test models over a range of scales to establish the range of validity of the technique and then to make predictions by direct modeling. This approach has been quite successful in applications involving sand (3-5). The application in clay is more complicated because density and water content are self-controlled phenomena in the sense that consolidation depends on internal properties of permeability, compressibility, and viscosity rather than externally controlled deposition. Thus the use of the modeling-of-models technique in clay requires special attention to the initial states of stress and moisture-content distribution in order to satisfy the requirements of similarity between test specimens.

DRUM CENTRIFUGE

The use of a complete drum for modeling clay slopes has many advantages. It permits the consolidation of clay at extremely high g-levels, and the usual problem of balancing the arm while water is removed in the consolidation process is automatically solved by symmetry. The drum forms its own counterbalance. It permits the study of stability of slopes having no unnatural boundary along their length. However, there are some drawbacks associated particularly with the drum centrifuge that must be addressed.

The drum centrifuge used in this study rotates in a vertical plane and has a very short length (0.3 m) and a radius of 0.6 m. The clay is poured into the drum while the drum is spinning and spreads evenly along the circumference, forming a uniformly thick blanket of clay 0.3 m wide and 0.15 m thick. This blanket is then consolidated under its own weight at 50-400 g by the spinning of the drum. The state of stress during consolidation is in question.

As the layers near the wall of the drum compact, the inner layers must move radially outward. This outward movement must also be accompanied by a circumferential spreading because the layer is moving to a larger radius associated with a larger circumference. The ends of the drum (0.3 m apart) have a camber θ inward with respect to the plane of rotation so that there must also be an out-of-plane spreading of inner layers as well. The geometry of the drum is shown in Figure 2.

The lateral strains associated with consolidation may be computed from the geometry, the measured inner surface displacement, and the change in water content across the thickness. The radial strain at a given layer is given by the following:

$$\epsilon_v = [\delta v - (d/R^*) - (d/R) + (d^2/RR^*)]/[1 - (d/R^*) - (d/R) + (d^2/RR^*)] \quad (1)$$

in which

$$\delta v = \text{volume change in a layer at depth } d = G_s (w_i - w_f)/(1 + G_s w_i) \quad (2)$$

where

w_i = water content at layer d initially as ratio of dry weight,
w_f = water content at layer d finally,
G_s = specific gravity of clay particles,
R^* = radius of layer from apex of end walls (see Figure 2b),
R = radius of layer from center of revolution of drum (see Figure 2a), and
d = radial displacement of layer.

The displacement d of the surface layer is measured. From this, $\epsilon_v \Delta y$ is subtracted to obtain the displacement d of the second layer. This process has been programmed for high-speed digital computation to determine the displacement distribution and then the lateral strain.

The lateral strain for one test (M-2) is shown in Figure 3. The conditions near the outer wall approach zero lateral strain while conditions near the inner soil surface approach strains large enough to reach the active lateral stress state.

WATER-CONTENT DISTRIBUTION

The influence of the variable lateral strain on the water-content distribution through the sample can be assessed by use of the Cam-Clay theory (6). If we take

$$\sigma_h' = K \sigma_v' \quad (3)$$

where

σ_v' = effective stress in y-direction (radial),
σ_h' = effective stress in x, z-directions (lateral), and
K = coefficient of lateral pressure,

Figure 1. Drum centrifuge and peripheral equipment.

Figure 2. (a) Axial view of drum and (b) X-section of drum, A-A.

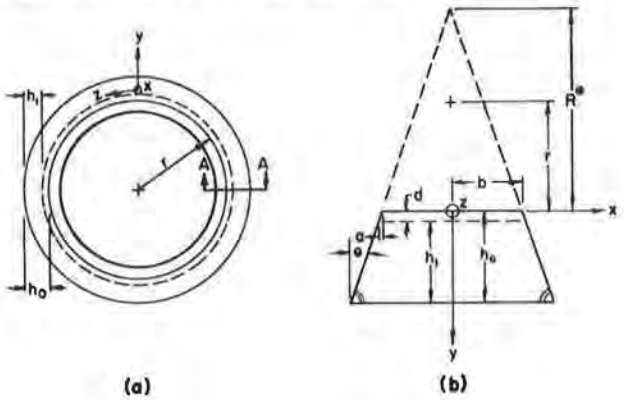

in accordance with the Cam-Clay theory,

$$v = V - \lambda \ell n p' - \{[(\lambda - \kappa)/M]/(q/p')\} \quad (4)$$

where v is the volume of a unit volume of solids,

$$q = \sigma_v' - \sigma_h' = (1 - K)\,\sigma_v' \quad (5)$$

$$p' = (\sigma_v + 2\sigma_h)/3 = [(1 + 2K)/3]/\sigma_v' \quad (6)$$

and V, λ, κ, and M are constants of the theory.

The difference in v for K_o conditions (zero lateral strain) and K_a conditions (active Rankine state) is given by the following:

$$\Delta v = v_a - v_o = \lambda \ell n\,[(1 + 2K_o)/(1 + 2K_a)] + [(\lambda - \kappa)/M]\,3\,[(1 - K_o)/(1 + 2K_o)] - [(1 - K_a)/(1 + 2K_a)] \quad (7)$$

Given λ = 0.056, κ = 0.010, M = 1.27, K_o = 0.5, and K_a = 0.30, the following holds:

$$\Delta v = -0.10 \quad (8)$$

This means that the specific volume for the active Rankine state is less than that for the at-rest state. A smaller specific volume is associated with a smaller water content through the following:

$$\text{water content} = [(v - 1)/G_s] \times 100 \text{ percent} \quad (9)$$

Figure 4 shows schematically the water-content distribution with respect to depth for the K_a (active) and K_o (at-rest) states. The actual

Figure 3. Lateral strain versus depth after consolidation.

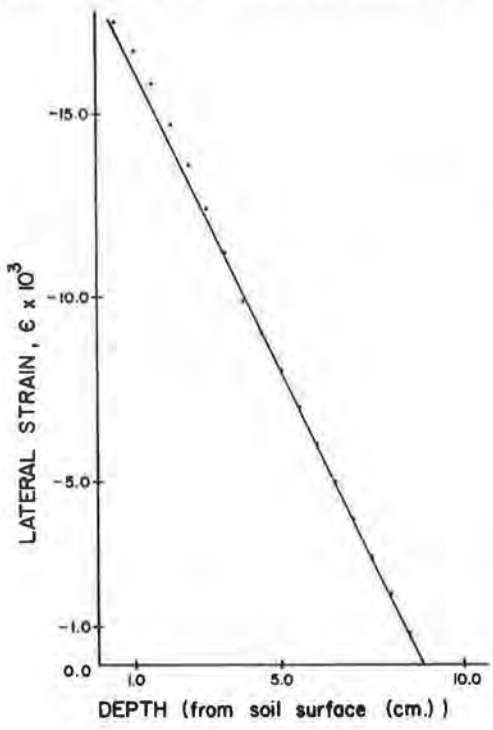

Figure 4. Expected W/C distribution for consolidated soil in drum.

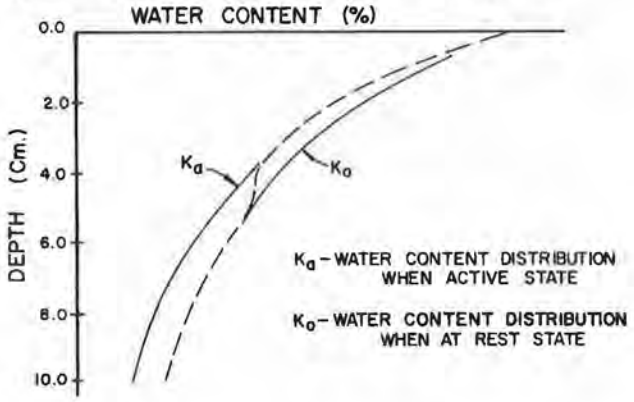

distribution follows the K_a-curve in the upper 4 cm of depth and follows the K_o-distribution in the lower 4 cm. A transition occurs between these two zones, forming an S shape.

DESCRIPTION OF TESTS

After consolidation of a clay blanket approximately 9 cm thick, the centrifuge is brought to a stop in order to take moisture-content samples. After this the centrifuge is spun up to the full consolidation speed to return the specimen to the fully consolidated state. Then the centrifuge is slowed to 40-50 rpm and a cutting is made by using a specially shaped cutting tool made of a sharpened wire bent to conform to the shape of the desired slope. The duration of time taken to cut the slope assures that the material is in the fully drained condition after cutting.

The control of the cutting is accomplished by means of a screw-fed rigid bracket to which the

cutting tool is affixed. This mechanism can be seen in Figure 1.

In the quick tests, the centrifuge is then steadily increased in speed, while the circumference is panned with a strobotac triggered by a photo cell that uses a light beam reflected from a target attached to the drum. The speed at which the first sign of a slope failure is observed defines the failure speed and the associated load factor at failure N_f.

The quick tests are essentially undrained tests due to the rapid rate of loading, although the analytical results of Fragaszy and Cheney (1) indicate that local dilation may occur at failure. Because the lateral stresses normal to the plane of rotation and the vertical stresses due to self-weight are greatly reduced, the sample is in a highly overconsolidated state. The quick tests are analogous in many respects to a quick draw-down test of a canal embankment.

Timed tests were performed once the quick-test strength had been established. These tests are performed in a similar manner, except the centrifuge speed is set at a percentage of the speed at quick slope failure and the time required to reach failure is observed. Two classes of time behavior are observed: (a) a short-term failure requiring 5-10 min and (b) a long-term failure requiring many hours.

All the slopes tested were at a 60° angle with respect to the horizontal and made of a mixture of kaoline particle sizes (25 percent Mono 90, 75 percent Snow Cal 50) having Cam-Clay properties λ = 0.056, κ = 0.010, and M = 1.27 and Mohr-Coulomb strength parameters c' = 0.1 kg/cm² and ϕ' = 33°.

MODELING OF MODELS

It has been stated (3) that the first task of an experimenter is to determine the range of validity of similitude in modeling whenever all the parameters characterizing a prototype are not exactly similar. In the current problem the particle size of the model material is taken as the same throughout the tests at various scales and there is a limit to the size of the model because of the finite length of the drum (0.3 m).

However, it is important also to maintain similarity between model and prototype wherever feasible. Because the strength and deformation characteristics of clay are strongly dependent on the water content, the water-content distribution is an important factor in establishing similarity. The water-content data plotted in Figure 5 were obtained from seven tests, all having the same prototype height but ranging in model height from 2 cm to 8 cm. In order to establish this similarity, it was found necessary to consolidate at the consolidation load factor N_c for 3 h with double drainage, top and bottom.

In order to establish a systematic schedule of quick tests, the array of tests shown in Figure 6 was projected. A prototype height (H_{pc}) of 400 cm was chosen for a series of seven model heights, after which tests of six different prototype heights were made at a single model height (5 cm).

The results of these tests are given in Table 1. If scaling is valid, all the tests at the same consolidation prototype height should fail at the same slope prototype height. In Figure 7 the failure prototype heights versus model heights are plotted. The range of consistent results is between 4 and 7 cm.

The divergence of the results for the 8-cm model height appears to be related to the fact that the water content is less than expected for the given consolidation load factor N_c. The reason for the divergence at the lower model heights is not clear but may be related to the size of clay conglomerates within the clay mass rather than the size of individual clay particles, and the water-content distribution is significantly different in shape at these lesser model heights.

With the valid range of model height established, a model height midway within this range was chosen for tests of other prototype heights. A plot of these results is given in Figure 8, which shows an almost linear relationship between prototype failure height and prototype consolidation height (H_{pc}).

The exception to this trend is test M-25, which, if the line is correct, failed prematurely. This result is explained by the fact that the water-content values for M-25 for some reason were greater than those of M-24, which was consolidated at N_c = 200. Thus, from the water-content data, M-25 should be associated with an N_c < 175 and is then in line with the other data points. The water-content plots are given in Figure 9. This observation makes clear that the fundamental parameter in assessing strength of these embankments is the water-content distribution rather than N_c. The relation developed between consolidation load factors N_c and failure load factors N_f is simply a convenience for presentation of results.

The relationship of Figure 9 is as follows:

$$H_{p_f} = 140 + 0.24H_{pc} \quad (10)$$

TIMED TESTS

The initial purpose of the long-duration tests was to establish the length of time necessary (if finite) for a slope lower than its quick-test failure height to fail. Early in the study, it was discovered that there were two types of time-to-failure data, as previously mentioned: a short-term failure requiring 5-10 min to develop and a truly long-term failure requiring many hours.

Table 2 lists the data from the timed tests and these data are plotted in Figure 10 along with the quick-test data for reference. There is a zone of prototype heights in which slopes will fail in a very short period of time. To the right of this zone, the time to failure dramatically increases. Isochrones of failure heights to consolidation heights are developed in the long-term-failure zone.

A cross plot of curves in Figure 10 is shown in Figure 11 that results in a family of time-to-failure lines for constant prototype consolidation height ($N_c \cdot H_m$). These lines are not valid to the left of the dashed line, which represents the boundary between short-term failure and long-term failure.

The test results shown in Figures 10 and 11 are all for a common model height of 5 cm. In order to establish a relationship between the time to failure in the model and time to failure in a prototype, tests over a range of model heights must be performed. To this end, a test series in Table 3 was carried out at a constant prototype height of slope H_{pF} and prototype height in consolidation H_{pc} but with model heights H_m ranging from 4.5 cm to 7.0 cm. The load factors at failure, of course, vary from 98.3 to 63.2.

If the time delay to failure depends on a dispersive phenomenon such as the hydrodynamic delay in consolidation, one would expect the time to be governed by a time factor T, which is proportional to the inverse square of the characteristic length H and directly proportional to time t:

$$T = C_v t/H^2 \quad (11)$$

Figure 5. Water content versus depth in modeling of models.

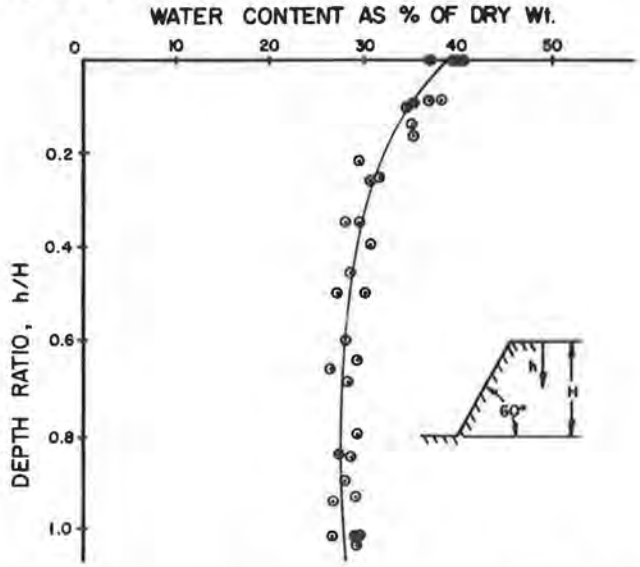

Table 1. Modeling-of-model data.

Test	H_m (cm)	N_c	H_{pc} (cm)	N_f	H_{pf} (cm)
M-11	2.0	200	400	167	334
M-12	3.5	114	400	55.2	193
M-13	4.0	100	400	63.4	253
M-14	5.0	80	400	47.3	236
M-15	6.0	66.7	400	39.4	236
M-16	7.0	57.0	400	34.9	244
M-17	8.0	50.0	400	37.6	301
M-21[a]	5.0	80	400	47.3	236
M-22	5.0	100	500	52.4	262
M-23	5.0	150	750	60.7	303
M-24	5.0	200	1000	78.0	390
M-25	5.0	250	1250	70.0	350
M-26	5.0	350	1750	110.0	550

[a]Test M-21 is the same as test M-14.

Figure 6. Modeling-of-model test program.

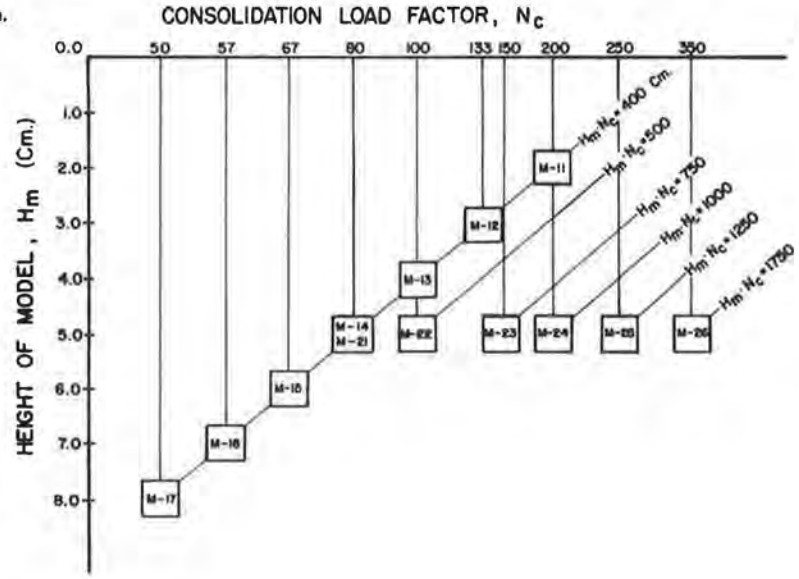

Figure 7. Prototype versus model height for modeling-of-model tests.

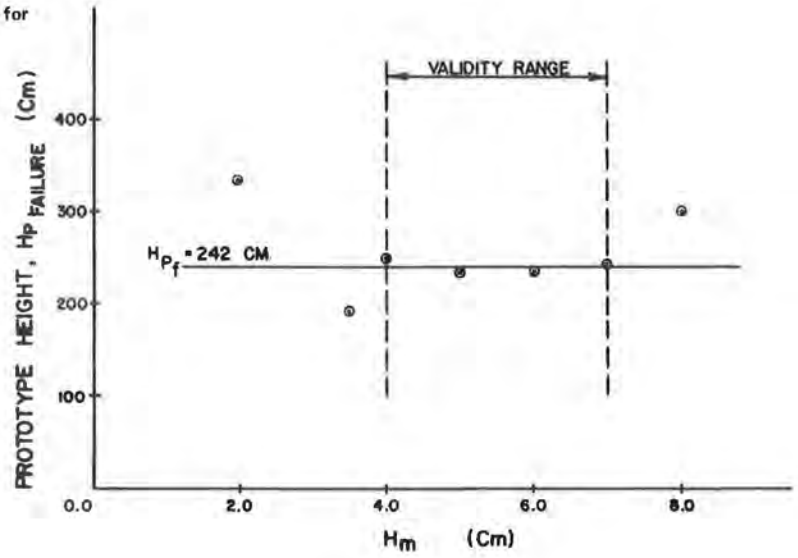

Figure 8. Prototype failure height versus prototype consolidation height for quick tests.

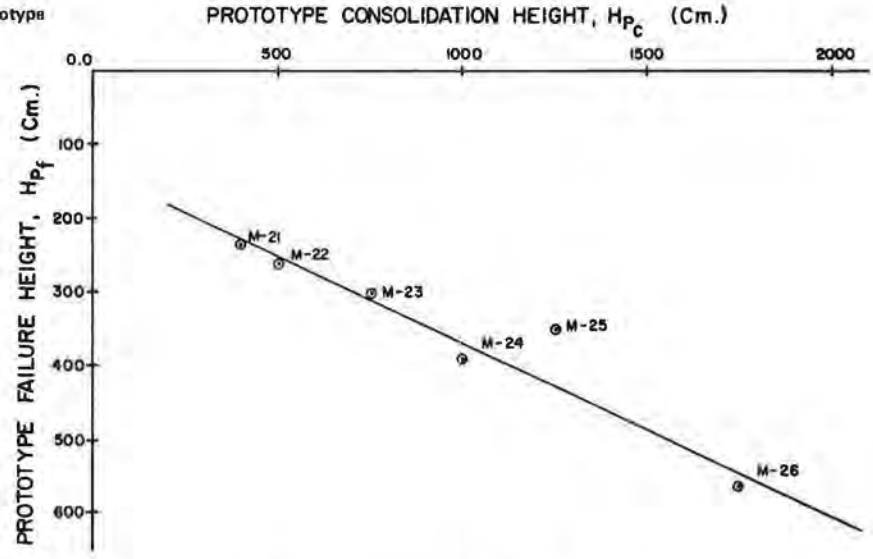

Figure 9. Water-content distribution: quick tests.

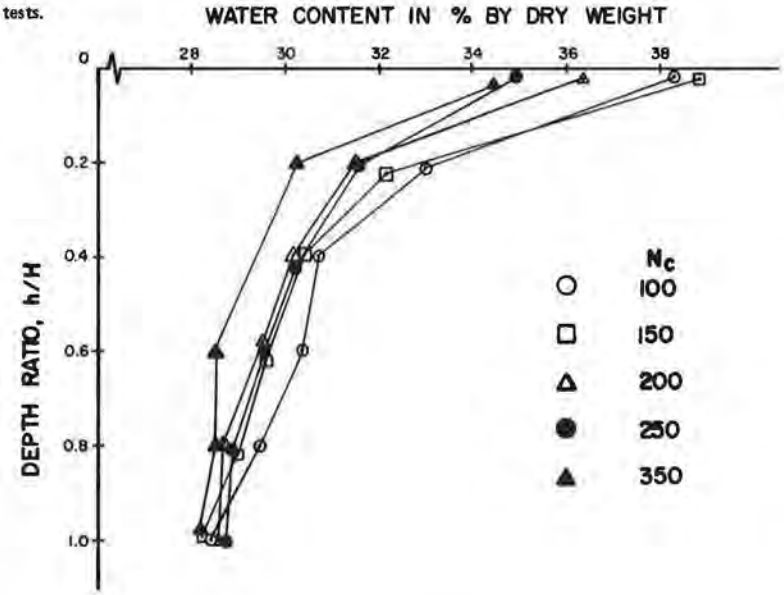

Table 2. Timed-test data.

Test	N_c	H_{pc} (cm)	N_f'	H_{pF} (cm)	t_F (min)
M-36	350	1750	88.5	442	150
M-36A	350	1750	77.0	385	310
M-36B	350	1750	54.5	272.5	520
M-35	250	1250	68.0	340	295
M-34	200	1000	59.0	295	5-10
M-34A	200	1000	45.0	225	5-10
M-34B	200	1000	39.3	196	510
M-33	150	750	21.0	105	5

Note: H_m = 5.0 cm.

where C_v is a constant.

The tests in Table 3 were run with constant prototype height; thus,

$$n_f' H_m = 1750 \text{ cm} \quad (12)$$

and

$$n_f'^2 = \overline{1750}^2/H_m^2 \quad (13)$$

The relation between t and n_f becomes the following:

$$t_f = [T(1750)^2/C_v]/(1/n_f'^2) \quad (14)$$

A plot of the inverse square of failure load factor n_f' versus time to failure is given in Figure 12. There is a fair correlation of the data with the theoretical line, and this tends to corroborate Skempton's hypothesis (7) for the time delay to failure. An extrapolation to a load factor of unity gives an estimate of the long-term time to failure of the prototype.

CONCLUSIONS

The existence of the short-term failure is of great

Figure 10. Results of timed tests.

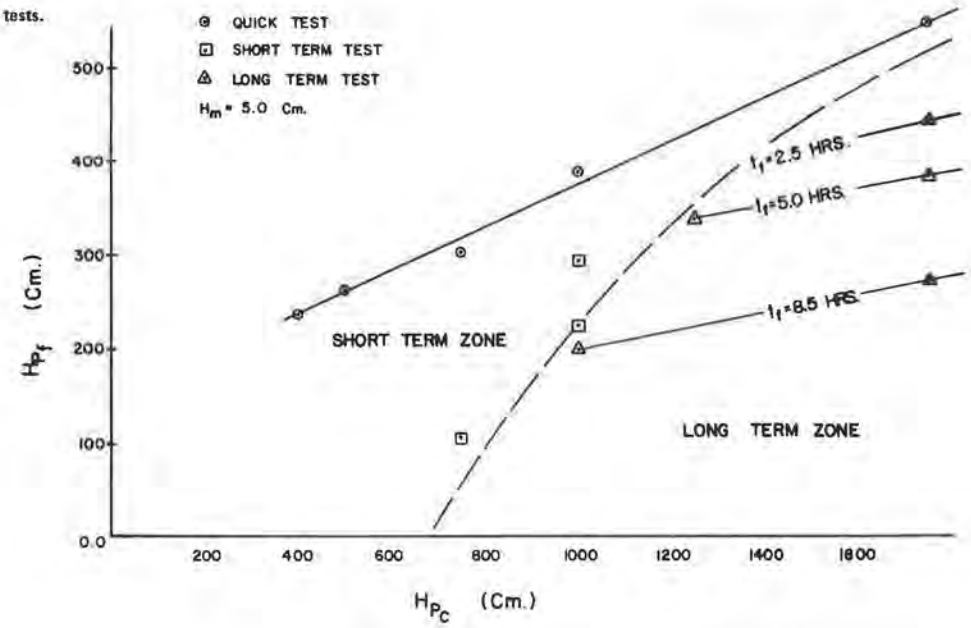

Figure 11. Time to failure (5-cm models).

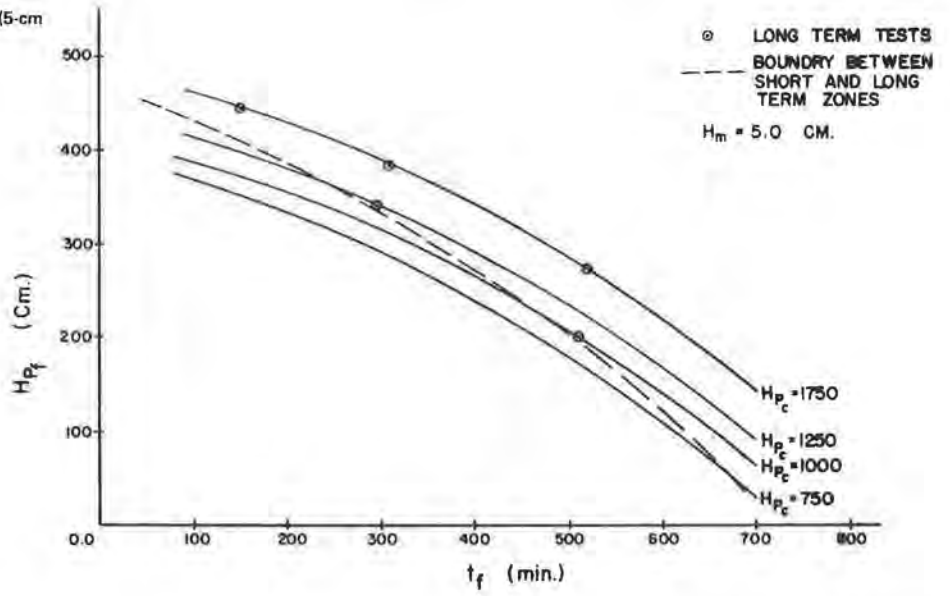

Table 3. Long-term modeling-of-model test data.

Test	H_m (cm)	N_c	H_{P_c}	N_f'	H_{P_F}	t_F (min)
M-41	4.5	389	1750	98.3	442	10
M-42	5.0	350	1750	88.5	442	150
M-43	5.3	330	1750	83.4	442	88
M-44	5.54	318	1750	80.3	442	72
M-46	7.0	250	1750	63.2	442	180

importance in assessment of the safety of slopes. This failure condition is likely associated with a local instability along a failure surface within the clay mass that permits a very localized dilation, leading to a fully softened state (critical state). The existence of this form of failure is suggested by Schofield and Wroth (6) as a mechanism of failure below the yield surface on the dry side of the critical state.

Apparently the quick tests generally were done so fast that such instabilities did not have time to develop, although some scatter in the data might be suggestive of such a reduction in strength.

The long-term behavior clearly exists in the model tests and time to failure increases with the size of the model. This result negates a viscoplastic creep theory (8) as an explanation of the delayed time to failure, which would make modeling invalid. The N^2-scaling law used in scaling time for hydrodynamic events (seepage, consolidation) appears to govern generally the delay time to failure and therefore corroborates the theory of Skempton (7).

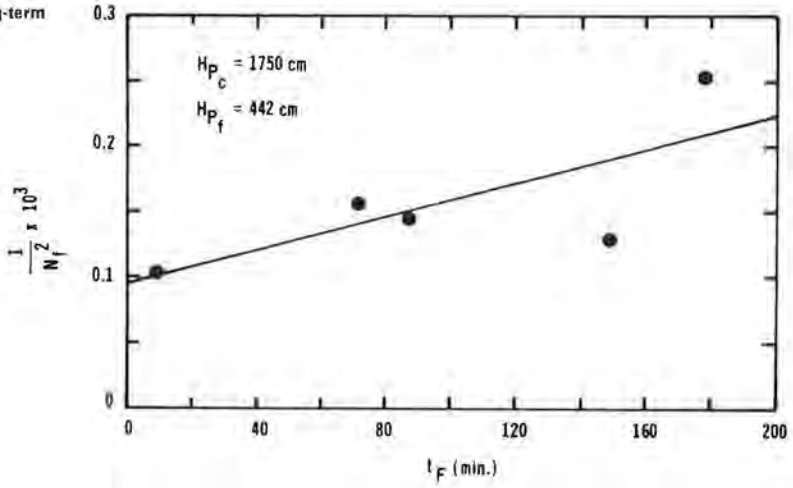

Figure 12. Time to failure versus $1/N_f^2$ for long-term modeling-of-model test.

REFERENCES

1. R. Fragaszy and J.A. Cheney. Drum Centrifuge Studies of Overconsolidated Slopes. Journal of Geotechnical Engineering Division of ASCE, Vol. 107, No. GT7, 1981, pp. 843-858.
2. R. Fragaszy. Drum Centrifuge Studies of Overconsolidated Clay Slopes. Univ. of California, Davis, Ph.D. dissertation, 1979.
3. N. Krebs-Ovesen. Centrifuge Testing Applied to Bearing Capacity Problems of Footings on Sand. Geotechnique, Vol. 25, 1975, pp. 344-401.
4. N. Krebs-Oveson. The Scaling Law Relationships. Proc., Seventh European Conference on Soil Mechanics and Foundation Engineering, Brighton, England, 1979, Vol. 4, pp. 319-323.
5. N. Krebs-Oveson. Centrifuge Tests to Determine the Uplift Capacity of Anchor Slabs in Sand. Proc., 10th International Conference on Soil Mechanics and Foundation Engineering, Stockholm, Sweden, 1981.
6. A.N. Schofield and C.P. Wroth. Critical State Soil Mechanics. McGraw-Hill, London, 1968.
7. A.W. Skempton. Slope Stability of Cuttings in Brown London Clay. Proc., Ninth International Conference on Soil Mechanics and Foundation Engineering, Tokyo, Vol. 3, Special Lectures, 1977, pp. 261-270.
8. J.D. Nelson and E.G. Thompson. A Theory of Creep Failure in Overconsolidated Clay. Journal of the Geotechnical Engineering Division of ASCE, Vol. 103, No. GT11, 1977, pp. 1281-1294.

Publication of this paper sponsored by Committee on Mechanics of Earth Masses and Layered Systems.

Centrifugal Testing of Soil Slope Models

MYOUNG MO KIM AND HON-YIM KO

The principles of testing static geomechanical models are explained, and the need to simulate the gravity-induced body forces is emphasized. The only convenient method of inducing increased gravity on models of soil structures is to spin the model in a centrifuge. Experiments were conducted in a 10-*g*-ton geotechnical centrifuge to model the stability of slopes of partly saturated granular soils. A series of modeling-of-models tests was conducted in which several models of different scales were tested at different gravity scales. The internal consistency of the centrifugal modeling technique is demonstrated by results of these tests, which show that the same critical height of the prototype slope is obtained irrespective of model scale. A quantitative comparison is made of the model test data and analytical results from limit analysis, finite-element analysis, and limiting-equilibrium analysis. It is demonstrated that the critical slope heights obtained from the centrifuge tests are bracketed within the upper bounds established by limit analysis and the lower bounds obtained from finite-element calculations. In addition, the locations of the failure surface obtained by testing and analysis correspond closely in all cases.

Testing of scaled earth models under an increased gravitational body force field is a relatively new idea in soil mechanics. This centrifugal-modeling technique is the only method that can completely satisfy the requirements of the principles of similitude in the geotechnical model in which body forces of a structure are significant. Nevertheless, many workers are still unconvinced of the validity of the method, primarily due to the lack of prototype data against which model behavior can be compared. Even when such data are available, comparisons usually point out the necessity to better define the geology of the prototype situation as well as the material properties.

In order to demonstrate that the scaled centrifugal model can project to prototype behavior, it is possible to carry out a modeling of models, in which a series of models is constructed at different scales, all representing the same prototype (which could be an imaginary situation), and tested at different gravity ratios, each calculated to bring the respective model to full similitude with the prototype. Only when it has been demonstrated that

Figure 1. Failure envelope and stress-strain curves of prototype and model materials.

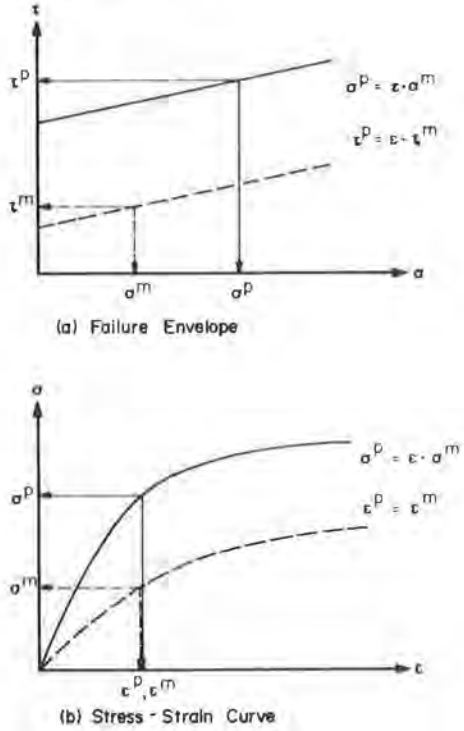

all models produce the same prototype projections can it be considered that the scaling relations obtained from the principles of similitude are valid and are therefore invariant with respect to the model scale. A homogeneous slope of granular soil is chosen to be the test model in this investigation. Three series of slope models of different sizes that had similar geometry were built and tested in a centrifuge.

After the concept of the modeling of models has been confirmed by using the slope model, the next step is to compare the self-consistent results of the centrifuge tests with the solutions obtained by analytical methods to verify the validity of the model test results on a quantitative basis. To this end, the stability of the centrifuged slope is analyzed by the upper-bound method in limit analysis. Solutions obtained by the finite-element method and the simplified Bishop's method of limiting equilibrium analysis are compared with the test results in terms of the critical height and/or the location of the failure surface of the slope.

BACKGROUND

In general, physical models can be grouped into two categories depending on whether they satisfy the principles of similitude or not (1). In order to predict the behavior of the prototype on a quantitative basis by using model test data, however, the principles of similitude should always be satisfied in the model system.

If the principles of similitude are satisfied in the model, one can pass from a certain quantity y' derived from the model to a homologous quantity y in the prototype by means of a scale factor that is fixed by similitude. In problems of statics there are two independent quantities, length and specific force (force per unit area); therefore, two independent scale factors for the respective quantities involved may be defined as follows:

$$\lambda = L/L' \qquad \xi = \sigma/\sigma' \tag{1}$$

where

λ, ξ = scale factors for length and specific force, respectively;
L, σ = length and specific force in prototype; and
L', σ' = length and specific force in model.

It may be noted that the length scale λ must also be valid for displacement and that the scale factor of specific force ξ must be valid for all quantities having the dimensions of specific force, for example, modulus of elasticity E and shear stress τ.

Since the scale factor of length λ is always greater than unity for practical geotechnical models, only two types of models, when they are classified with respect to the magnitude of the scale factors, are possible in the modeling of such problems. They are (a) models in which the scale factor of the specific force ξ is greater (or smaller) than 1 and (b) models in which the scale factor of the specific force ξ is equal to 1.

The first type of modeling requires that the failure envelopes of the model and prototype materials must be geometrically similar with respect to the origin of the axes in the Mohr diagram, as shown in Figure 1a (1), according to the following relations:

$$\sigma = \xi\sigma' \qquad \tau = \xi\tau' \tag{2}$$

At the same time, the stress-strain curves of the prototype and model materials must also correspond as shown in Figure 1b, according to the following relations:

$$\sigma = \xi\sigma' \qquad \varepsilon = \varepsilon' \tag{3}$$

In earth structures, however, it is extremely difficult, if not impossible, to satisfy these two critical conditions imposed on the model material.

In the second case, the material of the prototype can be used for the model provided that body forces can be ignored when compared with boundary forces. However, body forces are almost invariably significant in soil-mechanics prototype problems, and the investigator is then faced with the requirements of the similarity of body forces. The scale factor of body forces η may be expressed as follows:

$$\eta = \gamma/\gamma' = (\sigma \cdot L^{-1})/[\sigma' \cdot (L')^{-1}] = \xi \cdot \lambda^{-1} \tag{4}$$

where γ and γ' are the unit weights of prototype and model materials, respectively. Substituting $\xi = 1$ into Equation 4, we obtain the following:

$$\eta = \gamma/\gamma' = \lambda^{-1} \tag{5}$$

that is to say,

$$\gamma' = \gamma \cdot \lambda \tag{6}$$

Equation 6 implies that the unit weight of model material should be as many times greater than the length scale λ than the unit weight of prototype material. Furthermore, this model material should have the same mechanical properties with respect to both strength and stress-strain behavior as the prototype material, since the scale factor of specific force ξ is now equal to unity. Again, it is impossible to find such a model material that satis-

fies these requirements without introducing a special technique by which the unit weight of model material can be increased as many times as required.

By using a centrifugal modeling scheme, in which the material of the prototype is used for the model, one can satisfy these requirements. By the definition of the unit weight, $\gamma = \rho \cdot \underline{g}$, where ρ is mass per unit volume and $\underline{g}$ is acceleration of the gravity force. Substituting this into Equation 6, we get the following:

$$\gamma' = \rho \cdot g \cdot \lambda = \rho \cdot a \tag{7}$$

where $a = \lambda \cdot \underline{g}$. Therefore, if the magnitude of the acceleration of the gravity force $\underline{g}$ can be magnified as many times as the scale factor of length λ in the model system, the principles of similitude will be satisfied. The magnification of the acceleration field can be achieved easily in a centrifuge, where a centrifugal acceleration of the force of inertia is generated.

EQUIPMENT

The centrifuge used in this investigation is a modified version of the Genisco Model 1230-5G accelerator at the University of Colorado. The centrifuge system is shown in Figure 2. The effective radius of the centrifuge is 53.5 in measured to the base of the swinging basket, and the weight capacity is 20 000 $\underline{g}$-lb. The essential features of this centrifugal system are described below.

Of the two swinging baskets hinged to the ends of the rotating arm, one (3, Figure 2) was used to mount the test package consisting of a specimen container (4) and a mirror system (5). The other (6) was used as a counterweight mount to balance the centrifuge dynamically as well as statically. The maximum dimensions of the allowable test package on the basket are 18x18x12 in.

The closed-circuit television camera is mounted close to the centrifuge axis and is focused on the test package through the mirror system so that the behavior of a model structure in the specimen container during the experiment can be observed. The experiment can be recorded by a video tape recorder outside the centrifuge. In addition, two hydraulic rotary joints are available in this system for hydraulic power transmission into the centrifuge for driving jacks, for instance, but they were not used in these experiments.

TEST PROGRAMS AND PROCEDURES

Three series of plane strain slope models were constructed and tested in the centrifuge. The slopes in each series had a similar geometry with the same slope angle (60°) but with different heights (8, 4, or 2.67 in), as shown in Figure 3. Two kinds of granular soils, identified as A and B, were used in the construction of slopes. They were artificially batched in the laboratory according to the gradation curves, which were chosen arbitrarily. For both soils, 5 percent of moisture was introduced to create the apparent cohesion as a result of the negative pore-pressure development.

The specimen container has the inside dimensions 16x11.5x6 in. The front wall of the container was made of lucite plate 1 in thick so that a model slope inside the container could be seen through the wall, while the other three walls and the base were made of aluminum plate 0.5 in thick. The lucite wall has a 1-in^2 grid scribed on its inside surface, which is used as a datum for marking the shape of the failure surface after a slope failure. Wood formworks of three sizes were used to define the geometries of the model slopes.

The model slopes were constructed in the following manner:

1. The container was laid horizontally with the front lucite wall removed.
2. A wood formwork was clamped down in the proper position according to the specified geometry of the slope to be built.
3. Dry soil and 5 percent of water by weight were mixed, and the mixed soil was compacted in layers in the specimen container.
4. The lucite wall was attached to the container, which was then erected to its testing position.

After being located in the centrifuge, slope test models were accelerated by increasing the rotational velocity of the centrifuge until failure. Each individual test was monitored by the TV video system through the failure stage.

MODEL TEST RESULTS

If the scaling relations derived from the principles of similitude are to be observed in centrifugal model testing, all three series of the model slopes of similar geometry, built of the same soil at the same density, should predict identical prototype behavior in terms of the critical height of the slope, which can be obtained by the following expression:

$$H_c^p = H_m \times (a/g) \tag{8}$$

where H_c^p is the predicted critical height of the prototype slope, H_m is the height of the model slope at failure, when the centrifugal acceleration reached the value a, and $\underline{g}$ is the acceleration of the gravity force. However, the densities of the soils in the test models could not be controlled exactly for all the model slopes tested in this study; therefore, the critical heights calculated would not all be identical but are a function of soil densities, as the strength of soils is. With this in mind, the results of the three series of model tests listed in Tables 1 and 2 and plotted in Figures 4 and 5 can now be examined.

In Figures 4 and 5, best least-squares-fit lines are drawn through the data points of each series of models. It is noticed from the fitted lines that there is a trend showing that the H_c^p values increase as the density of the slope soil increases, as expected.

Comparisons are made among the results of the three series at the middle of the density range, 108.5 pcf and 101.0 pcf for soils A and B, respectively. At that density, the average value of the predicted critical height is calculated from the fitted lines, and deviations from this average for each of the three model scales are calculated. Thus, it is shown in Figures 4 and 5 that the 4-in model predicted a critical height of the prototype to be 8.3 percent higher and the 8-in model predicted a height 11.5 percent lower than the average value for soil A, while for soil B the predicted critical height by the 2.67-in model is higher by 6.2 percent and that by the 8-in model is lower by 10.2 percent than the average value of the H_c^p at the soil density of comparison. Such scatter is considered to be negligible in engineering applications, and it is concluded that all three series of the model slopes predict identical prototype behavior in terms of its

Figure 2. Centrifugal system used in experiments: 1, slip-ring assembly; 2, closed-circuit TV camera; 3, test package basket; 4, specimen container; 5, mirror system; 6, counterweight basket.

Figure 3. Configuration of model slope.

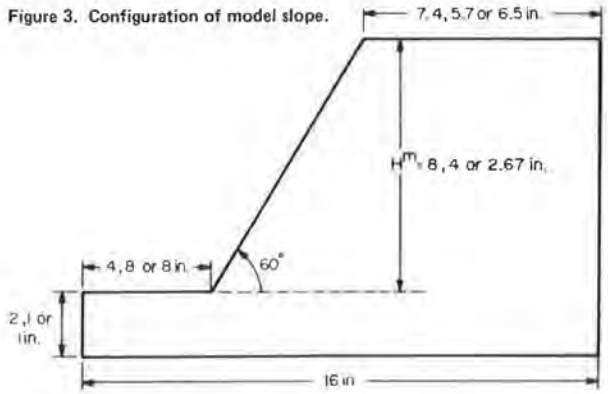

critical height. Thus, the concept of modeling of models is confirmed.

In Figure 6, the failure surface observed from the centrifugal slope model tests is shown in the form of a band bracketing the locations observed in all the tests. This will be compared later with the failure surfaces obtained by analytical methods.

SLOPE STABILITY ANALYSIS BY ANALYTICAL METHODS

To examine quantitatively the validity of the results of the centrifugal slope model tests, the stability problem of the centrifuged slope is solved by the analytical methods such as the upper-bound method in limit analysis, the finite-element method, and the simplified method in limiting-equilibrium analysis, and the results of these analyses are compared with the model test results.

Limit Analysis

In solving the stability problem by the upper-bound method in limit analysis, a rotational failure mechanism is assumed in this study, as shown in Figure 7, in which the failure surface passes through the toe of the slope. In Figure 7, the triangular region ABC rotates as a rigid body about the center of rotation 0; the materials below the logarithmic surface BC remain at rest.

To obtain an upper bound for the critical value of the height of the slope in Figure 7, the external rate of work done by the soil mass ABC is equated to the internal energy dissipation along the surface BC, which gives the following expression (2):

$$H = (c/\gamma)\, f(\theta_b, \theta_t) \tag{9}$$

where the function $f(\theta_b, \theta_t)$ is defined as follows:

$$f(\theta_b, \theta_t) = \left\{ \exp[2(\theta_b - \theta_t)\tan\phi]/2\tan\phi(f_1 - f_2 - f_3) \right\} \left\{ \sin\theta_b \exp[(\theta_b - \theta_t)\tan\phi] - \sin\theta_t \right\} \tag{10}$$

in which θ_b and θ_t are as defined in Figure

Table 1. Test results for soil A.

Specimen Number	Unit Weight (pcf)	a/g at Failure	Predicted H_c^p (in)	Water Content[a] (%)
8-in Model				
A-8-1	109.21	32.3	258.4	4.72
A-8-2	109.21	29.1	232.8	4.42
A-8-3	108.55	25.2	201.6	4.05
A-8-4	109.21	24.4	195.2	4.85
A-8-5	109.21	30.3	242.4	3.94
A-8-6	107.89	21.2	169.6	3.66
A-8-7	111.84	41.4	331.2	4.29
A-8-8	110.26	30.3	242.4	4.92
A-8-9	109.67	27.5	220.0	5.41
A-8-10	107.81	27.5	220.0	4.68
4-in Model				
A-4-1	107.62	54.5	218.0	4.69
A-4-2	107.62	67.5	270.0	4.58
A-4-3	105.96	43.3	173.2	4.43
A-4-4	109.27	65.7	262.8	5.07
A-4-5	107.28	52.2	208.8	5.47
2.67-in Model				
A-8/3-1	108.94	105.8	282.5	4.55
A-8/3-2	106.50	70.8	189.0	5.26
A-8/3-3	107.32	74.0	197.6	4.28
A-8/3-4	108.94	86.4	230.7	4.12
A-8/3-5	106.50	61.5	164.2	4.63

[a]Water content was measured immediately after testing.

Table 2. Test results for soil B.

Specimen Number	Unit Weight (pcf)	a/g at Failure	Predicted H_c^p (in)	Water Content[a] (%)
8-in Model				
B-8-1	101.32	18.0	144.0	4.73
B-8-2	101.32	17.3	138.4	4.74
B-8-3	101.84	17.6	140.8	4.80
B-8-4	100.66	16.4	131.2	4.43
B-8-5	101.32	20.9	167.2	4.57
B-8-6	101.32	23.4	187.2	4.46
4-in Model				
B-4-1	98.68	32.1	128.4	5.05
B-4-2	100.00	39.4	157.6	4.62
B-4-3	100.66	37.0	148.0	4.96
B-4-4	100.66	43.8	175.2	4.41
B-4-5	101.32	45.3	181.2	4.93
2.67-in Model				
B-8/3-1	101.63	64.5	172.2	4.60
B-8/3-2	100.81	57.9	154.6	5.19
B-8/3-3	99.19	52.8	141.0	4.72
B-8/3-4	100.00	70.8	189.0	4.51
B-8/3-5	100.81	72.7	194.1	4.48

[a]Water content was measured immediately after testing.

Figure 4. Results of centrifugal slope model tests, soil A.

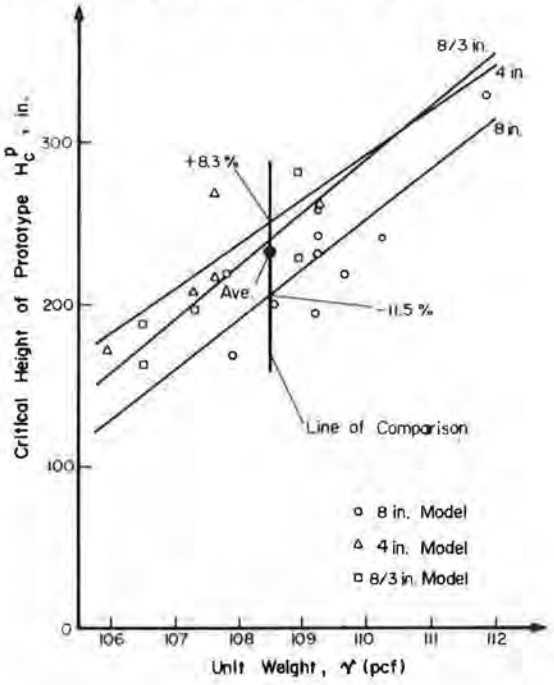

Figure 5. Results of centrifugal slope model tests, soil B.

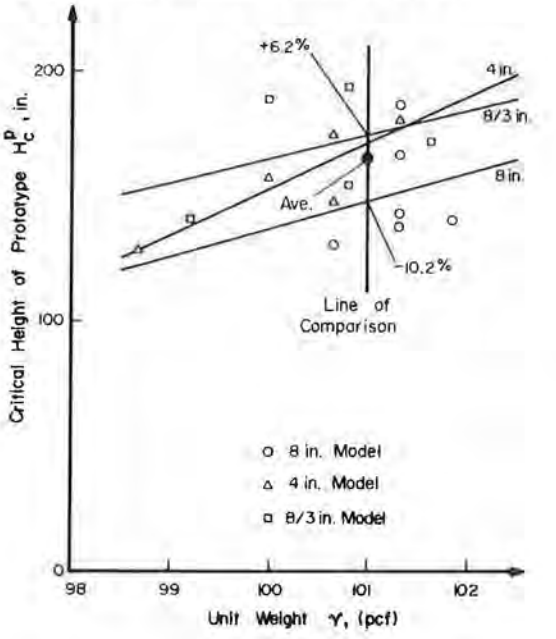

7, ϕ is the friction angle, and the following expressions hold:

$$f_1(\theta_b,\theta_t) = [1/3(1+9\tan^2\phi)]\,(3\tan\phi\cos\theta_b + \sin\theta_b)\exp[3(\theta_b - \theta_t)\tan\phi - (3\tan\phi\cos\theta_t + \sin\theta_t)] \quad (11)$$

$$f_2(\theta_b,\theta_t) = (1/6)(L/r_t)[2\cos\theta_t - (L/r_t)]\sin\theta_t \quad (12)$$

$$f_3(\theta_b,\theta_t) = (1/6)\exp[(\theta_b-\theta_t)\tan\phi]\,[\sin(\theta_b-\theta_t)(L/r_t)\sin\theta_b]\cos\theta_t - (L/r_t) + \cos\theta_b\,[\exp(\theta_b-\theta_t)\tan\phi] \quad (13)$$

L and r_t are also defined in Figure 7.

A least upper bound for the critical height of the slope may be obtained by finding a minimum value

Figure 6. Failure surface of centrifugal model slope.

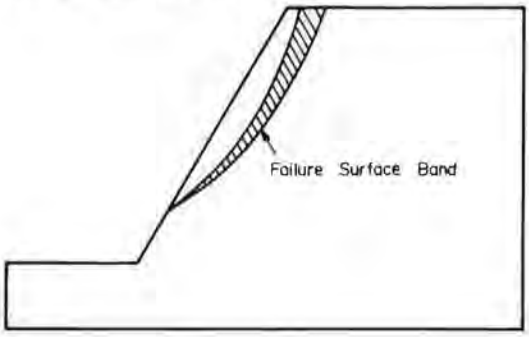

Figure 7. Failure mechanism for stability of embankment with failure plane passing through toe.

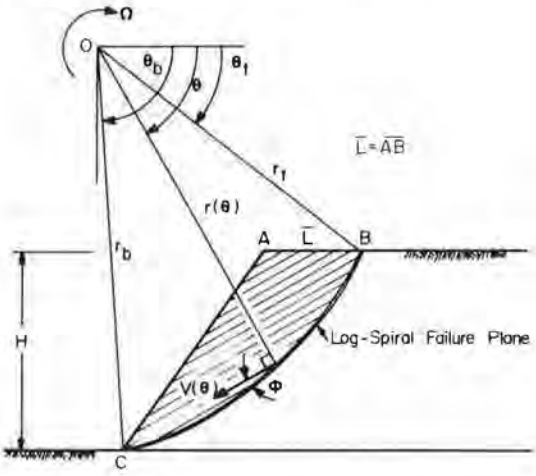

of the function $f(\theta_b,\theta_t)$, i.e.,

$$H_c = (c/\gamma)\min[f(\theta_b,\theta_t)] = (c/\gamma)N_s \quad (14)$$

where $N_s = \min[f(\theta_b,\theta_t)]$, and it is known as a stability factor of slope. The N_s-values for various geometries and friction angles may be found in the study by Chen (2).

With N_s known, a least-upper-bound critical height of a slope can be calculated by Equation 14. However, it is observed from the model test results, as shown in Figure 6, that the failure surface of the model slopes did not pass through the toe but passed through a point approximately 20 percent of the height of the slope above the toe. Therefore, to obtain the least-upper-bound critical height of the centrifuged slope, a factor of 1.25 was applied to the solution obtained by Equation 14 to take into account the fact that the failure surface passed approximately 20 percent of the actual height of the slope above the toe. In this manner, the least-upper-bound critical heights of the centrifuged slopes were calculated at three different densities for both soils and are given in Table 3. For these calculations, soil strengths obtained from triaxial testing reported by Kim (3) were used.

Finite-Element Analysis

The finite-element method (FEM) was used to find a lower-bound solution for the given slope problem. The lower-bound theorem of the limit analysis can be stated as follows: If a state of stress can be

Table 3. Results of limit analysis.

Density γ (pcf)	Cohesion c (psi)	N_S	H_c^* (in)	H_c[a]
Soil A				
106.0	0.56	20.26	185.0	231.3
108.0	0.66	23.02	243.1	303.9
110.0	0.76	25.88	309.0	386.3
Soil B				
99.5	0.51	18.48	163.7	204.6
100.5	0.54	19.35	179.7	224.6
101.5	0.57	20.19	195.9	244.9

[a]Equals $1.25 \times H_c^*$.

Figure 8. Mohr circle plot for calculation of factor of safety.

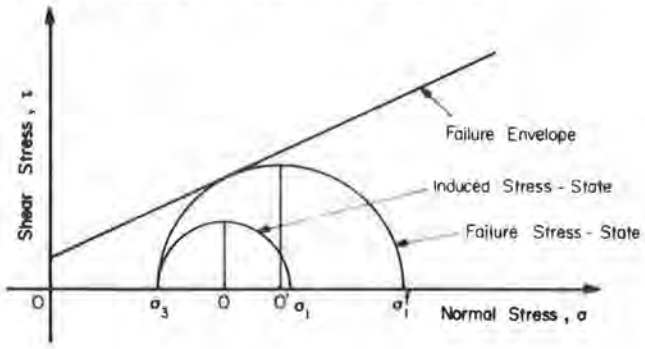

found that satisfies the stress equilibrium and boundary conditions and that does not exceed the yield condition, then no collapse occurs. By the FEM, a state of stress can be found that satisfies the stress equilibrium and boundary conditions. Therefore, if the maximum loading condition is found that induces a state of stress without violating the yield condition anywhere in the structure, it will provide the highest lower-bound solution.

An eight-node isoparametric quadrilateral finite-element program SLOPE was developed for the slope stability analysis during the course of this investigation. In the program SLOPE, nonlinear stress-dependent stress-strain behavior of soil was approximated by a hyperbolic function (4,5), and the incremental tangential Young's modulus E was evaluated by differentiating the function (6). Poisson's ratio was assumed to be 0.35, which is a typical value for partly saturated soils.

In this analysis, failure of an element is assumed to occur when the magnitude of the shear stress developed in an element reaches that of the shear strength. A factor of safety is defined as the ratio of the maximum shear stress induced to the maximum shear stress allowable, which can be visualized on a two-dimensional Mohr circle plot as shown in Figure 8. In Figure 8, the ratio of the radius of the small circle representing the actual stress state induced to the radius of the larger circle representing the stress state at failure represents the factor of safety.

A failure surface is obtained from the factors of safety calculated for assigned elements by finding a continuous line connecting the combination of elements having the smallest overall factor of safety. The continuous line forming a failure surface is assumed to be a circular arc that passes through the top crest of the slope. The overall factor of safety for the entire failure surface F_s can be calculated by the following expression (7):

$$F_s = \sum_{i=1}^{n} (\ell_i/L) f_{si} \qquad (15)$$

Figure 9. Trial failure surfaces of finite-element analysis.

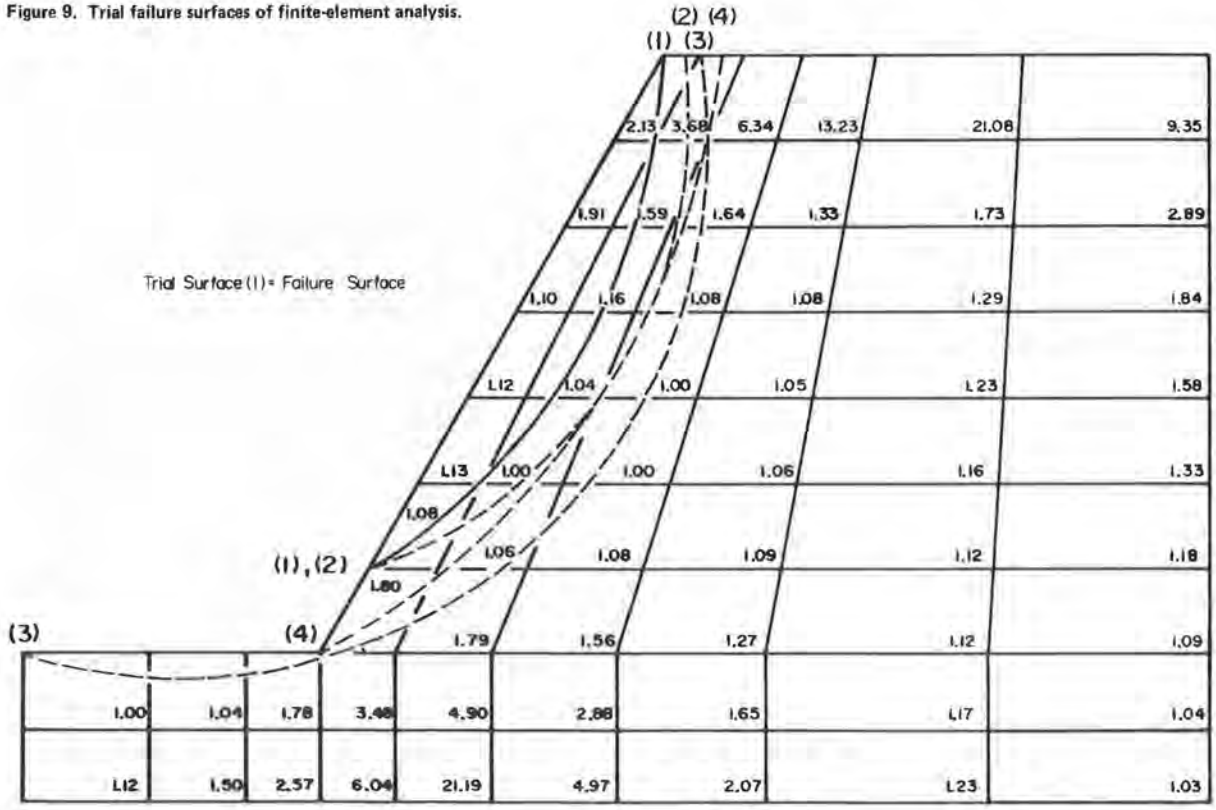

Figure 10. Failure surfaces obtained by SNOB for soils A and B at various densities.

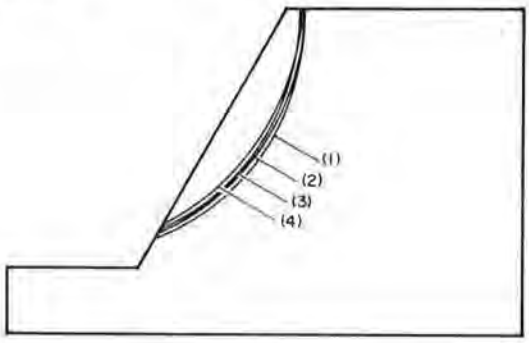

Figure 11. Comparison of results in terms of H_c^p for soil A.

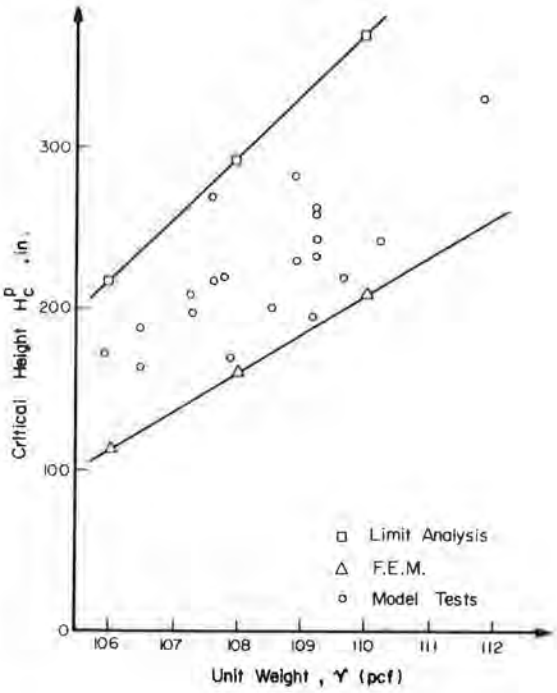

where

f_{si} = factor of safety of element i along failure surface,
ℓ_i = length of failure surface through element i,
L = total length of failure surface, and
n = number of elements on failure surface.

Four trial failure surfaces of circular arcs, which were selected so as to pass through the elements having smaller f_{si}'s than those of the surrounding elements, are shown in Figure 9. Also shown in Figure 9 is the f_{si} of each element at the critical point when any of the elements in the slope first reached an f_{si} equal to or less than unity on increased gravity loading. The overall F_s's of surfaces 1, 2, 3, and 4, calculated by Equation 15, were 1.29, 1.41, 1.50, and 1.57, respectively. Thus, surface 1, which has the smallest failure surface, is chosen to be the failure surface.

Since the procedure of incremental loading by body forces is employed in this method, the critical height of the slope is not directly determined, but the increased unit weight of the soil at the critical point is known, from which the equivalent critical height may be calculated by the following equation:

Figure 12. Comparison of results in terms of H_c^p for soil B.

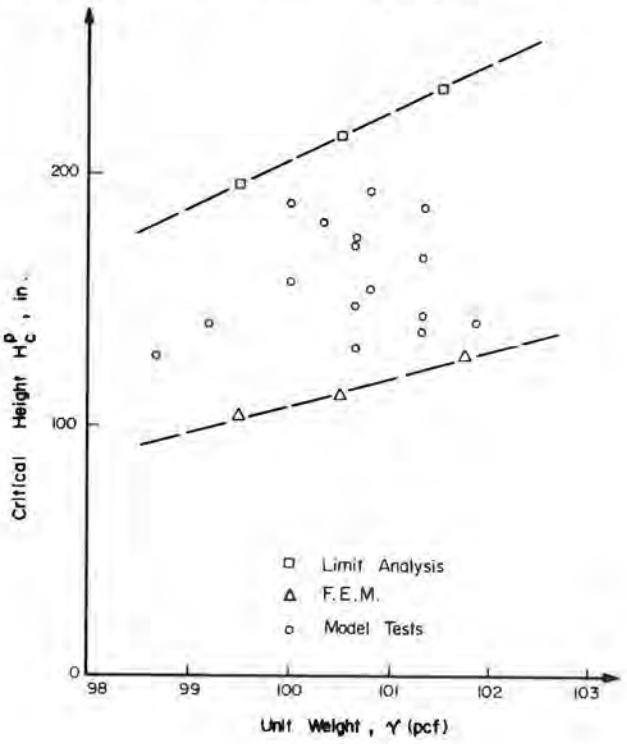

Figure 13. Comparison of failure surfaces.

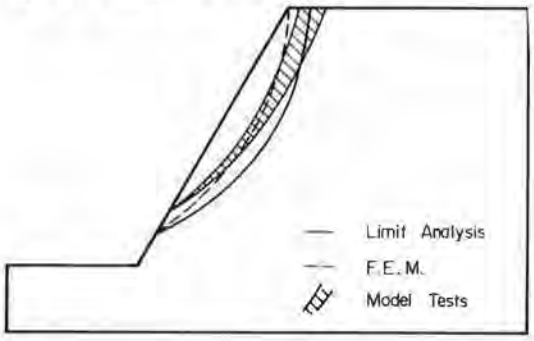

$$H_c = H_m(\gamma_f/\gamma) \quad (16)$$

where

H_m = height of a numerical model,
γ = initial unit weight of soil in model, and
γ_f = unit weight of soil at critical point.

The critical heights predicted by the FEM at three different densities of the two soils are given below:

Soil	Density γ (pcf)	Critical Height Hc (in)
A	106.0	120
	108.0	168
	110.0	216
B	99.5	104
	100.5	112
	101.5	128

Limiting-Equilibrium Analysis

The limiting-equilibrium slope stability program SNOB (stability--New York and Bishop) (8,9), which uses the simplified Bishop method of the analysis, was used to analyze the slopes for which the heights had previously been determined by limit analysis. Failure surfaces giving the minimum F_s's were obtained by an automatic searching method provided by SNOB and are shown in Figure 10. Soil types and densities for each failure surface are as follows: 1, soil B at 99.5 and 100.5 pcf; 2, soil A at 108.0 pcf; 3, soil A at 106.0 pcf and soil B at 101.5 pcf; and 4, soil A at 110.0 pcf. It is observed that the location of the failure surface is not very sensitive to the small changes of the densities of soil. Therefore, failure surface 2 will represent the failure surfaces when they are compared with those obtained by the FEM and the centrifugal model tests. The average minimum F_s of the slopes predicted by the limit analysis was 0.99. Since the slopes analyzed by the limiting-equilibrium method had the same height as that calculated by the upper-bound method of limit analysis, this implies that the simplified Bishop method used also produces upper-bound solutions. This is not generally the case, since in most limiting-equilibrium analyses, equilibrium (either force or moment) is not satisfied.

MODEL TEST RESULTS VERSUS ANALYTICAL SOLUTIONS

The critical heights of prototype slopes predicted by the upper-bound method of limit analysis and the lower-bound method of finite-element analysis are plotted against the densities of slope soils in Figures 11 and 12 for soils A and B, respectively; the centrifugal model test data are also shown. It is observed from Figures 11 and 12 that all the data points of the centrifugal model tests, in spite of the relatively large scatters, lie between the upper and lower bounds obtained by limit analysis and finite-element analysis, respectively. It is thus concluded from the observation that in slope stability the centrifugal model testing scheme gives consistent results with those of analytical methods such as limit analysis and finite-element analysis in terms of the critical height of a slope.

The failure surfaces obtained by the FEM and computer program SNOB are shown in Figure 13 superimposed on the failure surfaces observed in the centrifugal model tests, which are shown as contained in the band indicated. In general, the failure surface of a slope belongs to one of three different modes depending on whether it passes through the toe, below the toe, or above the toe of the slope. It is observed in Figure 13 that all the failure surfaces shown belong to the same mode passing above the toe, are shallow in depth, and are located sufficiently close to each other to allow us to conclude that the centrifugal model testing scheme also gives consistent results with those of the FEM and the simplified Bishop method in terms of the location of the failure surface.

DISCUSSION AND CONCLUSIONS

In both the centrifugal model tests and the finite-element analysis, the loading was applied as increasing gravity forces on the structure. Although such loading is certainly not the same as that in the case of an actual slope constructed incrementally, it has been shown by finite-element analysis (10) that the two methods of load application do not make much difference in the predicted critical slope height. By the same token, it can thus be argued that centrifugal tests of constructed models would produce similar results as tests in which the model is built up while the centrifuge is in flight. The latter is, of course, a much more difficult experiment to perform.

From the results of the investigation reported in this paper, it can be concluded that centrifugal modeling of slope stability problems gives self-consistent results. Quantitatively, the model test data also agree well with the results from well-established methods of analysis.

Although centrifugal modeling as a tool is becoming familiar to the geotechnical engineer, it should be pointed out that there are several ways in which it could be used. A centrifuge can be used to model a prototype design by constructing a model of it to include all the necessary details. A large centrifuge, of several hundred g-ton capacity, would be required. In the absence of such large facilities, small centrifuges of the size used in this investigation can still be used to test models to gather data for the validation of analytical methods. The analyses can be performed to simulate the test conditions in the centrifuge experiments in which the material properties and loading and boundary conditions are known exactly. In this manner, the feedback from the comparison between test data and analytical results can lead to an improvement in the design methods. Finally, centrifuge experiments can also be conducted for the purpose of observing the phenomena that could take place in the test structure under proper simulation of the gravity stress gradient. When such phenomena are properly understood, numerical models can be formulated to incorporate such effects into analysis and design. The operation of small centrifuges is inexpensive and many experiments can be run for parametric studies. It is foreseen that in the near future such facilities will be available to many geotechnical engineers for the purposes just described.

REFERENCES

1. E. Fumagalli. Statical and Geomechanical Models. Springer-Verlag, Vienna, 1973.
2. W.F. Chen. Limit Analysis and Soil Plasticity. Elsevier Scientific Publishing Co., New York, 1975.
3. M.M. Kim. Centrifuge Model Testing of Soil Slopes. Department of Civil Engineering, Univ. of Colorado, Boulder, Ph.D. thesis, 1980.
4. R.L. Kondner. Hyperbolic Stress-Strain Response: Cohesive Soils. Journal of Division of Soil Mechanics and Foundation Engineering of ASCE, Vol. 89, No. SM 1, Proc. Paper 3429, 1963, pp. 115-143.
5. R.L. Kondner and J.S. Zelasko. A Hyperbolic Stress-Strain Formulation for Sands. Proc., Second Pan American Conference on Soil Mechanics and Foundation Engineering, Brazil, Vol. 1, 1963, pp. 289-324.
6. J.M. Duncan and C.Y. Chang. Non-Linear Analysis of Stress and Strains in Soils. Journal of Division of Soil Mechanics and Foundation Engineering of ASCE, Vol. 96, No. SM 5, 1970, pp. 1629-1653.
7. E.L. Corp, R.L. Schuster, and M.M. McDonald. Elastic-Plastic Stability Analysis of Mine-Waste Embankments. U.S. Bureau of Mines, RI 8069, 1975.
8. S.J. Hasselquist and R.L. Schiffman. A Computer Program for Slope Stability: New York State and Simplified Bishop Method. Computing Center, Univ. of Colorado, Boulder, Rept. 74-5, 1974.
9. R.M. Leary. Computerized Analysis of the Stability of Earth Slopes. Bureau of Soil Mechanics, New York State Department of Transpor-

tation, Albany, Soil Design Procedure SDP-1, 1970.
10. I.M. Smith and R. Hobbs. Finite Element Analysis of Centrifuged and Built-Up Slopes. Geotechnique, Vol. 24, No. 4, 1974, pp. 531-559.

Publication of this paper sponsored by Committee on Mechanics of Earth Masses and Layered Systems.

Rectangular Open-Pit Excavations Modeled in Geotechnical Centrifuge

O. KUSAKABE AND A.N. SCHOFIELD

Tests of models made of soil in geotechnical centrifuges have become accepted as a method of study of mechanisms of ground deformation with less expense or delay and with more control of ground conditions than tests of prototype scale. Centrifuge test results are reported for four different rectangular open pits excavated rapidly in saturated clay soil of uniform strength with depth. It is found that the mechanism by which such excavation will cause road pavements and buried services to fail will fit the axisymmetric mechanism, where the upper part of the pit wall tends only to move vertically and the wall movement is dominated by plastic deformation of the lower part of the pit wall. Support in the upper region will have little effect on this axisymmetric mechanism, and the stability of the pit will be controlled by the strength of the ground near the base of the excavation. The observed mechanism induces tension in the upper portion of the ground and induces compression failure at depth. Flexible road construction is rather weak in tension, so the observed mechanism is probably relevant to pits passing through a flexible road construction and entering a lower layer of soft ground.

The excavation of trenches or of pits in roads can cause damage to road pavements or to buried services beside the excavation. Ground movements at failure can be fitted to failure mechanisms of the theory of plasticity. Studies of ground movements before failure show that the incipient failure mechanism is established well before failure occurs and that damaging ground movements increase rapidly as the factor of safety against failure is reduced. Tests of models made of soil in geotechnical centrifuges have become accepted as a method of study of mechanisms of ground deformation with less expense or delay and with more control of ground conditions than tests of prototype scale. This paper is concerned with the modeling of rectangular open pits excavated rapidly in saturated clay soil of uniform strength with depth.

The failure of a long trench is illustrated in Figure 1a, with a vertical face ABC moving down into the trench as soil slips on an inclined plane CD and a tension crack DE opens. The failure of a circular shaft is illustrated in Figure 1b and 1c. In the rapid undrained failure (Figure 1b), the lower portion BC of the vertical face squeezes in and an annular ring of soil of section BCD is plastically compressed and deformed. Above the plastic zone BCD a rigid block ABDE descends vertically; there is shearing on DE as well as on CD, on DB, and within BCD (1). In the long term, shown in Figure 1c, a shaft that is safe against rapid failure may exhibit a crack at B and subsequently begin to cave in. This paper reports tests of four different model rectangular open-trench or pit excavations; their behavior can be compared with these plane and axisymmetric cases.

The tests used Speswhite kaolin clay soil reconstituted from a slurry. It was consolidated with vertical effective stress σ_v' = 140 kN/m² and allowed to swell back into equilibrium in centrifuge flight with stresses $0 \leq \sigma_v' < 140$ kN/m² as shown in Figure 2. When rapidly sheared, such soil has shear strength $24 < c_u < 32$ kN/m² throughout the model depth. In such rapid shearing the effective mean normal stress in the clay approaches a critical state pressure (in this case, say, p' = 62 kN/m²) and the pore-water pressures take whatever value is needed to balance externally applied total pressure. In the longer term, excess pore-water pressure gradients will lead to the flow of pore water. A point of particular interest in these tests is the observation of pore-water pressure changes in the clay during and after the process of excavation.

CENTRIFUGE MODEL TEST SYSTEM

In centrifuge model tests, the weight of soil is increased and the scale of the model is reduced, both by a factor n (2). The result is identical similarity at corresponding points in a model and in a notional full-scale prototype of the total and effective stresses and strains in the soil and of the pore-water pressures. In addition, the reduction of model scale by a factor of n means that pore-water diffusion to achieve a given time factor ($T_v = C_v t/h^2$ in Terzaghi's consolidation theory) requires times t_m in the model greatly reduced in comparison with times t_p in the prototype in the ratio $t_m/t_p = 1/n^2$. In this paper, tests will be reported with axes on graphs both at the model and at the notional prototype scale. Details of the model excavation dimensions are shown in Figure 3; positions of pore-water pressure transducers (PA, PB, and PC) and of displacement transducers [linear variable differential transformers (LVDTs), LR, LS, and LT] are shown in the plan for each model at model scale.

The models were made in a circular tub of internal diameter 850 mm (designated 1 in Figure 4). The clay (2) was consolidated and the pit (3) excavated and lined with a rubber bag (4) containing a bag pressure transducer (5). The bag was filled with a heavy fluid $ZnCl_2$ solution (3). Pore-water transducers A, B, and C had been consolidated into position 7. Lead powder threads were injected into the clay (8), and lead shot was placed on various surfaces. These would allow study of deformation during dissection of the model. In flight there were LVDT measurements that followed surface movements.

In flight the upper surface of the clay was partly covered by water maintained at a constant level D as sensed by a transducer (10). A cross beam (11) carried transducers and a junction box (12). After the models were made, the system was brought into equilibrium with about 9 h of centrifuge flight. The process of excavation was modeled by draining the $ZnCl_2$ solution down a vertical pipe (13). A solenoid valve (14) controlled the dumping of the $ZnCl_2$ solution into a reservoir (15). A second solenoid valve (16) isolated the surface level in a first reservoir (17), maintained from the slip-ring supply pipe (18), from the excavation base where there were filter papers (19) below the rubber bag. The excavation base drain pipe (20) was connected to a second reservoir (21), originally maintained at the same level (D) as the first reservoir. But on dumping, the level in the second reservoir fell to E, the excavation base level. It was significant to know the rate at which water seeped from the ground into the excavation and into the second reservoir, so a third reservoir (22) with a pressure transducer in it and a control valve (23) was placed between the second reservoir (21) and the waste pipe (24).

Features of the test system can be seen in Figure 5.

RECORD OF TEST 2

After a 9-h consolidation run in the centrifuge to monitor pore-water pressure and settlements and see when equilibrium was achieved, the excavation process was carried out. The excavation process was simulated by dumping the $ZnCl_2$ solution from the rubber bag in flight. The time required for excavation varies according to the size of the pits excavated. In these tests under a centrifuge acceleration of 75 g, from 15 to 30 s was needed, which corresponds to between one and two days at the notional prototype scale.

A magnetic tape recorder capable of recording a maximum of 14 channels simultaneously was used to record data from the pore-water pressure and settlement gauges. Figure 6 shows the data from pit test 2 plotted against time. As may be seen in Figure 6a, the bag pressure (measuring the $ZnCl_2$ solution pressure at the base of the pit) fell to approximately 10 kN/m² within 18 s and then gradually increased with time. After the centrifuge had been stopped, it was observed that the lower part of the pit wall was closed up and the bag pressure transducer was trapped, which probably explains the subsequent rise in the bag pressure.

The first change in settlement to occur (up to about 10 s) during the reduction of the bag pressure is very slight, as shown in Figure 6b. Further reduction of the bag pressure produced a rapid increase in the settlement rate. During undrained shear deformation of soil, the ground surface settlement has to be compensated by the inward movement of the pit wall, which is likely to alter the rate at which the bag pressure falls. It can be seen in Figure 6a that the rate at which the bag pressure falls has changed after about 10 s. After completion of the excavation, the rate of settlement

Figure 1. Failure mechanisms.

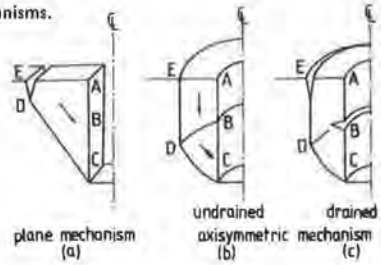

Figure 2. Stress history and strength profile.

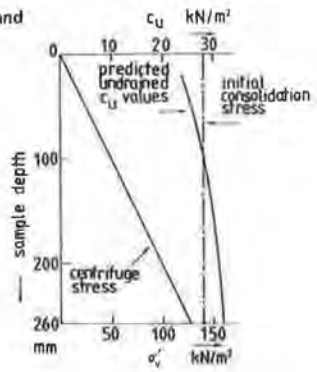

Figure 3. Pit dimensions and positions of LVDTs and pore-water pressure transducers.

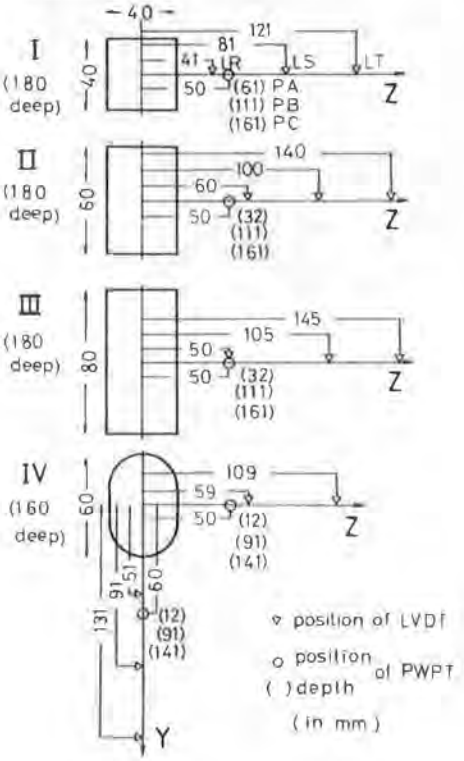

Figure 4. Test system.

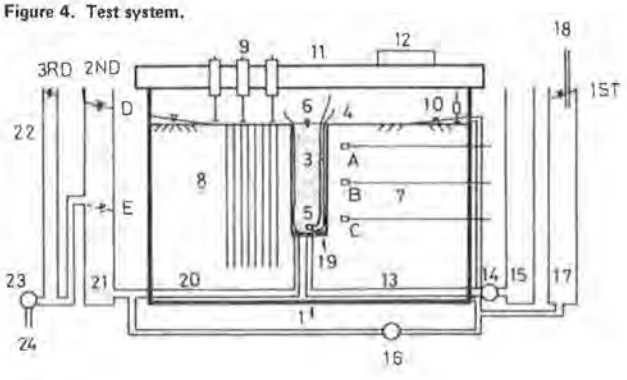

quickly levels off. Once the base of the pit has closed up, there will be little further settlement. In this case about 4.0-4.5 mm of surface settlement near the pit seems enough to make the base of the pit close. Since the pit width is 40 mm, the horizontal displacement of each pit wall needs to be 20 mm. Therefore, it appears that the rate of horizontal movement at the pit-wall base is about four to five times faster than that of the surface movement near the pit.

Figure 5. Centrifuge model system.

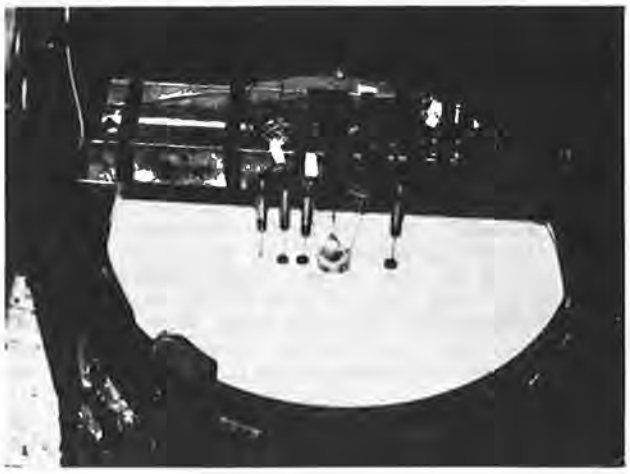

Figure 6. Data from pit test 2 versus time.

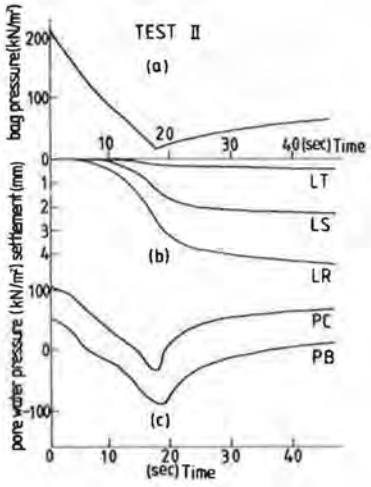

Figure 7. Settlement and pore-water pressure changes with excavation depth.

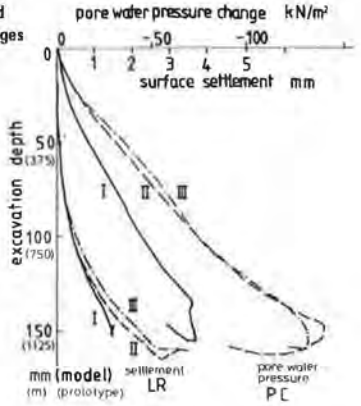

Figure 6c presents pore-water pressure changes during the test: They fall as the bag pressure drops. At about 14 s, a rapid change in the rate of fall of the pore-water pressure appears. This corresponds to the start of the steepest part of the settlement rate. Pore-water pressure suction is developed in soil during the development of a rupture plane.

Figure 8. Pore-water pressure change with excavation depth.

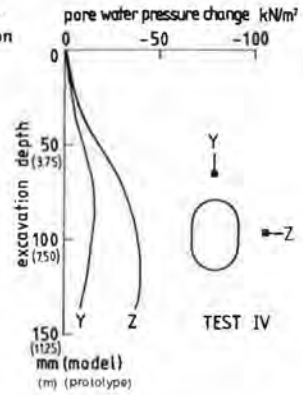

Figure 9. Settlement profiles after excavation.

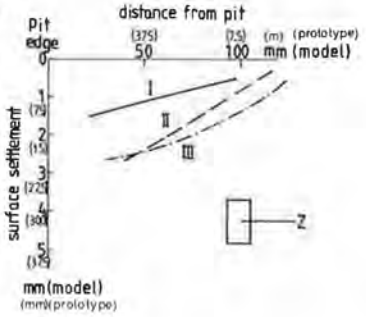

Figure 10. Settlement profile change with time.

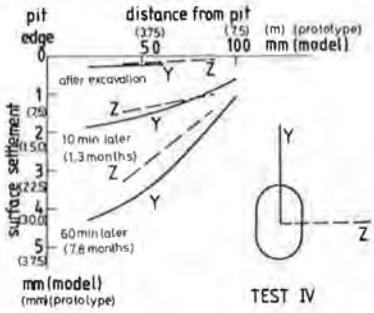

Figure 11. Wall movements.

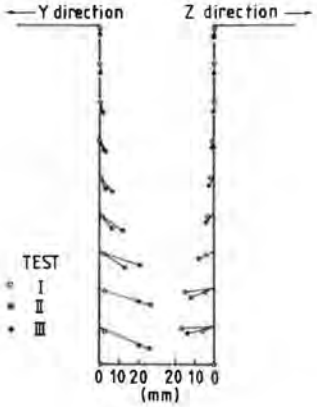

PORE-WATER PRESSURE CHANGES AND SETTLEMENT RATES

Figure 7 shows how the pore-water pressures and settlements change with the excavation depth for pit tests 1, 2, and 3. The settlements remain small values until the excavation depth reaches about 100 mm. During this period, a linear relationship between the excavation depth and the fall in pore-water pressure can be noticed.

It is important for those engaged in practical excavation work to appreciate that saturated clay soil is a granular material and that whenever it stands with an exposed vertical face there is a suction in the pore water. The safety of the excavation depends on the ability of soil to "hold its breath" for a time, and it is often only a matter of a short time before pore-water suction decays, as is clear from the record in Figure 6c. Also, in the undrained deformation the magnitude of the suction that is generated will be greatest where the greatest shear stress is mobilized.

In the test of pit 4, the pore-water pressure changes in the two directions (perpendicular to the long side and to the short side of the pit but at the same depth) were measured as is shown in Figure 8. The pore-water pressure change in the Z direction is larger than that in the Y direction. This is consistent with the trends illustrated in Figure 7, that is to say, the large face of excavation results in the large total stress change and causes the large pore-water pressure change in the vicinity of the excavation; the longer side is subjected to the larger deviator stress.

EXTENT OF DAMAGE

Soil engineers are always concerned about a subsidence of the surrounding area induced by excavation work. According to Peck (4), in the problem of plane-trench excavation in soft clay ground, the settlement may extend as far as four times the excavation depth. The settlement damage zone for an axisymmetric excavation is smaller than that for the plane-trench excavation. In the case of our rectangular open pits, Figure 9 shows the settlement profiles (on a line perpendicular to the longer face) at the moment of completion of the excavation for pits 1, 2, and 3. It is apparent that as the side length of the pit increases, the settlement profile has a flatter shape and the depression zone extends farther, although it does not extend beyond one excavation depth so far as this series of tests is concerned.

Pit 4 was left standing (with steady slow seepage into the excavation) for 1 h, corresponding to 7.8 months in the notional prototype scale. Figure 10 presents the change of settlement profiles during this period. Here the surface settlement results not only from the inward displacement of the pit wall but also from the compression of the soil due to the lowering of the ground-water level. At the moment the excavation is completed, the settlements in both directions are very small, less than 0.3 mm, indicating no signs that large deformations have taken place during the excavation. Subsequently the settlement gradually increases and reaches more than 4 mm (0.3 m in the prototype scale) at the point near the pit edge after 60 min (7.8 months in the prototype scale). The settlement becomes more localized toward the pit edge and its shape becomes a reverse dome shaped with time. This may be because the region nearer the pit is being affected more by the lowering of the ground-water level. The depression zone, however, was about the same as those observed under undrained conditions.

Our interpretation of centrifuge model tests (5) is based on a supposition that the effectively stressed soil behaves as an elastoplastic and not as a viscous material: All time effects are supposed to arise from transient pore-water pressure gradients. It is also supposed that the geometry of the failure mechanism is independent of the scale of the test. If a full test series were to be undertaken and reported (at much greater length than is available in this paper), that would normally include similar tests at different scales. This modeling of models would allow us to check the correctness of the supposition that diffusion time in models will scale with the square of the dimension scale.

OBSERVED FAILURE MECHANISM

For undrained deformations, the surface settlement is a direct indication of the wall movement during the excavation process. Figure 11 presents the vectors of wall movement obtained from observation of the movements of the lead shot shown on the X-ray radiograph. It is clear that the wall movement is dominated by plastic deformation of the lower part of the pit wall. For pit 2, for instance, the maximum horizontal movements in the Y and the Z directions are 27 mm and 16 mm, respectively. Another important feature here is that the direction of the movement vectors changes with depth from vertical to horizontal. This corresponds more to the axisymmetric problem in Figure 1b and 1c than to the plane problem in Figure 1a. This is clearly confirmed in Figure 12, which shows the radiograph of pit 3 in the Z direction, where the lead powder threads show clear discontinuities forming a triangular shearing zone.

It is common practice to provide temporary support for the excavation work to prevent collapse of the pit wall. However, it is often the case that the lower part of the wall is left unsupported. The use of support for only the upper part of the wall prevents mobilization of the plane failure mechanism (Figure 1a) but not of the axisymmetric failure mechanism (Figure 1b or 1c). As may be seen in Figure 1, in the case of axisymmetric mechanisms the upper part of the wall will tend only to move vertically. Support in the upper region would have had little effect on a failure such as that illustrated in Figure 11.

Although in our model tests the upper portion of the ground was clay and in a typical road construction the upper portion is made much stronger in compression, the observed mechanism induces tension in the upper portion and induces compression failure at depth. A series of calculations has been made to study the significance of cracking of flexible pavement layers. Before cracking of the layer, its strength not only increases the factor of safety but also tends to increase the radius of the critical failure mode AE in Figure 1b compared with the case of a single soft layer. When the layer cracks, it acts as a surface load and reduces the factor of safety significantly and also reduces the dimension AE to the same size as that of the single layer. Flexible road pavement construction is rather weak in tension, so the observed mechanism probably is quite relevant to pits passing through a flexible road construction and entering a lower layer of soft ground.

In addition to the loss of strength associated with vertical cracks in a pavement layer, it also appears to be possible in drained long-term conditions for horizontal cracks into the vertical pit face to lead to failure. Figure 13 was taken after pit 4 was dissected to see the internal deformation. Here a horizontal crack located just above

Figure 12. Radiograph of pit 3 Z-direction section.

Figure 13. Inside view of pit 4 dissected.

the triangular shearing zone has developed. Further tests are required to determine at what stage of the centrifuge run this horizontal crack occurred. However, when full-scale pits are excavated in ground with a high ground-water level, it is sometimes observed that in the longer term the lower part of the pit face is wet and that the seepage flow sloughs off the soil from the pit wall. This is the start of caving, and the debris falls to the full-scale pit base just as was observed after the test of model pit 4. The phenomenon of caving may be one of the critical design questions for the long-term stability of vertically sided pit excavations and is to be the subject of further tests in the current series.

CONCLUSION

Well-instrumented geotechnical centrifuge model tests stand as physical events in their own right with no less significance to the geotechnical engineer than full-scale trials of prototypes. This brief series of rectangular-pit excavation models forms a small part of a large program. However, even from this brief series of tests it is possible to deduce that the damage such excavations will cause to road pavements and buried services will fit the axisymmetric rather than the plane mechanism and will be controlled by the strength of the ground near the base of the excavation rather than the strength of the overlying pavement.

ACKNOWLEDGMENT

The four tests reported in this paper were undertaken at the expense of Cambridge University for the specific purpose of presentation at the 61st Annual Meeting of the Transportation Research Board in Washington, D.C., in January 1982. The extensive series of other model tests of which they form a part has been supported by the U.K. Transport and Road Research Laboratory and by the British Gas Corporation Engineering Research Laboratory. These other model tests will be reported and full details of stability calculations will be given in a forthcoming Ph. D. thesis to be submitted by Kusakabe in 1982.

REFERENCES

1. A.M. Britto and O. Kusakabe. Stability of Unsupported Axisymmetric Excavation in Soft Clay. Engineering Department, Cambridge Univ., England, Tech. Rept. CUED/D/-Soils/TR105, 1981.
2. A.N. Schofield. Cambridge Geotechnical Centrifuge Operation. Geotechnique, Vol. 30, No. 3, 1980, pp. 227-268.
3. P.V. Lade, H.L. Jessberger, E. Makowski, and P. Jordan. Modeling of Deep Shafts in Centrifuge Tests. Proc., 10th International Conference on Soil Mechanics and Foundation Engineering, Vol. 1, 1981, pp. 683-692.
4. R.B. Peck. Deep Excavation and Tunneling in Soft Ground. Proc., Seventh International Conference on Soil Mechanics and Foundation Engineering, Vol. 3, 1969, pp. 225-290.
5. A. Lyndon and A.N. Schofield. Centrifuge Model Test of a Short Term Failure in London Clay. Geotechnique, Vol. 20, No. 4, 1970, pp. 440-442.

Publication of this paper sponsored by Committee on Mechanics of Earth Masses and Layered Systems.

Preliminary Investigation of Bearing Capacity of Layered Soils by Centrifugal Modeling

A. C. HERDY AND F. C. TOWNSEND

The bearing capacity of circular footings founded on a sand layer overlying a clay layer was investigated by using centrifugal model tests. Model footings corresponding to prototypes ranging from 0.6 to 1.5 m were loaded to failure. Comparisons between observed model behavior and Meyerhoff's bearing-capacity theory for layered soils were made. These comparisons showed excellent agreement (less than 13 percent), which when considering the sensitivity of bearing-capacity coefficients to ϕ, is well within engineering acceptance.

Traditional bearing-capacity analysis of footings is limited to homogeneous soils extending to a depth B beneath a footing. To overcome this limitation, several theories and analyses have been presented. Button (1) presented a theory for nonhomogeneous (layered) soils; however, his analysis was applicable to clays only ($\phi = 0°$). Reddy and Srinivasan (2) extended Button's work to include anisotropic strength properties. Desai and Reese (3) applied the use of finite-element techniques to analyze the bearing capacity of footings founded on various clay layers with nonhomogeneous and nonlinear stress-strain properties. Brown and Meyerhof (4) performed laboratory model tests to investigate Button's theory. These previous investigations only considered clay layers, and only recently have layers involving friction and cohesion been analyzed. Meyerhof and Hanna (5) described analyses of footings subjected to inclined load on layered soils. Later in 1979, their work on two-layered soils was extended to include three layers (6). Purushothamaraj, Ramiah, and Rao (7) and Vesić (8) have also investigated the subject.

As can be seen, the bearing capacity of footings founded on layered soils has received considerable attention. However, verification of these theories is restricted by the inability to perform full-scale tests. In this context, centrifugal model testing offers a practical means for providing laboratory models that when subjected to a gravitational field will be in similitude with prototype structures.

PURPOSE AND SCOPE

The objective of this investigation was to verify Meyerhof's (9) theory for the bearing capacity of footings on a sand layer overlying a clay. This verification was accomplished by performing centrifugal model tests on a circular footing founded on a sand layer overlying clay.

DESCRIPTION OF THEORY

Based on model tests and some field observations, Meyerhof (9) proposed a semiempirical theory for two cases: layered soil composed of a dense sand layer overlying a soft clay and a loose sand overlying a stiff clay.

Case 1: Dense Sand on Soft Clay

Meyerhof observed that if a footing rests on a relatively thin dense sand layer above a soft clay deposit, failure may occur by breaking through the sand stratum into the clay. An approximate solution was developed by considering the failure to be an inverted uplift problem. This theory was found to hold true when the ultimate bearing capacity of a homogeneous thick bed on sand (q_t) is much greater than that of the underlying clay deposit (q_b).

According to Meyerhof (9), the ultimate bearing capacity for a rough strip footing of width B and depth D_f founded on a dense sand overlying a soft clay can be calculated by the following equation:

$$q_o = cN_c + 2P_p \sin\delta/B + \gamma D_f \quad (1)$$

where

$$P_p = 0.5\gamma H^2 (1 + 2D_f/H)K_p/\cos\delta \quad (2)$$

and K_p is the coefficient of passive earth pressure and H is the depth of the sand layer underlying the footing. Meyerhof suggested that the angle δ may be estimated as 0.67ϕ.

Meyerhof also suggested that a coefficient K_s, which represents the punching shearing resistance on the vertical plane through the footing edge, can be used. This coefficient is related to the corresponding earth pressure coefficient K_p by $K_s \tan\phi = K_p \tan\delta$

This relationship was found by Caquot and Kerisel (10) and is shown in Figure 1 (9) for various friction angles ϕ. It is of interest to note that K_s increases rapidly with ϕ from about one to two times the Rankine value of $\tan^2(45 + \phi/2)$.

By substituting all of the aforementioned values into Equation 1, it becomes the following:

$$q_o = cN_c + \gamma_s H^2 (1 + 2D_f/H)[(K_s \tan\phi)/B] + \gamma D_f \quad (3)$$

with a maximum value that corresponds to a single layer of sand of the following:

$$q_{o\,max} = q_t = (\gamma/2)BN_\gamma + \gamma D_f N_q \quad (4)$$

For circular footings of diameter B, depth D_f, and distance H above the clay surface, the bearing capacity can be approximated by the following:

$$q_o = 1.2cN_c + 2\gamma_s H^2 (1 + 2D_f/H)[(SK_s \tan\phi)/B] + \gamma D_f \quad (5)$$

with a maximum of the following:

$$q_{o\,max} = q_t = 0.3\gamma_s BN\gamma + \gamma D_f N_q \quad (6)$$

The above formula is an extension of the one for strip footings by considering the passive resistance P_p inclined at δ on a vertical cylindrical surface through the footing edge.

The S-factor that appears in the second term on the right-hand side of Equation 5 is a shape factor governing the passive earth pressure on a cylindrical wall. It may be conservatively taken as unity (1.0), especially for small ratios of H/B. Figure 1 also shows values of SK_s as a function of ϕ.

For rectangular footings of width B and length L, the first and second terms on the right-hand side of Equation 3 defined for strip footings should be multiplied by $(1 + 0.2B/L)$ and $(1 + B/L)$, respectively. This is an approximate interpolation between the values for bearing capacity obtained for circular and strip footings.

Figure 1. Coefficient of punching shearing resistance.

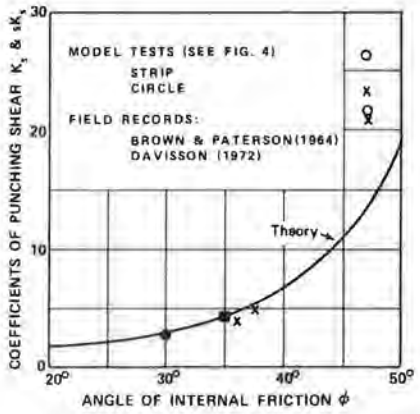

Figure 2. Theoretical modified bearing-capacity factors for strip footings.

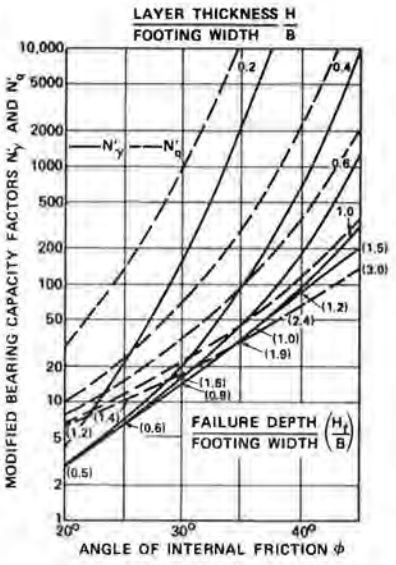

Case 2: Loose Sand on Stiff Clay

In this case the bearing-capacity failure may be limited to the sand layer. By considering that the ultimate bearing capacity of a thick bed of sand (q_t) is less than that of a thick bed of clay (q_b), the bearing capacity of the stratum may be estimated by assuming that the sand layer rests on a rigid base. The sand layer in this case may fail laterally by a squeezing action.

The bearing capacity of a rough strip footing founded on loose sand overlying a stiff clay layer may be expressed as follows:

$$q_o = \gamma B N'_\gamma/2 + \gamma D_f N'_q \quad (7)$$

with a maximum value that corresponds to a single layer of clay of the following:

$$q_o = q_b cN_c + \gamma D_f \quad (8)$$

The theoretical modified bearing-capacity factors N_γ' and N_q' that are dependent on ϕ, the ratio of H/B, and the degree of roughness of the rigid base are shown in Figure 2 (9). One should note that these factors increase with ϕ from the lower limits of N_γ amd N_q and as the ratio of H/B decreases from the depth ratio of H_f/B of the failure surface in a thick bed of sand.

For the case of circular footings, a solution was found by considering that in radial planes the stresses and shear zones are identical to those in transverse planes of a corresponding strip footing; i.e., the contact pressure distribution beneath the circle may be assumed to be similar to that for a strip. Therefore, the bearing capacity may be calculated from the following:

Figure 3. Theoretical modified shape factors for circular footings.

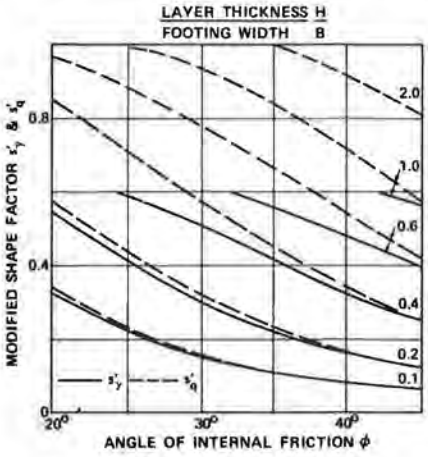

$$q_o = S'_\gamma \gamma B N'_\gamma/2 + S'_q \gamma D_f N'_q \quad (9)$$

with a maximum of the following:

$$q_o = q_b = 1.2cN_c + \gamma D_f \quad (10)$$

The modified shape factors S_γ' and S_q' are given in Figure 3 (9). These factors decrease from the conservative upper limits of $S_\gamma' = 0.6$ and $S_q' = 1$ for a thick bed of sand. Also, as ϕ increases and the ratio H/B decreases, both factors tend to similar values for small ratios of H/B.

For rectangular footings, the bearing capacity may be estimated by taking Equation 7 for strip footings and multiplying the first term on the right-hand side by $[1 - (1 - S_\gamma')B/L]$ and the second term by $[1 - (1 - S_q')B/L]$.

If the bearing capacity of the sand (q_t) approaches that of the clay (q_b), the failure surface beneath a footing extending into the clay and the shear zones becomes discontinuous at the interface, and the bearing capacity may be estimated by using an empirical parabolic intersection relationship of the following type:

$$q_o = q_t + (q_b - q_t)(1 - H/H_f)^2 \quad (11)$$

with a maximum for H/B = 0 when $q_o = q_t$.

EQUIPMENT

The University of Florida geotechnical centrifuge was manufactured by the Rucker Company and is a machine with a 1-m radius capable of accelerating a 25-kg payload to 85 g (Figure 4). It currently does not have a swinging bucket; the model is bolted to the end of the arm instead. For these tests, the soil was placed in a cylinder 25 cm in diameter. Loading of the model footings was accomplished by using a double-acting air piston to which regulated compressed air was supplied via two hydraulic slip rings. The load applied by the air piston was measured by using a miniature 226-kg (500-lb) load cell, while deformations were measured by using a

Figure 4. Principal layout of the University of Florida centrifuge.

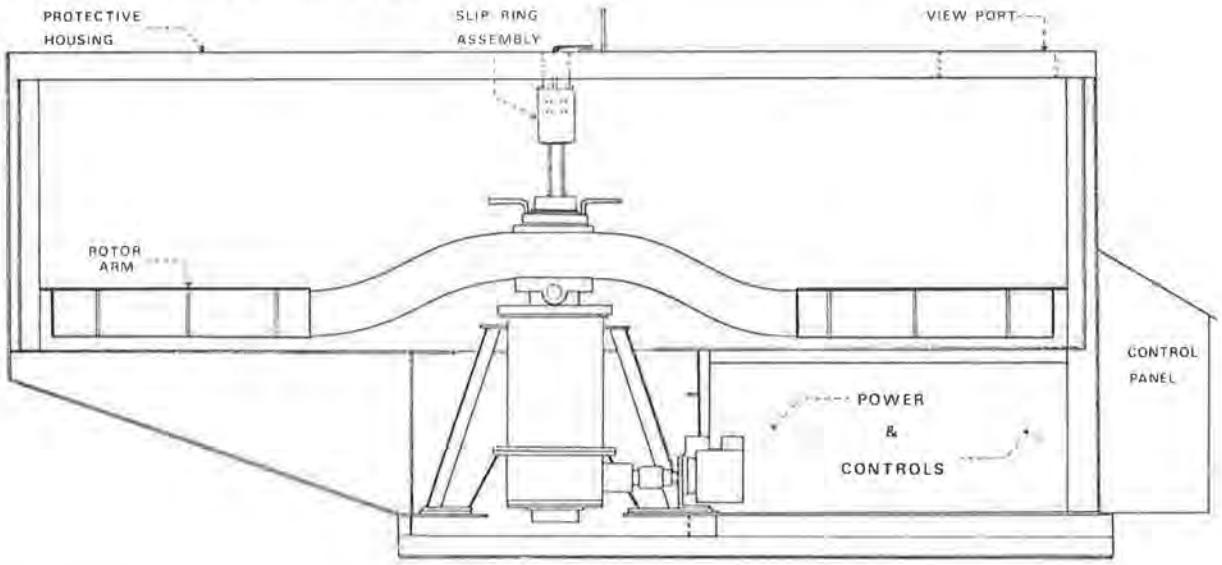

Figure 5. Schematic diagram of the centrifuge model.

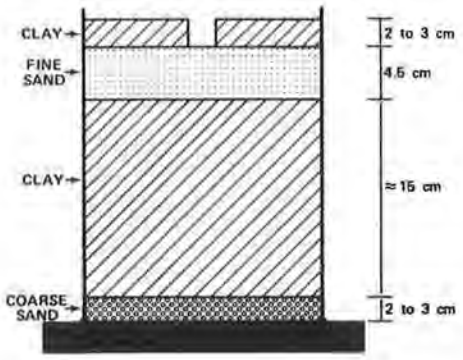

Figure 6. Relationships of stress versus deformation for model footings.

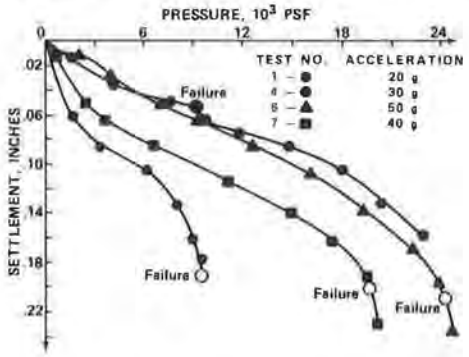

2.54-cm (1.0-in) linear variable differential transformer (LVDT). The model footing was an aluminum disk 19 cm in diameter to which sandpaper was glued to provide a rough contact surface.

SOILS AND MODEL PREPARATION

The clay base used in the models was kaolinite from Edgar, Florida; it had a liquid limit (LL) of 54 and a plasticity index (PI) of 24. The optimum water content was 26 percent. The sand used was an SP with D_{50} = 0.35 mm, e_{max} = 0.836, and e_{min} = 0.616. The ϕ-values determined by direct shear tests were 23° and 40° for the lowest and densest states, respectively. However, a correlation presented by Schmertmann (11) between ϕ and D_r was used to estimate ϕ for the model tests.

Model preparation consisted of placing the clay base into the model cylinder and statically consolidating the clay to a pressure equivalent to γHN (N = 50 g) by using a Tinius Olsen loading machine. To accelerate consolidation, a thin layer of coarse sand was placed in the bottom of the model container, and filter paper was placed over this sand. After consolidation (usually two days), the fine-sand upper layer was rained through a No. 30 sieve from a 1.5-m height. The sand layer was 4.5 cm thick, giving an H/B ratio of 1.5 as recommended by Tcheng (12).

Since the University of Florida centrifuge requires that the model container be mounted perpendicular to the radial acceleration plane, a thin layer of clay of 2-3 cm was placed on the clay surface to act as a membrane to prevent the sand from spilling out of the container. The influence of this layer was calculated as a surcharge. Figure 5 shows a sketch of the model after completion.

The soil weights and volumes were measured for each phase of model construction, and the corresponding densities of each layer were determined from them. Subsequent to each centrifuge model, test samples were taken from the clay layer and the unconfined compressive strength, water content, and density were determined. These values are presented in Table 1.

TEST PROCEDURES

Model tests were performed by assembling the loading piston and LVDT to the model footing, observing the zero readings, and accelerating the model to the test acceleration (either 20, 30, 40, or 50 g). The model was allowed to equilibrate for approximately 5 min at this acceleration, after which loading was initiated by supplying air pressure in 1-psi increments to the air piston, and the load and deformation values were recorded. Loading was continued until a sharp increase in deformation corresponding

Table 1. Summary of soil properties and model dimensions.

Test No.	Soil Property: Sand γ_s (pcf)	Sand D_r (%)	Sand ϕ[a] (degrees)	Clay γ_c (pcf)	Clay c[b] (psf)	Footing Dimension: Acceleration Level (g)	Prototype Footing Diameter B (ft)	Surcharge: Thickness (cm)	Surcharge γ_q (pcf)
1	98.3	73.6	37.8	105.2	178	20	2.0	1.9	112.5
4	91.5	16.8[c]	32.5	114.2	1440	30	3.0	2.8	123.8
7	104.0	114.5[c]	40.0	106.2	249	40	4.0	2.2	101.9
6	99.6	83.1	38.5	106.3	439	50	5.0	2.3	103.1

[a] From correlations by Schmertmann (11).
[b] Based on four U/C tests.
[c] D_r values appear in error.

Table 2. Comparison of calculated and observed bearing capacities.

Test No.	N_γ	N_q	N_c	D_f[a] (ft)	Sand[b] q_t (psf)	Clay[c] q_b (psf)	SK_s[d]	H (ft)	Calculated[e] q_o (psf)	Observed[f] q_o (psf)	Difference (%)
1	75.7	47.6	5.14	1.25	11 230	1238	6.8	2.95	9 575	9 135	4.6
4	32.7	24.6	5.14	2.76	11 070	9224	3.5	4.4	10 232[g]	9 410	8.0
7	109.4	64.2	5.14	2.87	32 183	7820	7.1	5.9	23 104	20 330	12.0
6	85.1	52.4	5.14	3.8	32 942	3095	7.1	7.4	28 074	24 450	12.9

[a] Surcharge thickness x g-level.
[b] Equation 6.
[c] Equation 10.
[d] Figure 4.
[e] $q_{to} = 1.2cN_c + 2\gamma_s H^2 (1 + 2D_f/H)\,[SK_s \tan\phi/B] + \gamma_q D_f$ (Equation 5).
[f] From Figure 6.
[g] Equation 5 + Equation 9 with $H_f/B \approx 2$.

to failure was observed. For the tests at highest accelerations, it was necessary to provide a balancing pressure to the air piston to prevent the increased weight of the footing and ram, prematurely loading the model. For these cases, the balancing pressure was adjusted to maintain the LVDT readings at their original null positions. A total of seven tests was performed, of which four were satisfactory

TEST RESULTS

The soil and model characteristics are listed in Table 1. The parameters used for calculating the bearing capacity and the calculated bearing capacities are compared with the observed values from the models in Table 2. Figure 6 presents the stress-deformation relationships for the various models as they were loaded in the centrifuge.

In all but test 4 (30 g), a punching failure occurred. Observations in the clay layer for all tests revealed a heaved section with a diameter of approximately 5B.

A comparison of predicted versus observed results presented in Table 2 shows excellent agreement. The difference was generally less than 20 percent; the best agreement was 4.6 percent for test 1. Considering the sensitivity of the SK_s and the bearing-capacity coefficients to ϕ, the agreement is well within engineering acceptance. For example, a value of $\phi = 37.8°$ instead of 38.5° (test 6) will result in a calculated bearing capacity of 22 794 psf or a difference of -7 percent for this test.

Two test conditions are modeled in this program. Tests 1, 6, and 7 are for a dense sand layer over a clay layer with varying values of cohesion. For these tests, a punching failure was observed. Test 4 represents a loose sand layer of a stiff clay, and no punching failure occurred for this test. The increased levels of acceleration (G) corresponded to an increase in model dimensions; thus prototype footings ranging from 0.6 to 1.5 m were modeled.

CONCLUSIONS

The generally good agreement between the test data and Meyerhof bearing-capacity theory indicates that the testing procedure developed is satisfactory for conducting centrifugal model tests to evaluate bearing capacity of footings.

The results show that, at least for the H/B ratio of 1.5, Meyerhof's bearing-capacity theory for layered soils is very good in spite of uncertainties involved in determination of the parameters used in his equation.

The results show clearly that for the tests at 20, 40, and 50 g, punching failure had occurred. But for 30 g, it seems that a lateral squeezing of the sand had occurred.

Because this study was of a preliminary nature, additional model tests involving different shapes and H/B ratios should be more thoroughly investigated.

ACKNOWLEDGMENT

The assistance of David Bloomquist in performing the centrifugal model tests and preparing this paper is acknowledged and greatly appreciated.

REFERENCES

1. S.J. Button. Bearing Capacity of Footings on a Two-Layer Cohesive Subsoil. Proc., Third International Conference on Soil Mechanics and Foundation Engineering, Zurich, Vol. 1, 1953, pp. 332-335.
2. A.S. Reddy and R.J. Srinivasan. Bearing Capacity of Footings on Layered Soils. Journal of Soil Mechanics and Foundation Division of ASCE, March 1967.
3. C.S. Desai and L. Reese. Ultimate Capacity of

Circular Footings on Layered Soils. Journal of Indian National Society of Soil Mechanics and Foundation Engineering, 1970.
4. J. Brown and G.G. Meyerhof. Experimental Study of Bearing Capacity in Layered Soils. Proc., Seventh International Conference on Soil Mechanics and Foundation Engineering, Mexico City, Vol. 2, 1969, pp. 45-51.
5. G.G. Meyerhof and A.M. Hanna. Ultimate Bearing Capacity of Foundations on Layered Soils Under Inclined Load. Canadian Geotechnical Journal, Vol. 15, 1978.
6. G.G. Meyerhof and A.M. Hanna. Ultimate Bearing Capacity of Foundations on a Three-Layer Soil, with Special Reference to Layered Sand. Cana-
7. P. Purushothamaraj, B.K. Ramiah, and K.N. Venkatakrishna Rao. Bearing Capacity of Strip Footings in Two-Layered Cohesive-Friction Soils. Canadian Geotechnical Journal, Vol. 10, 1973.
8. A.S. Vesić. Bearing Capacity of Shallow Foundations. In Foundation Engineering Handbook, H.F. Winterkorn and H.Y. Fang, eds., Van Nostrand Reinhold, New York, 1975.
9. G.G. Meyerhof. Ultimate Bearing Capacity of Footings on Sand Layer Overlying Clay. Canadian Geotechnical Journal, Vol. 11, May 1974.
10. A. Caquot and L. Kerisel. Traité de Méchanique des Sols. Gauthier-Villars, Paris, 1949.
11. J. Schmertmann. The Measurement of In Situ Shear Strength. State of the Art Presentation to ASCE Specialty Conference on In Situ Measurement of Soil Strength, Raleigh, NC, 1975.
12. Y. Tcheng. Shallow Foundation on a Stratified Soil. Proc., Fourth International Conference on Soil Mechanics and Foundation Engineering, London, Vol. 1, 1957, pp. 449-452.

Publication of this paper sponsored by Committee on Mechanics of Earth Masses and Layered Systems.

Field-Performance Comparison of Two Earthwork Reinforcement Systems

JOSEPH B. HANNON, RAYMOND A. FORSYTH, AND JERRY C. CHANG

A field-performance comparison of two different earthwork reinforcement systems constructed on Interstate 5 near Dunsmuir, California, is presented. Two mechanically stabilized embankment (MSE) walls and one reinforced-earth (RE) wall, all of comparable height, were constructed with the same type of backfill material. The MSE state system uses welded steel bar mats for reinforcement as compared with the flat steel strips of the proprietary RE system. All three walls were extensively instrumented. The steel stresses in the MSE bar mats were uniformly low; the maximum was 4 ksi as compared with the variable stress measured along the RE strips (9.3 ksi maximum). Erection times were comparable for both systems. The stress patterns developed in the MSE reinforcement tend to confirm the premise that MSE can be used with low-quality backfill, which would offer a significant economic advantage.

Construction experience in 1972 by the California Department of Transportation (Caltrans) with the first reinforced-earth (RE) wall in California suggested that alternative systems of soil reinforcement could possibly provide increased pullout resistance.

In 1973, a large direct-shear device was developed at the Transportation Laboratory of Caltrans to measure pullout resistance of various reinforcement systems, including the flat steel strips then used by the Reinforced Earth Company. The results, presented in some detail in 1977 (1), clearly indicated that the mat arrangement increased pullout resistance to an extent far in excess of that possible solely by friction between soil and earth. The failure mechanism observed involved the development of a passive pressure wedge of soil rather than the slippage or tensile breaks observed with the proprietary flat steel strips. This introduced the possibility of the use of a lower-quality backfill material, which, at given locations, could offer significant economic advantages.

During the design of the realignment and widening of I-5 near Dunsmuir, California, earthwork retention structures were found to be economically feasible at two sites. As a result of an agreement with the Reinforced Earth Company, the decision was made to construct a system designated as a mechanically stabilized embankment (MSE) that used bar-mat reinforcement with concrete facing for two walls at one location. At the second location, a proprietary RE wall with concrete facing would be constructed. The Dunsmuir project presented the initial opportunity to fully evaluate a prototype mat reinforcement system, including construction characteristics, response to load, cost, and corrosion resistance. In addition, it would be possible to compare the two systems on installations of approximately the same configuration and environment although somewhat differing foundation conditions. All three installations were instrumented to monitor stresses and deformations of these two soil-reinforcement systems. Instruments also monitored steel loss due to corrosion.

This report summarizes construction, instrumentation, field behavior, and cost data for the RE and MSE systems constructed at Dunsmuir. Detailed information on these aspects plus foundation conditions and design are covered in the final research report on the project (2).

GENERAL DESCRIPTION

The MSE system is a Caltrans development licensed under the Reinforced Earth Company patent in accordance with an agreement dated May 1976.

The two MSE walls on this project are located along the northbound lanes of I-5 below the Siskiyou Elementary School. The site, designated location A, consists of an upper and a lower wall. The upper wall, constructed between May and August 1976, is

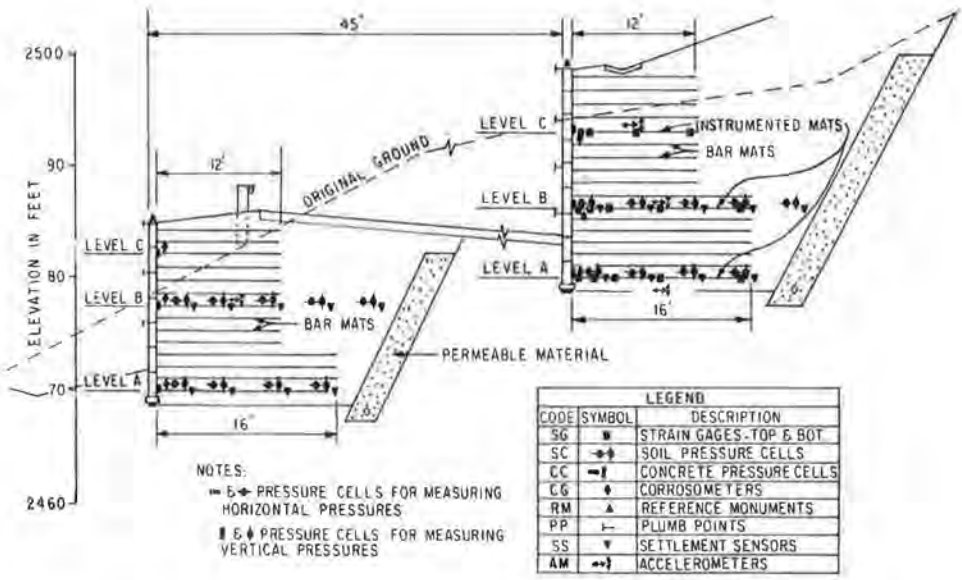

Figure 1. Typical section and instrumentation plan for MSE walls at location A.

located above a frontage road and serves as an earth-retaining structure for the slope below the Siskiyou Elementary School.

The upper wall has a maximum height of approximately 20 ft. The lower wall, which was begun in September 1974 and completed in October 1975, is located below the frontage road along the northbound lane of I-5. The maximum height of the lower wall is approximately 18 ft. Figure 1 shows typical sections of the two MSE walls together with the instrumentation plan.

The RE wall is a system of earthwork reinforcement in which internal stability is achieved through friction between flat steel strips and soil backfill. This system was developed in the 1960s by a French engineer, Henry Vidal (3), and is marketed in the United States by the Reinforced Earth Company of Washington, D.C.

The RE wall, located along the southbound lanes of I-5, was designated location B in the contract plans. The distance between locations A and B is approximately 2000 ft. The maximum height of the RE wall is approximately 20 ft. Figure 2 shows a typical section of the RE wall together with the instrumentation plan.

The material for the backfill for both locations A and B consisted of Class 4 (Type 1) aggregate subbase. Specification requirements and test results are shown in Table 1.

MSE WALL

External and Internal Stability

External stability for the MSE walls consisted of analyzing the resistance to both sliding and overturning for static and for earthquake conditions.

Once the requirements for internal stability have been satisfied, the MSE wall is presumed to act as a solid gravity mass; its weight resists the overturning moment produced by the earth pressure behind the gravity mass. Resistance to sliding is provided by adequate embedment depth to mobilize the shear strength of both the foundation and backfill materials. For preliminary analyses, the soil parameters used for the backfill were ϕ=35°, c=360 psf, and γ=130 pcf. Calculations of overturning moment and sliding resistance were made at depths below top of wall of 10 and 20 ft to evaluate the effects of reduced reinforcement lengths as shown in Figure 1. For the design of both MSE walls, advantage was taken of the gravity section design with reduced bar-mat lengths in the upper portion of the walls. The factors of safety were 2.0 or higher in all cases.

The stability of the foundation was analyzed by using ϕ=20°, c=1100 psf, and γ=120 pcf. The factors of safety exceeded 1.5 for sliding and 2.0 for overturning.

Horizontal earthquake acceleration of 0.2 g was also considered in a pseudostatic stability analysis that produced factors of safety exceeding 1.8. Internal stability was accomplished by longitudinal reinforcement by using sufficient cross-sectional area to preclude tensile failure with sacrificial steel for corrosion loss during the design life of the facility. The transverse members were selected to withstand pullout under an assumed pressure distribution.

Pull resistance was not a controlling factor in design of the bar-mat reinforcement since laboratory tests indicated that the bar mat has more than five times the pullout resistance than a corresponding surface area of flat steel reinforcing strips (1).

Embedment depth of the bar mat was determined from the requirement for external stability.

Corrosion

Before a decision on bar size could be made for the Dunsmuir walls, the metal losses throughout the design life of the structures required estimation so that sacrificial steel could be provided.

In underground metal facilities, such as gasand liquid-carrying pipelines where local pitting and eventual complete perforations can result in failure of the facility, the problem is of great concern. However, in buried load-bearing structures, such as piles or reinforcement, overall weight loss or average penetration was considered more critical than maximum penetration of pitting.

Tests on preliminary native soil samples of proposed backfill materials during the feasibility study produced a pH of 5.4 and resistivity of 17 000 ohm·cm and a pH of 5.8 and a resistivity of 30 000 ohm·cm. These results were determined from California Test 643. With this information as criteria, a rate of metal loss from pitting of 0.0018 in/year (1.8 mils/year) was assumed for preliminary design of the Dunsmuir bar mat based on corrosion of steel

culverts. For 50 years' service life, a total depth of metal loss was estimated to be 0.09 in in terms of surface pit development. However, corrosion parameters obtained from tests on progress samples of the actual backfill material during construction (Table 1) were a pH of 5.4 and resistivity of 8700. This equated to a much higher metal loss of 7.2 mils/year in terms of pit development or 0.8 mil/year of uniform surface loss. This rate, although in excess of the original estimated corrosion rate, was compensated for as indicated later. The chart in Figure 3 by Stratfull (4) presents the basic relationship used in the above test method and equates weight loss to surface pitting.

The final bar-mat design for resistance to tensile stress and the effects of corrosion called for 3/8-in-diameter bars at 6-in longitudinal spacing. The mats were 4 ft wide with nine 3/8-in-diameter bars to resist a maximum tensile load of 3.1 kips/mat and the corrosion rate of 0.0018 in/year for a 50-year life as estimated initially. The transverse bars were spaced at 1-ft 10-in centers for the longer mats and 2-ft centers for the shorter mats (Figure 4). The length of the mats was governed by previously described stability considerations. The final mat length was 10 ft for the top five panels and 15 ft for all panels below the top five or in excess of a 10-ft vertical wall height. The vertical spacing between mats was 12 in.

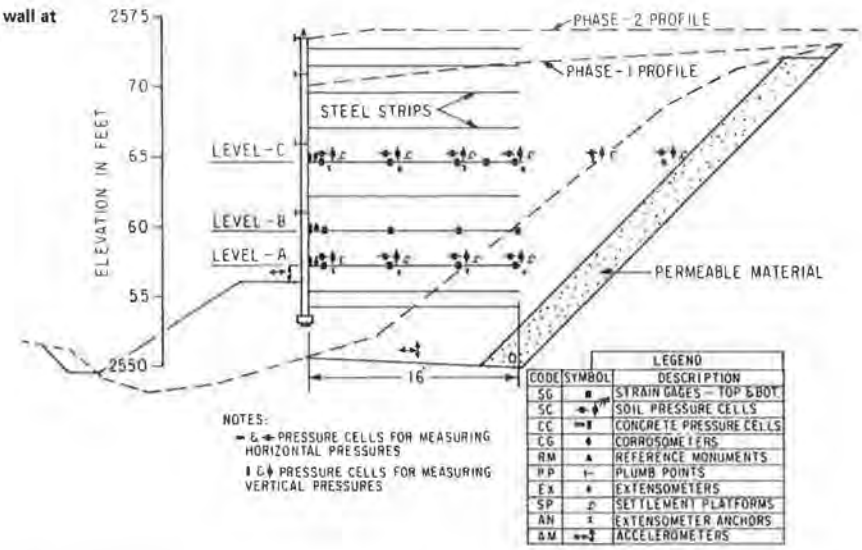

Figure 2. Typical section and instrumentation plan for RE wall at location B.

Table 1. Physical soil properties and shear strength of backfill materials for locations A and B.

Property	Proposed Material						Material Used[a] (74-1628, Sept. 1974)		Specification
	MM 08433, June 1971			73-1803, Dec. 1973					
	UU	CU Eff	CU Total	UU	CU Eff	CU Total	UU	CD	
Angle of internal friction ϕ (degrees)	24	33.5	15.5	35	33.0	10	34	36	
Cohesion C (psf)	2160	720	720	1150	400	1600	1000	200	
Plasticity index PI (%)		3			NP		5		
pH									
Resistivity (ohm-cm)		-			-		8700		
Sand equivalent		15			27		36		18 minimum
Maximum dry density (pcf)		116.8			77		94 (121 wet)		
Sieve size (% passing by weight)									
4 in		-			-		100		100
3 in		90			97		100		-
2½ in		86			94		97		-
2 in		83			92		97		-
1½ in		80			90		94		-
1 in		76			86		87		-
3/4 in		73			83		83		-
1/2		70			79		79		-
3/8 in		68			77		77		-
No. 4		65			67		74		30-94
No. 8		59			60		69		-
No. 16		55			52		64		-
No. 30		51			44		60		-
No. 50		47			33		54		-
No. 100		43			23		46		-
No. 200		38			15		39		0-29
5 μ		14			9		16		-
1 μ		6			4		-		-

Note: UU = unconsolidated undrained; CU Eff = consolidated undrained effective; CD = consolidated drained.

[a]Sampled from location B.

Concrete Facing

The connector and concrete facing design are covered in detail in the aforementioned final research report (2). The specific shape of the precast concrete panel that was finally used was the product of discussions with the contractor based on a cost-reduction proposal. The configuration ultimately selected was 2x12.5 ft, which allowed for four mats per panel (Figure 5).

Construction Operation

An unreinforced concrete leveling footing was placed in an excavated trench along the entire wall length at the prescribed foundation elevation to provide a level foundation for alignment control of face panels during erection. Handling and placement of the wall panels were accomplished with a small crane and two laborers. The wall panels were plumbed with wooden wedges, hammer, and level and were set to correct spacing. Placement time for one panel was approximately 5 min. Neoprene sheets 1/8 in thick and 3.5x12 in were placed on each shear key groove of the panels as a bearing pad between subsequent panels. The fill height was then raised to the elevation of the bottom mat connector holes in the panels.

Mats were then placed on the fill (Figure 6), and their threaded rods were inserted through the lower holes in the panels. Two washers and a nut were fastened to the end of each threaded rod, and a waterproofing sealant was pumped through the holes in panels between the washer and the outside wall face. The mats were then pulled back from the wall until the nut on the end forced the washers to rest tightly against the countersunk holes on the outside wall face. Backfill material was placed over the mats and compacted. When the backfill thickness was approximately 12 in over the mats, the nuts on the end of the threaded rods were tightened. The countersunk holes on the outside wall face were filled flush by using a cement grout mixture.

The maximum length of a row of panels was 469 ft and the minimum length was 37 ft. The average time required to place one panel height with its accompanying mats, backfill, and permeable drainage blanket behind the backfill was approximately 45 min.

A total of 11 working days was required to construct the lower wall, which was 455 ft in length and 18 ft in maximum height. The upper wall (406 ft in length and 20 ft in maximum height) was erected

Figure 3. Chart for estimating corrosion rate of steel buried in soil.

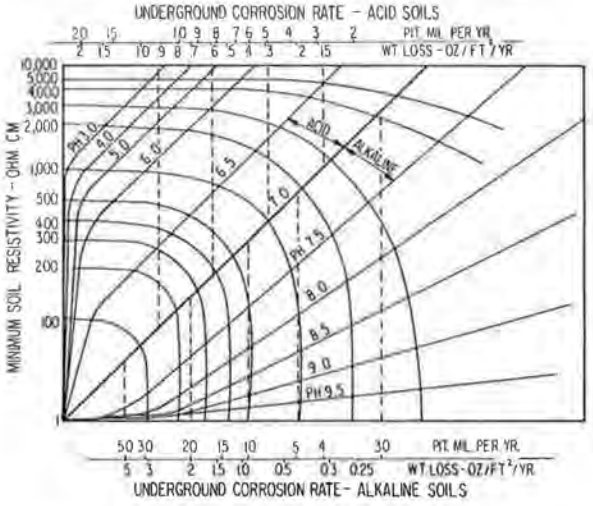

Figure 4. MSE bar-mat configuration and attachment to concrete facing.

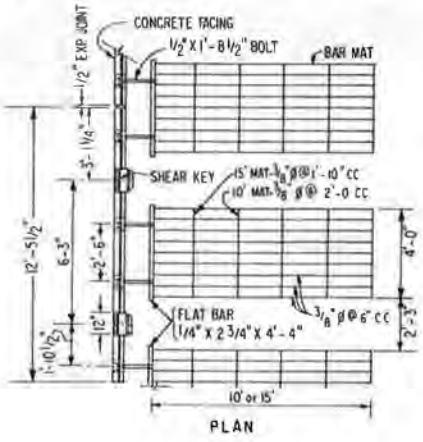

Figure 5. Isometric view, cross section, and typical stacking arrangement for MSE concrete facing panels.

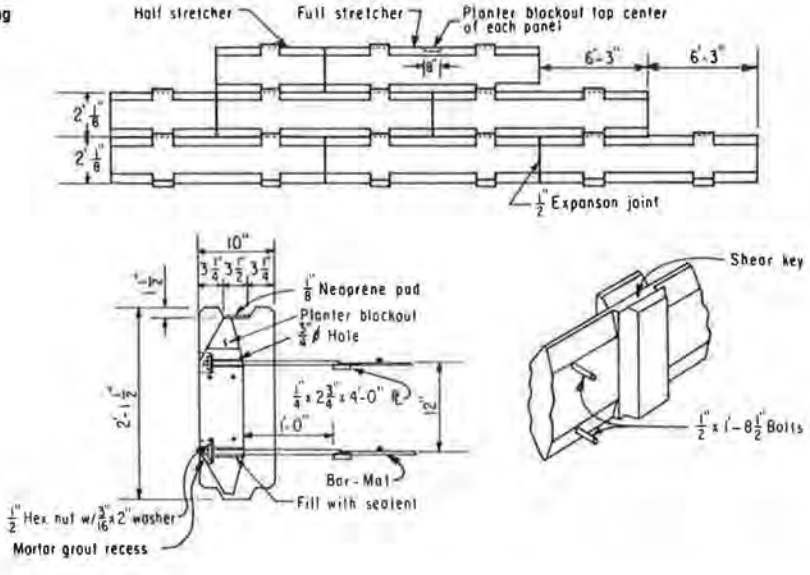

Figure 6. Steel bar mats for MSE in position on fill.

Figure 7. Completed MSE walls.

in 12 days. The completed installation is shown in Figure 7.

RE WALL

External and Internal Stability

External stability was analyzed by using triaxial strength properties for the foundation soils of ϕ=24°, c=200 psf, and γ=136 pcf. Factors of safety for the foundation soil exceeded 4.2. The gravity mass of the wall was designed with factors of safety that exceeded 1.5 for sliding and 2.0 for overturning.

Design of reinforcement for internal stability was accomplished by the Reinforced Earth Company. Smooth galvanized steel reinforcing strips 3 mm thick by 80 mm wide were used at a uniform 16-ft embedment depth. Lateral and vertical strip spacing was 3 and 2.5 ft, respectively.

Concrete Facing Panels

The precast concrete facing panels for the reinforced earth wall were as shown in Figure 8. They were approximately 5x5 ft in greatest dimensions and 7.5 in thick. Four types of panel elements were used.

Construction Operation

A nonreinforced concrete leveling footing was first placed along the entire wall location. Once the concrete footing had cured a minimum of one day, panel placement began; full and half-panels were alternated (Figure 8). Panel placement was accomplished by using a truck-mounted boom, hoist, and sling. As the panels were lowered into position, correction was made for horizontal distance between panels and their vertical alignment by using a spacer bar, crowbar, wedges, and level. Placement time for each panel was approximately 5 min. Once the backfill elevation reached the top of the half-panels, another set of full panels was introduced and held in position with clamps. Each clamp remained in place until placement of the next elevation of panels. As the fill elevation reached each level of tie strips on the wall panels, reinforcing strips were attached (Figure 9). Backfill placement was then continued to the next level of tie strips.

Figure 8. Typical layout for RE facing panels.

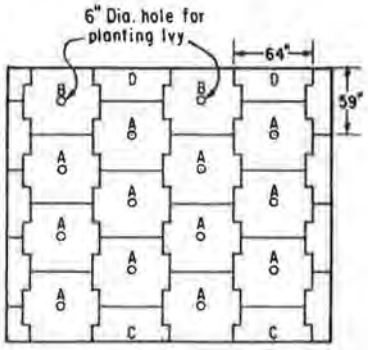

A 4-ft length of 1x4-in cork board was placed on the top edge of each panel without glue or adhesive. A 9-ft strip of 2x2-in Polyether foam, Grade 1035, was pushed into the vertical joints on the fill side by using a blunt-ended instrument (see Figure 9). The Polyether foam prevents fine particles in the backfill from washing through the joints but allows water to drain freely.

Backfill and permeable materials were transported to the wall site in bottom dumps and compacted with a 12-ton vibratory steel drum roller. Continuous grading and leveling by using a motor grader complimented the compaction operation. A water truck provided additional moisture. Laborers shoveled material larger than 2 in away from the wall face, and compaction along the edge of the wall was achieved by a small hand-operated vibratory steel roller. The completed wall is shown in Figure 10.

INSTRUMENTATION

Instrumentation for both reinforcement systems included (a) weldable strain gages with half-bridge circuits to determine the stresses developed in the bar mats and steel strips, (b) Magna corrosometer probes to measure corrosion rate of steel in a soil environment, (c) concrete pressure cells to measure horizontal soil pressures developed behind the concrete facing panels, (d) hydraulic and pneumatic soil pressure cells to measure soil stresses, (e) settlement platforms and mercury-pneumatic-type settlement sensors to measure vertical settlement within the backfill, (f) Statham accelerometers to measure dynamic response to steady-state vibration in a later testing program, (g) reference monuments to measure horizontal and vertical movement at the top and at the base of the walls, and (h) plumb points to measure horizontal and vertical movement at the face of the walls.

All instruments were read periodically during construction and after completion of construction through June 1978. Strain gages on the bar mats of the MSE walls were monitored through December 1980.

The final research report (2) presents the data

Figure 9. RE face panels held in position by wooden clamps with reinforcing strips attached.

Figure 10. Completed RE wall.

collected at both sites in detail. Only the more significant portions will be summarized here. Also, for purposes of comparing the responses of the two systems, only the data developed on the MSE upper wall will be presented, since they represent a loading condition similar to that of the RE wall.

Soil Pressure Against Concrete Wall Faces

The pressures at the wall face at both sites were measured by Carlson soil stress meters (concrete cells) at three levels. A plot of horizontal pressure versus height of overburden during construction can be seen in Figure 11. Here a best-fit line through the measured data points results in a maximum horizontal pressure at 20-ft overburden of about 4.2 psi for the RE wall, which is comparable with the pressure measured with the same overburden for the upper MSE wall.

The pressure values appear relatively consistent and conform to an active pressure state.

Reinforcement Stresses

To provide the basis of comparison, reinforcing steel stress levels from the RE wall and the MSE upper wall for the three instrumentation levels are superimposed on Figure 12. As shown, stresses in the MSE bar mats (maximum average of four gage locations) are uniformly low; the maximum is 4 ksi as compared with the variable stress measured on the RE strips (9.3 ksi maximum) at individual locations. Compressive stress was also measured on the RE strips near the face at level A, possibly a result of the toe buttress. The maximum connection-bolt stress for the bar mat was 6.65 ksi at level A following construction. However, this stress relaxed and stabilized at 4.5 ksi, which was similar to the maximum bar-mat stress at level A. The other MSE connection-bolt stresses at levels B and C also stabilized with a value similar to the bar-mat maximum stresses or went into compression. The overall long-term trend is a general relaxation of stress in the MSE system. The RE system showed minimal relaxation with time.

Figure 11. Horizontal soil pressure on wall face during construction of MSE and RE walls.

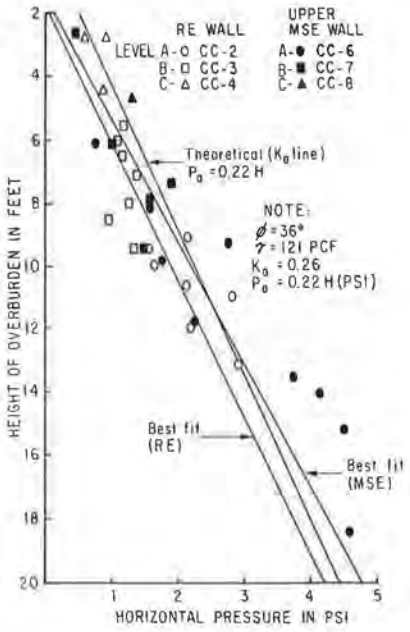

The stresses in the bar mats were also much more uniform throughout the depth of horizontal embedment than in the RE steel strips, possibly due to greater stiffness of the system. This characteristic will permit reduced steel quantities on future designs.

Pull Resistance of Reinforcement

The primary difference between the two systems constructed on this project was in the nature of reinforcement and, subsequently, pullout resistance and failure mode. Laboratory pullout resistance of the two types of reinforcement when Dunsmuir backfill material was used was measured in a series of tests with a large direct-shear device (1).

Test data pertinent to this report are presented in Figure 13, which shows load-deformation curves for a 3/8-in-diameter bar mat compared with those for three flat smooth steel strips of the same width and thickness used in the RE wall. Both reinforcement systems had the same area of steel exposed to soil for development of pullout resistance. Since tensile failure of the reinforcements did not occur, cross-sectional area was not critical.

The peak pullout resistance of the bar mat was 5.6 times that of the smooth steel strips with equivalent surface area (longitudinal plus transverse bars). These data and the results of tests on silty clay backfill presented in the aforementioned report clearly indicate that a lower-quality cohesive soil backfill would have been suitable for MSE walls.

The Reinforced Earth Company now uses a ribbed strip that provides some increase in pullout resistance. The ribbed strip was not tested as part of this study.

Corrosion Rate

As mentioned previously, corrosometer probes (CG) were installed behind the facing of the MSE and RE walls (Figures 1 and 2) to monitor and predict the uniform rates of corrosion and compare them with the rate estimated for design. The discussion below will cover both the upper and lower MSE walls as well as the RE wall.

In the lower MSE wall, Figure 14 shows a corrosion rate that varied with depth. CG 1 in level A corroded at a projected uniform rate of 3.4 mils/year, CG 2 in level B corroded at 1.5 mils/year, and CG 3 in level C corroded at 0.3 mil/year. The average rate for these three sensing probes is equal to 1.7 mils/year.

The upper MSE wall contained two corrosometer probes in each of its three levels (Figure 14). In level C, the two probes indicate a projected corrosion rate of 0.4 mil/year. This corresponds well with the 0.3 mil/year computed for level C of the lower wall. However, the pairs of probes in levels A and B of the upper wall gave projected corrosion rates that did not correlate well. Level B indicated a corrosion rate of 3.1 mils/year for CG 5 and 1.1 mils/year for CG 8. Level A resulted in 2.9 mils/year for CG 4 and 0.7 mil/year for CG 7. It should be noted that a different type of probe was used for corrosometers CG 4, 5, and 6 than for the other six sensing probes. Most of the sensors used a 4-mil corrodible element, whereas CG 4, 5, and 6 contained a 1-mil element. The results from the 1-mil elements are somewhat questionable due to their high sensitivity and short life. They may not, therefore, realistically reflect the long-term corrosion effects.

When all data are included, the average uniform corrosion rates in mils per year for each pair of probes were 1.8, 2.1, and 0.45 for levels A, B, and C, respectively. The average uniform corrosion rate for the upper wall is 1.5 mils/year.

If one considers the average uniform rates of 1.7 and 1.5 mils/year from the corrosometer probes in the lower and upper walls, respectively, projected uniform metal losses of 0.86 oz/ (ft^2·year) and 0.78 oz/(ft^2·year) are predicted. These values can be compared with the predicted corrosion loss in terms of pitting of 7 mils/year for the actual backfill sample. From corrosion criteria (Figure 3), this equates to a loss of 0.5 oz/ (ft^2·year) (pH of 5.4 and resistivity of 8700) for the composite

Figure 12. Comparison of steel stresses in earth reinforcement (RE and MSE walls).

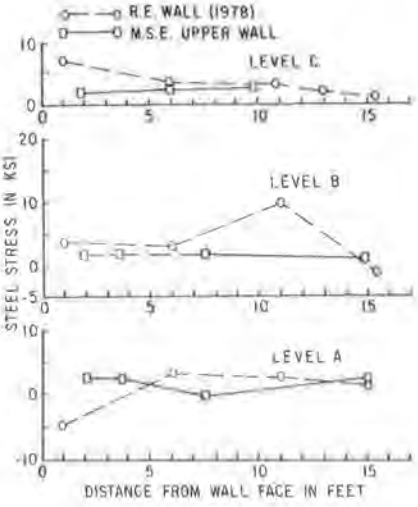

Figure 13. Laboratory pullout tests on steel strips and bar mat.

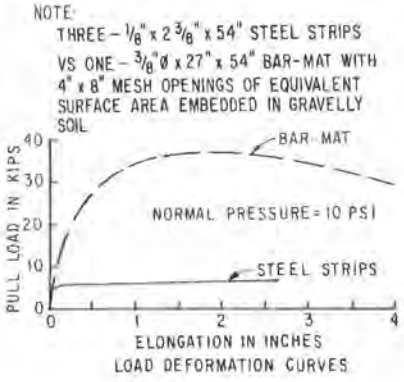

Figure 14. Estimated and actual corrosion rates, location A (MSE).

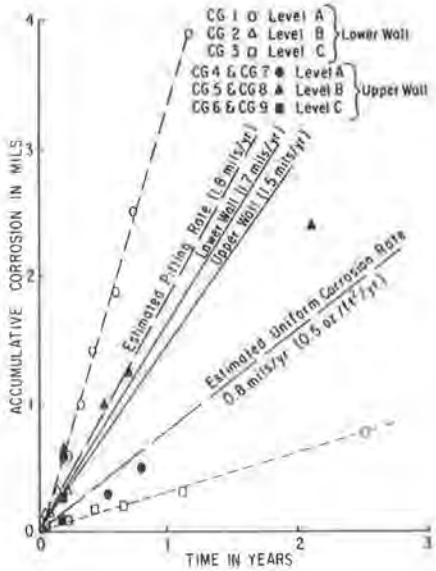

Figure 15. Estimated and actual corrosion rates, location B (RE).

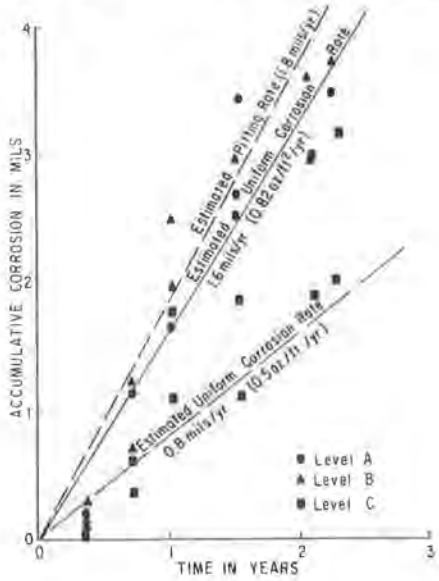

progress sample of backfill material. This is approximately 60 percent of the actual rates measured by the corrosometer probes.

Even though the above rates of metal loss are greater than the original estimated value, the 0.375-in-diameter bar mat is more than adequate for the actual field stress conditions. This bar mat will also provide sufficient sacrificial steel for the average measured uniform rate of 1.7 mils/year.

The corrosometer data also appear to indicate that corrosion rates increase with depth. This may be due to the phenomenon of corrosion stress; i.e., under greater pressures, the corrosion rate is increased. There may also be more moisture retained at the lower levels, which would tend to accelerate corrosion.

In April 1980, approximately 46 months after the completion of level C of the upper MSE wall, a segment of the bar mat at this level was retrieved for further corrosion analyses.

The bar-mat segment was covered with a light layer of rust. As stated previously, the average corrosion rate at this level of the embankment was 0.4 mil/year, which is about one-fourth of the entire MSE average. The analysis was limited to level C since no samples could be obtained from lower levels.

Various specimens were cut from the retrieved bar-mat segment for tests to measure weld shear resistance and tensile strength of the longitudinal reinforcement.

The results indicated that strength of the steel was virtually unchanged. Also, the welds' minimum shearing strength was 1800 lb, which is well above the approximate 70-lb design requirement (assuming a uniform distribution of stress throughout the bar mat). A microscopic examination of the light rust on the welds showed that it had not penetrated or weakened the welds or the mat.

The rate of corrosion at location B (RE) was measured in the fill by means of two corrosometers per level in levels A, B, and C. Since the same backfill material as that for the MSE walls would be used, a 1.8-mil/year rate of corrosion in terms of pitting was predicted initially from laboratory tests for pH and resistivity as defined previously.

Measured and estimated corrosion rates are plotted in Figure 15 for levels A, B, and C. Although the corrosion rates vary somewhat from those measured in the MSE walls, the average for all the gages is very nearly the same.

The average uniform corrosion rates at each level range from 2.0 to 1.18 mils/year for levels A, B, and C, respectively. The average of these rates is 1.6 mils/year [0.82-oz/(ft²·year) uniform rate], which is somewhat higher than the pitting rate of 7 mils/year [0.5 oz/(ft²·year)] estimated for the actual backfill samples.

CONSTRUCTION COST

A valid comparison of construction cost for MSE and RE walls on this project based on contract bid items is not possible due to the vagaries of the bidding process, construction timing (location A was constructed after location B), and the fact that location A was the first MSE project whereas the construction industry was generally familiar with RE projects. As an example, steel for the RE wall was bid at $0.53/lb as compared with $1.00/lb for the MSE walls.

If we take these factors into consideration, an appropriate means of developing a cost comparison of the two systems is believed to be quantities of principal items and erection time. Excavation quantity was not considered, since this was primarily dictated by site geometry rather than by system type. Also not included were items associated with the subsurface drainage since the same system was used for both RE and MSE walls.

Actual costs for wall facing for the two systems were closely comparable ($4.60/ft² for the RE wall versus $4.50/ft² for the MSE walls). To normalize the data for comparison, quantities are presented below by amount per 100 ft² of wall face; phase 1 of the RE construction involved 10 563 ft² and the lower MSE wall construction involved 5825 ft²:

Item	System	
	RE	MSE
Select backfill/100 ft²	80.5	89.2
Steel for reinforcement (lb/100 ft²)	490.5	946.2
Erection time (days/100 ft²)	0.27	0.19

These data indicate that reinforcement steel quantities for MSE walls per unit area of wall face were approximately double that of the RE wall due to the presence of the transverse members. In terms of erection time, the MSE wall was found to offer a slight advantage.

In assessing the relative costs of the two systems used on the project, two key factors should be borne in mind with respect to the MSE installation. First, a subbase-quality backfill was used on both systems for the purpose of comparing response to load. The results of laboratory pullout tests referred to earlier indicated that a low-plasticity ($PI \leq 10$) nonexpansive native material would have been satisfactory for the MSE installation. Also, the extremely low and relatively uniform steel stresses measured in the MSE installation indicate that No. 2 rebar (W5 wire) rather than No. 3 rebar (W11 wire) would have provided adequate tensile strength and a corrosion life equivalent to that of the RE strips. The use of No. 2 bars (W5 wire) would have resulted in a net reduction in steel quantity of 55 percent for the MSE project.

CONCLUSIONS

1. Horizontal pressure on the upper wall at location A (MSE system) and the RE wall at location B approximated the active Rankine state, which verified design theory.
2. The stresses in the MSE bar mats suggest a redistribution of stress in the reinforced soil mass and a uniformly low steel stress level at a maximum of 4 ksi as compared with the variable stress measured on the RE strips (9.3 ksi maximum). This is possibly due to the greater stiffness of the MSE system.
3. The extremely low and relatively uniform stresses measured in the bar-mat steel for the MSE system suggest that a 0.25-in-diameter rather than a 0.375-in-diameter bar would have been adequate for tensile strength and a corrosion life equivalent to that of the RE system.
4. Laboratory pullout tests suggest that MSE bar mats provide a pullout resistance that is greater than five times that of the smooth RE strips of the same surface area. These results also suggest that lower-quality backfill materials would be suitable for the MSE system.
5. Corrosion rates determined by corrosometer probes buried in the backfill soil were somewhat questionable and provided a poor correlation to predicted soil corrosion rate based on Caltrans steel-culvert criteria.
6. Both the MSE and the RE systems performed satisfactorily.
7. The MSE system will require more steel due to the presence of transverse members but can apparent-

ly be erected more quickly than the RE system can.

8. Where quality backfill would be a major cost item, the mesh (bar-mat) reinforcement could offer a significant economic advantage.

REFERENCES

1. J.C. Chang, J.B. Hannon, and R.A. Forsyth. Pull Resistance and Interaction of Earthwork Reinforcement and Soil. TRB, Transportation Research Record 640, 1977, pp. 1-7.
2. J.C. Chang, J.B. Hannon, and R.A. Forsyth. Field Performance of Earthwork Reinforcement. California Department of Transportation, Sacramento, Rept. CA/TL-81/06, 1981.
3. H. Vidal. The Principle of Reinforced Earth. HRB, Highway Research Record 282, 1969, pp. 1-16.
4. R.F. Stratfull. A New Test for Estimating Soil Corrosivity Based on Investigation of Metal Highway Culverts. Corrosion, Oct. 1961, pp. 115-118.

Publication of this paper sponsored by Committee on Mechanics of Earth Masses and Layered Systems.

Design and Construction of Fabric-Reinforced Retaining Walls by New York State

GARY E. DOUGLAS

The experience of New York State in the design and construction of two fabric-reinforced retaining walls is described. Crushed-stone fill is reinforced by horizontal layers of fabric placed at intervals dependent on the height of the wall, the strength of the fabric, and the internal friction angle of the fill. Design and construction procedures are detailed; the emphasis is on practical construction techniques. The design and construction are based on methods described by the U.S. Forest Service. The construction technique, although not commonplace, can be quickly mastered without special equipment or labor requirements. Instrumentation installed during construction to monitor vertical and horizontal movements indicates satisfactory performance 18 months after completion. The cost of this type of construction at this site compared favorably with alternative designs. Suggestions for cost reductions are offered for future installations, which may include embankment repair, similar to this project, or temporary works, such as construction detours.

New York State Department of Transportation (NYSDOT) has designed two retaining walls in which geotextile fabric is used as a reinforcing material. The walls, completed in August 1980, repair shallow failures in a side-hill embankment of NY-22 in Columbia County. The failures were observed in early 1976, when the easterly shoulder settled several inches in two areas 125 ft apart. The areas, designated A and B, extend for 110 ft and 150 ft, respectively.

A monitoring program was established in the fall of 1976 to measure any vertical or horizontal movements of the pavement, shoulder, and embankment slope. A subsurface investigation program was initiated in 1977; it consisted of a number of cased drill holes, one of which was converted into a long-term observation hole. The subsurface profile (Figure 1), determined from visual identification of soil samples and analysis of boring logs, shows 5-10 ft of loose clayey silt, sandy with gravel, overlying similar compact material; ledge rock is encountered at depths varying from 15 to 25 ft.

Movements up to 0.2 ft horizontally and 1.2 ft vertically, detected from September 1976 to April 1978, and distortion of observation hole casing at depths of 4-5 ft (see Figure 1) indicated a shallow failure in the loose material rather than a sliding failure along the rock surface. Subsurface water, due to side-hill seepage at area B and a broken box culvert at area A, was the primary cause for failure of the 1 vertical on 1.5 horizontal embankment slopes. This assumption was supported by the existence of 125 ft of unaffected 1 on 1.5 slope between the two failure areas and the natural flattening of slopes in the wet areas to 1 on 2.5.

The extent of the failures would have required remedial treatment beyond the capability of maintenance forces. Consequently, NYSDOT considered a number of design solutions. The criteria for an acceptable treatment included positive stabilization of the failure areas with low future maintenance, additional shoulder width, and safe traffic control during construction. Traffic restrictions by construction equipment and/or cost considerations eliminated a pile-and-lagging wall and extensive slope treatments. The earth-fabric wall concept was selected as the lowest-cost solution that met the criteria.

DESIGN

The design is based on methods described in a U.S. Forest Service publication (1, Chapter 5). The wall is designed as lifts of alternating fabric reinforcement and stone fill, as shown in Figures 2 and 3. The fabric within the theoretical failure zone cannot mobilize tensile strength to resist internal failure and is therefore discounted when the reinforcing length required is calculated. The fabric length embedded behind the theoretical failure plane is the fabric that reinforces the fill. The lift thickness is formed by the fabric, which overlaps the face of the wall and retains the fill material.

Site conditions controlled the length and the height of each wall necessary to stabilize the failure areas. The cross-section dimensions were determined to satisfy the internal and external stability of the wall. The minimum dimensions for internal stability were calculated with the strength parameters of the fabric and fill material by using appropriate factors of safety. These dimensions were increased to adequately resist lateral pressures acting on the wall, computed according to Rankine theory and the Boussinesq equation.

The reinforcing selected was Bidim C-34, a nonwoven, needle-punched, continuous-filament polyester fabric with high strength and permeability. The design tensile strength of 75 lb/in width of material represents approximately one-third the grab-test value (ASTM D-1117-69) reported by the manufacturer, a ratio that agrees with the Oregon State University ring-test results for other Bidim weights as report-

Figure 1. Typical subsurface profile at failure location.

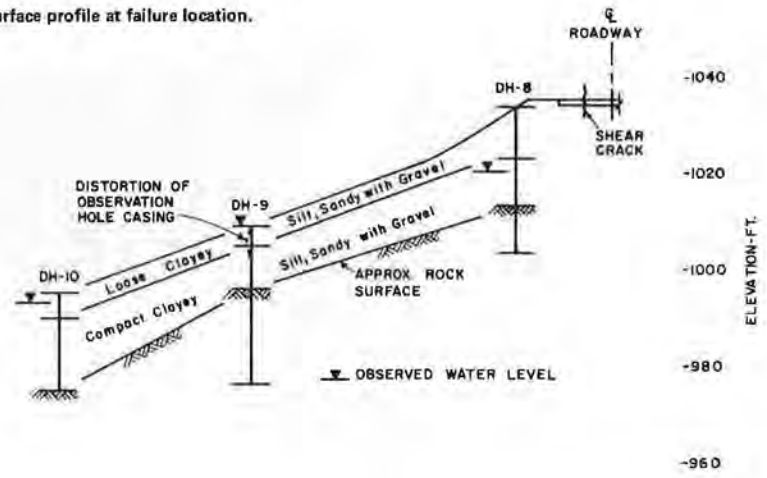

Figure 2. Typical lift detail.

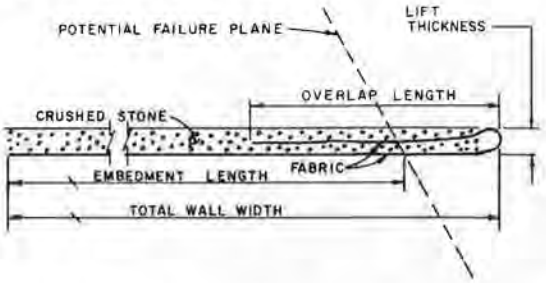

Figure 3. Typical wall section.

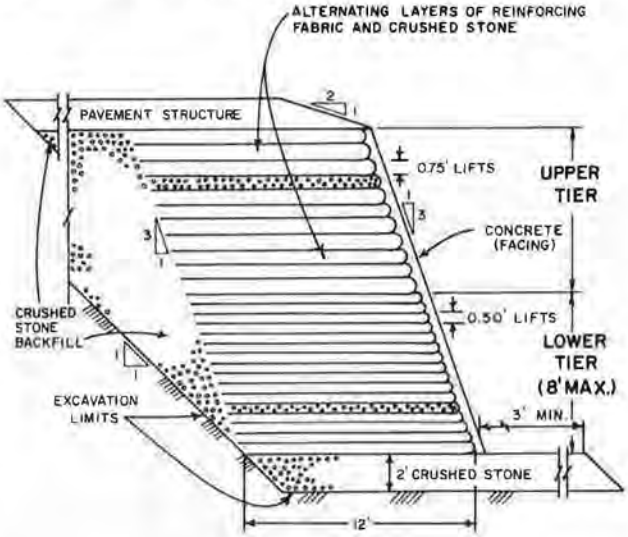

ed in the U.S. Forest Service publication (1). Crushed stone was selected as the fill material because of its high permeability and high angle of internal friction. The stone also develops high friction with the fabric, which is necessary to develop fabric tension.

The minimum dimensions calculated to satisfy internal stability did not satisfy the external requirements to resist sliding. This was primarily because of the low friction factor assumed between the fabric and the native material. The factor of safety against sliding was increased by widening the wall to gain mass and by placing a foundation of crushed stone 2 ft thick beneath the first lift to increase the friction factor. This crushed-stone layer also provided positive drainage for the wall and backfill.

The final cross-section dimensions, shown in Figure 3, were obtained by adjusting the calculated values to use the full manufactured width of fabric rolls, 17.4 ft. The wall was designed in two tiers, each with a different maximum lift thickness. The two-tier design was selected for practicality in construction, since the theoretical lift thickness may vary continuously with depth and pressure below the top of the wall. The overlap dimension was allowed to vary with the lift thickness to keep the wall width constant.

CONSTRUCTION

The site was prepared for wall construction by using normal clearing procedures. However, in the grubbing operation, care was taken not to disrupt the root systems of two large white pine trees adjacent to the limits of failure area A.

The excavation was progressed to the limits shown in Figure 3 while one-way traffic was maintained on the adjacent lane. The excavation was confined to one lane by using a 1 vertical on 1 horizontal backslope as the steepest allowable unbraced slope. The excavation was benched at elevations determined from analysis of boring logs and confirmed by field inspection to remove weakened material and establish the wall foundation on undisturbed compact soil. The transition between benches and the end slopes were 1 vertical on 2 horizontal.

An additional 2 ft of soil was removed below the base elevation and replaced with a crushed-stone foundation layer, as mentioned earlier. The excavation was continued at this elevation to the natural slope to provide a continuous drainage path from within and behind the wall. Wherever the distance from the toe of the wall to the existing slope exceeded 10 ft, French drains were installed, 20 ft on center, to provide positive drainage. This reduced the volume of excavation and stone backfill required. In area B, because of side-hill seepage, a separation layer of filter fabric was placed on the backslope of the excavation to prevent contamination of the stone backfill. Area A did not require this treatment because there would be no seepage after the culvert had been repaired under this contract.

This project incorporated recommendations from the U.S. Forest Service (1) to improve the temporary form. With the exception of placing the

crushed-stone foundation and drainage layer, the sequence for wall construction was also performed as recommended (1). The construction sequence consisted of the following steps, which were repeated in order until the wall reached full height:

1. The temporary form system was placed to line and grade (Figure 4);
2. The fabric was positioned and the excess was draped outside the form (Figure 5);
3. Crushed stone was placed to approximately one-half lift thickness and reached full thickness at the face (Figure 6);
4. The excess fabric was folded back to overlap the fill, and the lift was completed to full thickness, burying the overlap (Figure 7); and
5. The fill was compacted, and the temporary forms were removed (Figure 8).

The fabric was placed horizontally, with the long dimension parallel to the centerline. Crushed stone was placed by using one of several methods, depending on the work area available. First, the contractor tried end-dumping the stone and placing it by hand. This method, which proved to be too laborious and time-consuming, was quickly abandoned in favor

Figure 4. Placing temporary forms.

Figure 5. Positioning fabric.

Figure 6. Forming berm for overlap.

Figure 7. Burying overlap length.

Figure 8. Compacting completed lift.

Figure 9. Concrete finish on face of wall.

Figure 10. Typical slip tube.

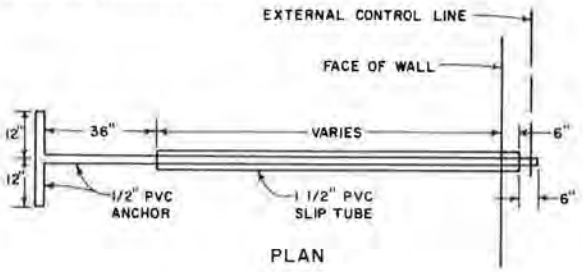

of dumping stone from a front-end loader and backblading it to the approximate thickness. Hand labor was necessary only to form the berm and overlap at the face. When the construction area increased sufficiently, the front-end loader supplied stone and a small bulldozer was used for grading.

Each lift was compacted by using a "walk-behind" (hand-guided) double-drum vibratory compactor with successive passes made parallel to the centerline that progressed from the backslope to the temporary form. When the work area increased, a small ride-on vibratory roller was used. Thorough compaction was desired at the wall face to minimize postconstruction settlements and horizontal movements in this area. However, the specified minimum of four passes was reduced to two passes when observations showed that the compaction effort was penetrating several underlying lifts. After the form had been removed, the vertical face gradually became curved as overlying lifts were compacted. Even when thoroughly compacted, the fabric at the face did not appear highly stressed and could actually be pinched by ordinary finger pressure.

The fabric was chosen mainly for its strength and permeability, although some resistance to ultraviolet deterioration was also desired. The maximum allowable exposure time for the fabric was specified as two weeks. However, for permanent protection, low maintenance, and protection from vandals, the wall face was covered with a mesh-reinforced pneumatically projected concrete. The reinforcing mesh, specified to be manufactured from No. 12 wires spaced 2 in in each direction, was supported by using No. 3 rebars inserted between layers to a depth of 3 ft. The bars were placed between layers during construction to form a grid measuring 3x3 ft. The mesh was included to minimize possible settlement cracks in the rigid concrete surface of the flexible wall (Figure 9).

INSTRUMENTATION

The walls were instrumented to investigate vertical and horizontal movement. Each wall was instrumented at the section of maximum height, which generally corresponded to the area of maximum past distress. Slope indicators and settlement devices were installed to monitor the behavior of the foundation soil. Slip tubes (Figure 10) were placed within the wall to detect lateral movements of the stone fill perpendicular to the wall face. The fabric was not instrumented. Minimal construction delays (typically only 0.5 h) were required to install a set of slip tubes or settlement devices that were prefabricated and installed by NYSDOT personnel. Installing the slope indicator casing, also done by NYSDOT, required several days of drilling. However, the contractor was able to schedule work without any conflicts.

Two settlement devices were installed under each wall 6 ft and 10 ft from the toe. The change in fluid level at the readout measures the cumulative foundation settlement. These devices measure the change to 0.01 ft, which is sufficiently accurate to detect significant movements.

The settlements measured during construction were less than 0.25 in. At wall B, the settlement measured one year after construction was 1.32 in at both devices. At wall A, settlements measured eight months after construction were 0.5 in and 0.25 in at the devices 6 ft and 10 ft from the toe of the wall, respectively. (These were the last measurements before the wall-A devices were vandalized.) These settlements have caused no noticeable effect on the roadway structure or the rigid concrete face.

The slope indicator casing was installed just outside the toe of the wall. The magnitude and direction of foundation movement with respect to depth can be measured as a change from the original slope of the casing. Foundation movements can thus be isolated, and any subsequent lateral movements detected by the slip tubes will indicate movement within the wall. Measurements made one year after construction indicate no significant foundation movement at either wall, which verifies the earlier assumption of a shallow failure.

A slip tube (Figure 10) is free to slide on an anchor rod that extends 3 ft beyond the tube. Internal horizontal movements of the fill are indicated by the change in distance between the end of the slip tube and a scribe mark on the inner rod. The scribe mark is referenced to an external control line. Thus, the relative movement and the absolute movement of the tube can be determined.

The tubes were installed in sets of four at various elevations to investigate the pattern of lateral movement. The tubes were buried 3, 6, 9, and 12 ft into the wall; each anchor rod is extended 3 additional ft beyond its respective tube. With anchors equal in length to the longer of the adjacent tubes, the wall is divided into several observation zones. Movements were compared within sets of tubes and with corresponding-length tubes at different elevations. Many tubes showed no movement, whereas others have not exceeded 0.25 in as late as one year after construction. Possibly, any short-term movements occurred during construction, before the control points had been set, or only small movements have occurred. Generally, the shorter tubes have shown the most movement, although continued monitoring may reveal a more definite pattern.

Figure 11. Stepping lifts to follow grade.

Figure 12. Bending wall to meeting existing slope.

LESSONS FROM FIELD EXPERIENCE

The contract plans originally specified crushed stone with a 2.5-in maximum size. A substitution was allowed at the contractor's expense to reduce the maximum size to 1.5 in. The smaller stone also provides a sufficient friction angle for this design but is easier to place by hand. This change, combined with improved handling methods developed during this project, increased the contractor's daily production. For example, exclusive of face treatment, the first wall, which has a surface area of 1630 ft^2, required two weeks for construction. The second wall, which has a surface area of 2100 ft^2, was also constructed in two weeks.

The fabric layers were placed horizontally without splices. Longitudinal splices were eliminated by designing the total fabric dimensions to equal the 17.4-ft roll width available commercially. Transverse splices were permitted if necessary by specifying a minimum overlap of 2 ft, or a 6-in minimum overlap, field-sewn double-stitched by using nylon or polypropylene thread. On this project, the contractor elected to place all lifts as a single piece of fabric. Consequently, we have no comments on the success or use of splices beyond the suggestion above regarding transverse splicing and a concurrence with others (1) that splices parallel to the wall face should be expressly prohibited.

Moisture was observed at the wall face before the fabric was covered with concrete. This was possibly due to surface water collecting in areas where irregular pockets formed in the fabric or perhaps where the fabric became clogged with rock dust. In future installations, placing the fabric horizontally in the longitudinal dimension should be considered, but the fabric should slope toward the rear of the wall for positive drainage, especially if the face treatment will be impervious.

Compaction vibrated some stone fill out of the open ends of lower lifts. This loss of fill was prevented by folding the fabric to form a bed corner (Figure 11). Figure 11 also shows how the upper lifts were stepped to follow the grade of the road. At the south end of wall A, each lift was folded to bend the wall back to meet the flatter existing slope (Figure 12). The north end of each wall intercepted the natural slope and was buried with light stone fill after the face treatment had been applied.

The rebar grid set for the reinforcing mesh required the addition of a top and a bottom row. These bars were installed after construction and had a minimal effect on the fabric. Future installations should specify a top and a bottom row of rebars. The 3-ft-square grid should be modified, perhaps by staggering alternate rows of rebars. Construction joints in the concrete face seem desirable to reduce cracking. Vertical construction joints, 50 ft on center, were included in the second wall.

The volume of concrete used on the facing exceeded the estimate by 40 percent, even with the thickness reduced from 3 to 2.5 in. This increase occurred because the ribbed surface of the wall and the wall batter formed a shelf between each lift.

COST

The cost, including items for excavation, fabric, stone fill, and concrete facing, was \$42/ft^2 of wall face. This exceeds the 1978 estimate by \$10/ft^2. This increase reflects the haul distance for the stone (35 miles) as well as the increased volume of concrete facing. The percentage breakdown by item was 10 percent for excavation, 30 percent for fabric, 40 percent for stone, and 20 percent for concrete.

CONCLUSIONS

Fabric-reinforced retaining walls can be built quickly and easily without unusual equipment or labor requirements. The wall can be shaped to the site by such methods as benching, bending, and stepping the lifts. The primary considerations in construction are compaction of the stone fill and drainage accommodations. The temporary forms necessary to confine the face area during compaction can be fabricated from common materials.

The instruments used were adequate to detect postconstruction movements. However, the slip tubes could not be adequately monitored during construction. Future installations should attempt to account for this condition or perhaps restrict observations to the external face of the wall. The arrangement with the contractor for installing instrumentation was satisfactory, since the instruments were prefabricated to minimize delay.

The cost of this project compared favorably with that of other alternatives at this site. Cost reductions are possible by using a cheaper fill material. However, positive drainage must be provided by using a very permeable fill or by constructing a permeable zone behind and beneath the wall. Also, a cheaper face treatment will reduce costs significantly.

ACKNOWLEDGMENT

I would like to acknowledge all the personnel of the Soil Mechanics Bureau who were involved in this project, especially B.E. Butler, V.C. McGuffey, A.R. Schnore, R.S. Grana, and E.A. Cardinal.

The efforts of M. Duval, engineer-in-charge for NYSDOT, and S. Cornell, supervisor for Schultz Construction, Inc., were uniquely responsible for the quality of the structure and the innovative solutions to field problems detailed here.

REFERENCE

1. J. Steward, R. Williamson, and J. Mohney. Guidelines for Use of Fabrics in Construction and Maintenance of Low-Volume Roads. Federal Highway Administration, U.S. Department of Transportation, Rept. FHWA-TS-78-205, 1978.

Publication of this paper sponsored by Soil Mechanics Section.

Stabilization of Wedge Failure in Rock Slope

DUNCAN C. WYLLIE

A wedge failure in a rock slope 21 m (70 ft) high was stabilized by unloading the top third of the failure, constructing a concrete wall to reinforce the toe, and installing tensioned rock anchors. Because the potential failure was located above a major railroad line, it was necessary to carry out this work with minimal interruption of traffic. This required careful blasting to ensure that the track below the slope was not damaged by falling rock and the use of equipment that would not block the track. The use of decision analysis to review the alternative stabilization methods and select the optimum method is discussed. The probabilities of slope failure, which were used as input in decision analysis, were obtained from a Monte Carlo analysis. The purpose of the Monte Carlo analysis was to quantify the uncertainties in the rock strength and structural geology parameters that were used in the design.

Stabilization of rock slopes above major transportation routes requires a high degree of reliability because failures that delay traffic can be extremely costly. For the same reason, the method of stabilization must allow the work to be carried out with the minimum disruption to traffic as well as be cost effective.

In this paper, the stabilization of a wedge failure of a rock slope above a heavily used railway is described. The unstable wedge was discovered during a routine preventive-maintenance program to scale loose rock from the face of rock slopes and to widen and deepen ditches. This program had been set up as a result of a survey along the entire mountainous section of the railway to identify and classify potentially hazardous slopes (1). At this location a tension crack had opened behind the crest, and excavation of accumulated debris at the toe of the slope revealed that the rock was heavily fractured and had moved as much as 300 mm (6 in). The unstable rock mass was defined by two intersecting joint planes that formed a wedge that could be analyzed by standard limit-equilibrium techniques (2).

The extent of the movement made it necessary that the wedge be stabilized as soon as possible. This work was made more urgent by the approaching winter, which would halt construction. These time restrictions made it impossible to carry out an extensive investigation program, so design work was carried out by using available data and previous experience in similar geologic conditions. In order to quantify the uncertainties in the input data, probability analysis was used in addition to the limit-equilibrium method as an aid in evaluating different stabilization options.

CUT SLOPE IN MASSIVE GRANITE

The wedge failure had developed in a rock cut 21 m (70 ft) high that had a face angle of 75°. The toe of the cut was within 6 m (20 ft) of the railway, so even a minor slope failure could reach the track. The rock type was a very competent, massive granite that was sufficiently strong not to be fractured by the stresses imposed by a slope of this height. However, the rock contained several sets of joints that were planar and had continuous lengths that often exceeded 3 m (10 ft) and were sometimes as long as 30 m (100 ft). These conditions meant that the volumes of unstable rock formed by these joints could be substantial.

Figure 1 shows the two joints that formed the base of the wedge and one of the near vertical joints that formed the tension cracks behind the crest. A stereographic projection of the two inclined joint sets and the slope face is shown in Figure 2. This shows that the line of intersection of joint sets A and B dips toward the track and is undercut by the face, so there is a potential for sliding to occur.

There were two contributory causes of instability. Excessively heavy blasting in the original excavation had fractured the rock at the toe of the slope and reduced the forces that resisted failure. It was also likely that water pressures in the slope could be substantial following heavy rainfall or periods of sudden snow melt. However, the slope would drain quickly because of the continuous open fractures in the rock and because the slope had been cut in a "nose" of rock that was free-draining on three sides.

BACK ANALYSIS OF EXISTING FAILURE

Although the orientation of the planes that formed the wedge could be determined with some confidence, there was no direct means of measuring the strength of the joint surfaces. There was insufficient time to carry out core drilling to obtain samples for laboratory testing, so back analysis was used to calculate the strength. The joints contained no in

Figure 1. Sketch of wedge failure.

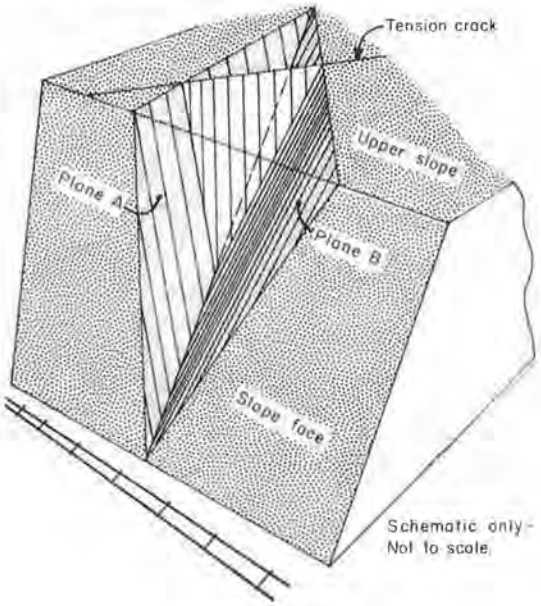

Figure 2. Stereographic projection of wedge geometry.

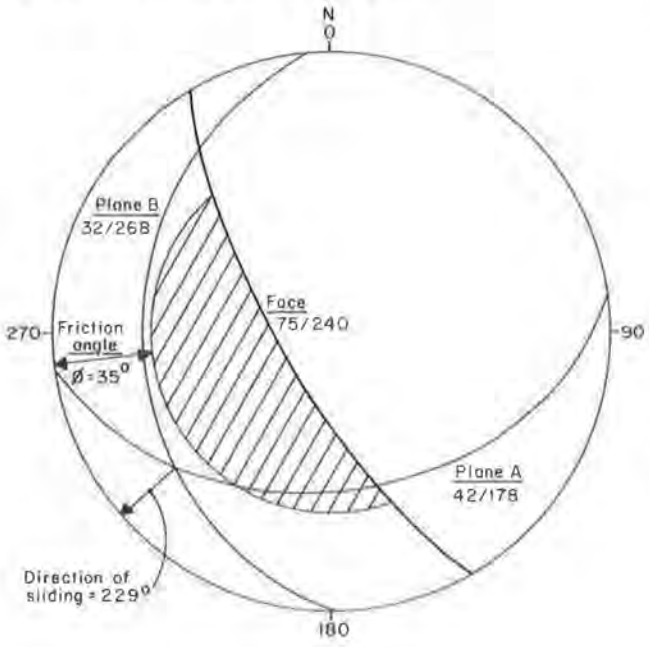

filling and were planar, so it was assumed that they had no cohesive strength and that the friction angle had a small roughness component.

The friction angle was determined by using a standard limit-equilibrium analysis for a wedge failure and varying the friction angle until the factor of safety equaled unity. It was assumed that the height of the water table was about one-half of the slope height. The limiting friction angle was found to be 35°, which is shown as a friction circle on the stereographic projection (Figure 2). This shows that, because the point of intersection of planes A and B lies outside the friction circle, the dry slope will be stable.

ALTERNATIVE STABILIZATION MEASURES

The objective of the stabilization program was to increase the factor of safety to 1.5. The alternatives considered were drainage, unloading, and bolting. The merits of these alternatives are discussed below.

Drainage

A fully drained slope would have had a factor of safety of 1.6. However, it was considered that the long-term reliability of horizontal drains to lower the water pressures was uncertain because if they became partly blocked, say with ice, high water pressures could build up in times of rapid snow melt or heavy precipitation. In addition, drainage through existing continuous open fractures was likely to occur naturally and drains would not improve the overall permeability significantly.

Bolting

In order to raise the factor of safety of the existing slope to 1.5 by installing bolts, a total bolting load of about 22 MN (5 million lb) would have to be applied. A bolting force of this magnitude would require the installation of a number of high-capacity, multistrand anchors. The holes for these anchors would have to be about 125 mm (5 in) in diameter. Drilling holes of this diameter in a near-vertical face while maintaining traffic would have been a difficult and expensive undertaking. Furthermore, the support system would rely on a few high-capacity anchors, failure of one of which would have produced a significant decrease in the support force.

Unloading and Bolting

Removal of the upper one-third of the slide and the installation of bolts with a total working load of about 5.5 MN (1.2 million lb) would increase the factor of safety to 1.5. This support force could be produced by using bolts with a working load of 450 kN (100 000 lb). The advantages of this system were that these bolts could be installed in holes drilled with hand-held equipment and that failure of a few bolts could not significantly decrease stability of the slope. However, the disadvantage was that the unloading operation would be slow. Only small volumes of rock could be moved in each blast in order to prevent damage to the track and to allow time for cleanup of broken rock between trains. It should be noted that the unloading operation alone does not increase the factor of safety in this condition where friction is the only factor contributing to the force that resists sliding. The effect of unloading is to decrease the required bolting forces to achieve the required factor of safety.

STABILIZATION PROCEDURE

The following is a description of the unloading and bolting operation used to stabilize the slope (Figure 3).

Unloading the top 9 m (30 ft) of the slope was carried out by a four-person crew who used hand-held pneumatic equipment to drill blast holes. The blasting was carefully controlled to ensure that there would be no further damage to the rock, and smooth-wall blasting was used on all final faces. This technique consisted of drilling holes parallel to the final face on a 750-mm (30-in) spacing that were lightly loaded by using wooden spacers between

half sticks of explosive. This produced an even distribution of explosive load equivalent to about 0.34 kg/m² (0.07 lb/ft²) of face. The holes were detonated on a single delay to ensure that the rock broke on the line defined by the holes. Before each blast the track was protected from falling rock with a 1.2-m (4-ft) layer of gravel. In this manner about 1150 m³ (1500 yd³) of rock were removed.

The bolting operation was carried out as follows. The rock at the toe of the slope was so highly fractured that the installation of bolts, which produce highly concentrated forces, would have been insufficient reinforcement. Therefore, a reinforced concrete wall 9 m (30 ft) high was poured at the toe to act as a massive bearing plate for the rock bolts and distribute the stabilizing load into the slope. Plastic pipes, at the required orientation of the bolts, were cast into the concrete to facilitate later drilling of the bolt holes.

All the rock bolts were 6-m (20-ft) long continuous threadbar that had grout anchors. The anchorage length of 2.4 m (8 ft) was determined by using the assumption that the rock/grout working-bond strength was 1.2 MPa (170 psi) (3). The bolts were tensioned by using a hydraulic jack before the bars were fully grouted to lock in the tension and provide corrosion protection. Five of the bolts were installed through the wall and the remainder in the sounder rock above.

Figure 3. Section through failure showing stabilization procedures.

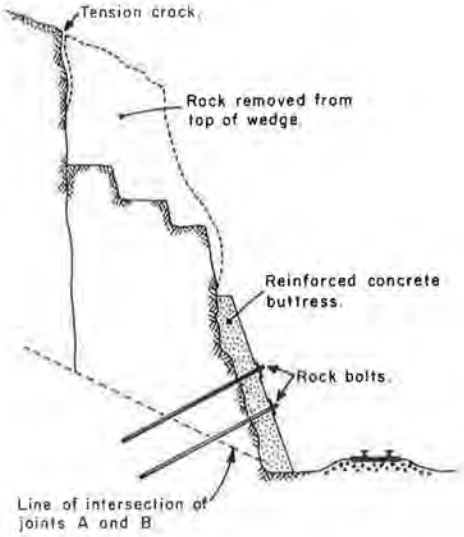

COMPARISON OF ALTERNATIVES BY DECISION ANALYSIS

The following is a description of how decision analysis (4-6) can be used to determine whether a stabilization program was economically justified and, if so, which has the optimum program.

Decision analysis involves examining the probabilities and associated costs of the various possible events that can occur for each alternative course of action. These probability and cost figures are used to calculate the expected cost for each alternative so the alternative with the lowest expected cost can be determined. The value of decision analysis is that the designer must quantify his or her uncertainty in the design and the owner must evaluate the consequences of failure. There is then a rational basis for comparing alternative courses of action.

The first step in the analysis is to draw a decision tree that shows the decisions that can be made and the events that can arise from these decisions. Figure 4 shows the three options:

1. No stabilization work,
2. Installation of bolts, or
3. Unloading and installation of bolts.

Whichever option is selected, the same events can

Figure 4. Decision tree that shows stabilization options and expected costs.

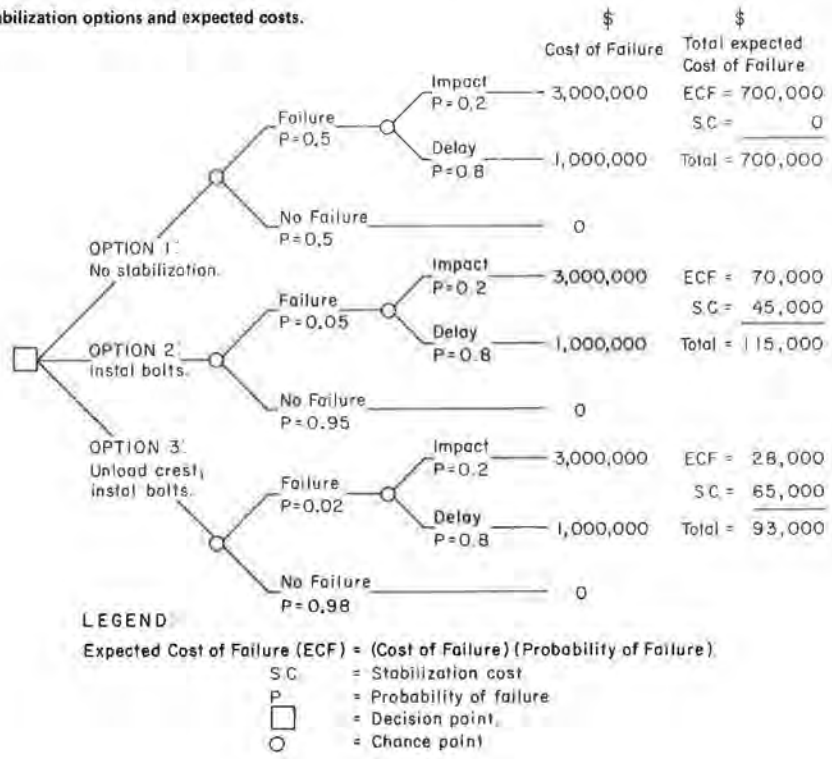

occur. Namely, a failure will or will not occur, and if failure does occur, there is the possibility either that it will cause a delay or that a train will hit the fallen rock. The difference among the three options is the probability with which the events take place.

Probabilities of Failure

The probabilities are estimated in two ways. The probabilities of slope failure are calculated by using Monte Carlo analysis (7,8), whereas the probability of a delay or impact is determined by examination of previous failure records.

Monte Carlo analysis involves giving a range of values to all those parameters in an analysis that cannot be determined precisely. A random number is then generated that is used to select a value for each of the variable parameters. These values are input to the stability analysis to calculate the factor of safety of the slope. A new random number is then generated and the calculation procedure is repeated until several hundred factors of safety have been determined. The proportion of the number of times that the factor of safety is less than unity is the probability of failure; i.e., if 10 out of the 100 trials have factors of safety less than unity, the probability of failure is 10 percent. A probability of 50 percent is synonymous with a factor of safety of 1.0.

In the stability analysis of the wedge failure, triangular distributions were assumed for those parameters the precise value for which was in doubt. The triangular distribution was defined by a mean value, which was the most likely value, and by upper and lower bounds, which are the expected extreme values (Figure 5). Because limited field and laboratory work had been carried out, judgment based on previous experience in the area was used to select these distributions. It was assumed that the extreme values for the dip direction of the joints were ±15° of the mean value, whereas the extreme values for the dip and friction angle of the joints were ±5°. The possible variation in water pressure was between one-quarter and three-quarters of the slope height.

In the case of the support by the bolts, it was also assumed that it was possible that they could produce more support than the nominal working load but also that some of the bolts could fail. The slope geometry and water and rock densities were given point values in this analysis.

Figure 6 shows a typical result of the Monte Carlo analysis. The X's represent the results of each stability analysis. Out of 100 analyses, 8 had factors of safety of less than unity, so the probability of failure is 8 percent. The probabilities of failure calculated in this manner are shown on the decision tree. The probability of failure of option 3 (unloading and bolting) is lower than that of option 2 (bolting only) because there is no uncertainty in decreasing the slope height, whereas rock bolts can fail.

Figure 5. Triangular distribution of dip angle of plane A.

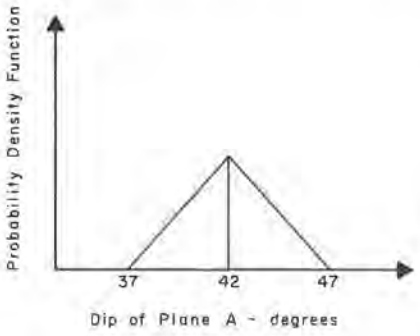

Figure 6. Calculation of probability of failure by using Monte Carlo analysis.

```
-----------------------------------------------
FREQUENCY DISTRIBUTION OF FACTOR OF SAFETY VALUES
-----------------------------------------------

                    FREQUENCY
                    0        10        20        30        40        50        60
 CLASS   INTERVALI.........I.........I.........I.........I.........I.........I.......
 1    .73    .79 .XX
 2    .79    .86 .XX
 3    .86    .93 .XX
 4    .93    .99 .XX
 5    .99   1.06 .XX
 6   1.06   1.12 .XXX
 7   1.12   1.19 .XXX
 8   1.19   1.25 .XXXX
 9   1.25   1.32 .XXXXXXXXX
10   1.32   1.39 .XXXXXX
11   1.39   1.45 .XXX
12   1.45   1.52 .XXXXXXXXXX
13   1.52   1.58 .XXXXXXXXXXXXX
14   1.58   1.65 .XXXXXXXX
15   1.65   1.71 .XXXXXXXXXXX
16   1.71   1.78 .XXXXXXX
17   1.78   1.85 .XXX
18   1.85   1.91 .XXXX
19   1.91   1.98 .XXXXX
20   1.98   2.04 .X
                 I.........I.........I.........I.........I.........I.........I.......
                 0        10        20        30        40        50        60

-----------------
SAMPLE STATISTICS
-----------------
MEAN= 1.481    S.D.= .295    SKEWNESS= -.248    KURTOSIS= 2.75    SAMPLE SIZE= 100

----------------------
PROBABILITY OF SLIDING
----------------------
P.F.= 5.17 :  BASED ON SAMPLE OF KINEMATICALLY VALID CASES AND ASSUMING THAT IT IS
              NORMAL WITH MEAN = 1.481 AND STD. DEV. = .295
P.F.= 8.00 :  BY COUNT WHERE KINEMATICALLY IMPOSSIBLE CASES ARE CONSIDERED TO BE SAFE
              ***NUMBER OF SUCH CASES WERE    0
```

Expected Costs

The next step in the decision analysis is to determine the expected costs of failure (ECF) of each alternative. Expected costs are the product of the cost of that event and the probability of its occurring. The costs of failure, i.e., $1 million for a delay and $3 million for an impact, are estimates based on likely delay times, injuries, damage to track and equipment, cleanup of rock, and slope stabilization. Indirect costs such as legal fees and insurance premiums should also be included in the costs of failure. The expected cost of failure for each alternative is shown on the decision tree (Figure 4).

The final step in the analysis is to determine the likely cost of implementing each decision, i.e., the stabilization costs. The costs are estimated from previous construction projects and are added to the expected cost of failure. As shown on the decision tree, the most effective means of stabilization is to unload the crest and install rock bolts, even though this is more expensive than bolting only. This shows the sensitivity to expected costs of the probability of failure.

CONCLUSIONS

In this paper, use of both limit-equilibrium and probability methods to design stabilization measures for a wedge failure in a rock slope is described. The advantages of using both methods are that limit-equilibrium analysis has been well proved in rock engineering practice, whereas probability analysis allows the designer to assess the effect of uncertainty in the input data on the design. The calculation of the probability of failure of the slope for different courses of action allows the relative merits of the alternatives to be evaluated. The use of decision analysis requires an assessment of the consequences of failure, which can involve the owner in the decisionmaking process.

REFERENCES

1. C.O. Brawner and D.C. Wyllie. Rock Slope Stability on Railway Projects. American Railway Engineering Association, Vancouver, Canada, 1975.
2. E. Hoek and J. Bray. Rock Slope Engineering, 3rd ed. IMM/North American Publications Center, Brookfield, VT, 1981.
3. G.S. Littlejohn and D.A. Bruce. Rock Anchors--State of the Art. Ground Engineering, May and July 1975, May 1976.
4. D.C. Wyllie, N.R. McCammon, and W. Brumund. Planning Slope Stabilization Programs Using Decision Analysis. TRB, Transportation Research Record 749, 1980, pp. 34-39.
5. H. Raiffa. Decision Analysis. Addison-Wesley, Reading, MA, 1970, 309 pp.
6. S.O. Russell. Civil Engineering Risks and Hazards. The B.C. Professional Engineer, Jan. 1976.
7. Pit Slope Manual. Canada Centre for Mineral and Energy Technology, Ottawa, Ontario, Canmet Rept. 77-5, 1977, Chapter 5.
8. D.L. Pentz. Slope Stability Analysis Techniques Incorporating Uncertainty in Critical Parameters. Proc., Third International Symposium on Stability in Open Pit Mining, Vancouver, B.C., American Institute of Mining Engineers, New York, 1981.

Publication of this paper sponsored by Committee on Soil and Rock Properties.

Repetitive-Load Behavior of Unsaturated Soils

E. SABRI MOTAN AND TUNCER B. EDIL

The resilient and residual deformation behavior of a number of soil samples under unconfined repetitive loading was investigated in the unsaturated state as a function of matrix suction. Matrix suction values within the range of 50-1500 kPa were achieved by using pressure-plate extractors. Results obtained during the first phase of the study on low-plasticity sand and clay mixtures are extended to high-plasticity clay during the second phase after a series of repetitive-load tests on statically compacted samples of grundite at both dry- and wet-of-optimum compaction moisture content. The resilient modulus is shown to be related to the matrix suction in a rather unique form for all soils tested; the maximum is at 800 kPa suction and it decreases thereafter and subsequently increases again significantly at very high suction values (as in the air-dried or oven-dried state). This maximum resilient modulus obtained at 800-kPa suction increases with decreasing plasticity index. The position and the form of the curve of resilient modulus versus matrix suction may undergo changes if deviator stress and confining pressure are introduced as variables. It is also shown that the resilient behavior of cohesive soils does not follow the same pattern as the relationship of unconfined strength versus suction beyond a suction value of 800 kPa. Furthermore, the postrepetitive testing unconfined strength of dry- and wet-of-optimum compacted samples seems to be better correlated with the moisture content than with the soil suction value.

The critical role of moisture in controlling the mechanical behavior of partly saturated cohesive soils through changes in the state of stress in soil and its modifying effects on the soil fabric have been well recognized. Strength and deformation characteristics of saturated soils can be related consistently to the stress state in the soil skeleton through the use of the effective-stress principle. However, in partly saturated soils, with decreasing degree of saturation, the evaluation of the effective stresses becomes less and less reliable due mainly to experimental difficulties. At low degrees of saturation, soil suction, which is the only measurable soil-water stress parameter, can be used analogous to the effective stress in saturated soils. The use of soil suction here as the critical soil-moisture parameter instead of the water content is also supported by the dependence of the consistency limits of cohesive soils of different origins on the stress conditions in soil water rather than on the amount of water.

Partly saturated soils usually do not create critical bearing-capacity problems. However, the magnitude of the recoverable (resilient) and irrecoverable (residual) deformations in base-course and subgrade materials caused by repetitively applied traffic loads is the basic concern in flexible pave-

Table 1. Soil properties.

Series	Soil	Liquid Limit (%)	Plastic Index (%)	AASHTO Classification	Unified Classification	Maximum Dry Unit Weight (kN/m^3)	Optimum Moisture Content (%)
1	Fayette silt loam[a]	39	18	A-6 (11)	CL	18.2	18.2
2	Sand mix[b]	33	12	A-6 (9)	CL	18.3	15.5
3	Sodium grundite[c]	55	27	A-7 (18)	CH	16.1	21.7
4	Calcium grundite[c]	54	26	A-7 (18)	CH	16.4	21.0

[a]Vernon County, Wisconsin.
[b]Mixture of 75 percent Fayette silt loam and 25 percent Keweenaw loamy sand from Douglas Co., Wisconsin.
[c]Sodium and calcium surface-saturated fraction of grundite passing No. 200 sieve, respectively.

ment design methodology. Soil failure in this context is described as the accumulation of excessive residual deformations in soil, which may not necessarily be the result of a shear failure.

Strength and deformation characteristics of compacted and consolidated cohesive soils subjected to repetitive loading have been documented as functions of water content and soil suction value by many researchers (1-7). One of the earliest studies reported (8) indicated a steep rise in the resilient modulus of a till and a corresponding drop in the residual deformation with decreasing water content at wet-of-optimum and more gradual changes at dry-of-optimum. Richards and others (9), measuring the suction in a subgrade soil by psychrometers, looked for a possible correlation between the deformation characteristics of compacted laboratory samples and those of the subgrade soils as a function of soil suction. Richards and Gordon (10) observed a linear correlation between the soil suction and the resilient modulus on a logarithmic plot. Shackel (11) indicated a slight dependence of soil suction on dry density and observed a decrease in soil suction during repetitive loading. Fredlund, Bergan, and Sauer (12) proposed a set of stress-state variables--confining pressure, deviator stress, and soil suction--controlling the deformation characteristics of a soil under repetitive loading. Later, Fredlund, Bergan, and Wong (13) gave equations relating the resilient modulus to deviator and confining stress through a set of parameters that are functions of matrix suction. Edris and Lytton (14) reported negligible changes in the resilient modulus of three different soils (with group symbols of ML, CL, and CH according to the Unified Soil Classification System) at psychrometrically measured initial total suction values higher than those corresponding to moisture content at approximately 2 percent dry-of-optimum. Luh (15) reported a tendency in the dynamic shear modulus of kaolinite specimens tested in a resonant column apparatus to increase substantially up to 400 kPa, which was followed by a decrease at 800 kPa. The drop in the shear modulus at 800 kPa was attributed to the formation of microcracks at high suction levels.

In this study, the response of soil under unconfined repetitive loading has been investigated as a function of matrix and total suction values on a number of cohesive soils over a range of plasticity characteristics. Consideration was given to the dependence of the resilient modulus and residual deformation of soils tested on the matrix component of the total suction values along with the modifying effects of the osmotic component, if any, on the soil behavior. The possible existence of a unique set of curves relating the resilient modulus to the matrix suction was investigated in particular.

EXPERIMENTAL PROGRAM

Soil Properties

Four series of compacted specimens were prepared for repetitive testing (Table 1) by using three different soils.

Sample Preparation and Moisture Equilibration

For series 1 and 2, three sets of samples were prepared by using a Harvard miniature compactor at the optimum moisture content and 2 percent dry- and wet-of-optimum (16). For series 3 and 4, two sets of samples were prepared at 2 percent dry- and wet-of-optimum moisture content by using static compaction and a compaction mold similar to that described by Shackel (17).

All the samples were placed on saturated ceramic plates in pressure extractors and permitted to absorb as much water as possible under atmospheric pressure. In series 3 and 4, sodium and calcium chloride were added to water saturating the extractor plate to minimize the water transfer between the plate and the samples through osmotic processes. Subsequently, all samples were moisture-equilibrated in extractors along a desorption cycle by increasing the applied air pressure in steps to achieve matrix suction values of 50, 100, 200, 400, 800, and 1500 kPa, and a number of them were tested under repetitive loading after equilibration at each step (16). At equilibrium, the moisture remaining in the soil specimen is in equilibrium with the applied air pressure, which has a value corresponding to the matrix suction component of the total suction. Total suction, which can be directly measured by using a psychrometer, is the sum of the matrix and osmotic components. Some of the samples in series 3 and 4 were further dried over a sulfuric acid solution in a desiccator to moisture contents lower than those corresponding to 1500-kPa suction prior to repetitive loading in order to examine the soil behavior at suction values beyond 1500 kPa (at an estimated matrix suction of 9000 kPa). A moisture sorption cycle (400 and 100 kPa) was also followed in series 3 and 4. In addition, three samples that were previously tested were retested subsequent to oven drying, which resulted in very large suction values.

Repetitive Loading

For series 1 and 2, the samples were tested uniaxially on an MTS Systems Corporation repetitive-loading system at a loading frequency of 0.5 cycle/s; a haversine load curve that lasted 0.3 s was used (16). For series 3 and 4, a pneumatic repetitive-loading system applying uniaxial loading was used at a frequency of 0.5 cycle/s with a continuous haversine load curve.

During the repetitive testing of series 3 and 4 samples, top and bottom loading caps made of Plexiglas and equipped with open psychrometers were used (Figure 1) to monitor the total soil suction before, during, and after the repetitive-loading tests. Load-deformation curves on an X-Y recorder were taken several times during the test and more fre-

quently within the first 1000 cycles. Resilient and residual deformations were monitored by a 6.25-mm travel linear variable differential transformer (LVDT) and a dial gage reading 2.5×10^{-3} mm per division, respectively. Axial load was measured by a load cell as illustrated in Figure 1. Minimum and maximum deviator stresses during the tests were kept fairly constant around 20 kPa and 100 kPa, respectively, to eliminate the deviator stress as a variable. Moisture loss in samples during repetitive loading was prevented by surrounding the membrane-covered samples by a cylinder containing wetted Styrofoam packing material, which was found to be very effective. Maximum number of load repetitions in series 1 and 2 was 10 000 and 5000, respectively. In series 3 and 4, tests were terminated after approximately 40 000 repetitions. An unconfined-compression test was run on each sample after repetitive testing.

Figure 1. Arrangement of psychrometers and load cell during repetitive-loading test.

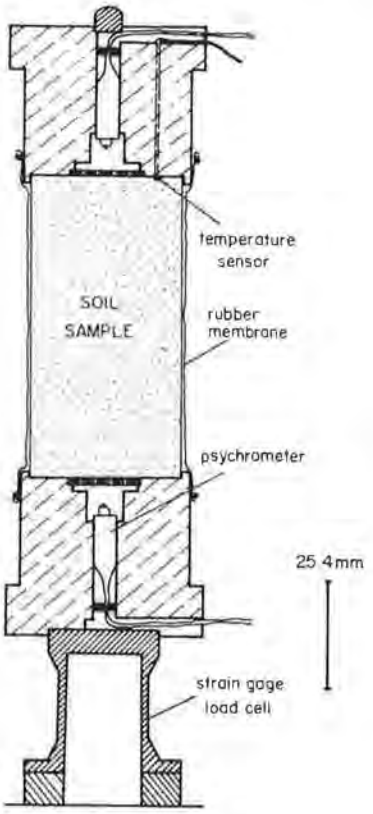

EVALUATION OF EXPERIMENTAL DATA

Resilient modulus (M_r, cyclic deviator stress divided by resilient strain), axial residual strain (ε_p), strain-energy absorption capacity, and postrepetitive testing unconfined strength (q_{up}) have been examined in this section as a function of number of load repetitions (N) and pre-test-induced matrix suction (ψ_m). Justification for the choice of matrix suction instead of total suction (ψ_t) will be given later in this section.

Load-Deformation Curves

During the repetitive-loading tests, basically three types of load-deformation curves were obtained as illustrated in Figure 2, where the repetitive stress level is indicated as a percentage of the unconfined strength. Curve 1 represents a tendency for recovery in the soil after a relatively large deformation has been imposed on it, which results in a rapid buildup of residual deformations. Repetitive-load level is relatively close to the unconfined strength, and the frequency of loading can play a significant role in controlling the residual deformations. With increasing suction, linear and concave upward loading curves result (curves 2 and 3). The lateral inertia of the sample is not expected to play a significant role in curve 3, since the loading cannot be classified as impact type. However, the initiation of a desaturation after 800 kPa as measured on series 3 and 4 specimens is believed to leave some relatively large pores free of water and easier to deform, but elastically, because of the increasing integrity of the soil structure under increasing suction. Also, the formation of microcracks with decreasing water in grundite, as observed by Luh (15) at macroscale in kaolinite samples after 800-kPa suction, and the closure of such cracks at small compressive stresses compared with the unconfined compressive strength can result

Figure 2. Relative magnitude of repetitive stress level and form of repetitive-load axial-deformation curves at different suction values.

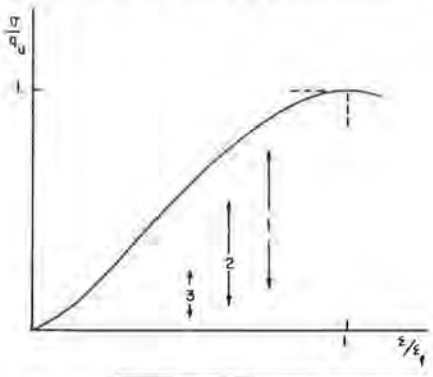

	Matrix Suction Range ($kPa \times 10^2$)		
Series I, II	$\psi_m \leq 1$	$1 < \psi_m \leq 2$	$\psi_m > 2$
Series III, IV	$\psi_m \leq 4$	$4 < \psi_m < 15$	$\psi_m \geq 15$
Curve type	(1)	(2)	(3)

Figure 3. Rate of increase in resilient modulus during repetitive loading at different matrix suction values.

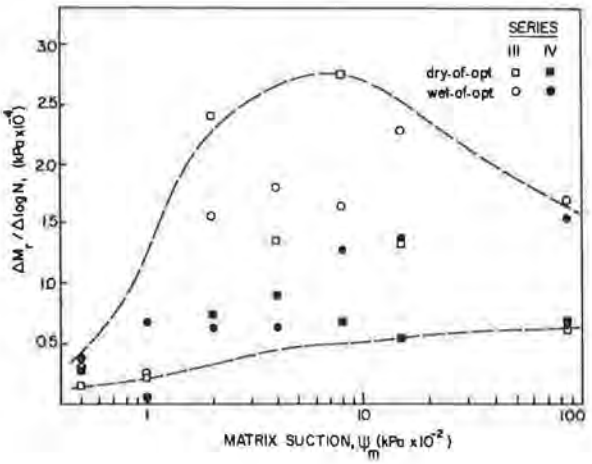

in a concave upward stress-strain curve. However, these cracks, if they actually exist, have to be very small, since thin sections prepared by using compacted grundite specimens freeze-dried under vacuum after equilibrium under 1500-kPa extractor pressure did not reveal any visible crack pattern when viewed under a petrographic microscope.

Resilient Modulus Versus Number of Load Repetitions

The resilient modulus in series 1 and 2 increased monotonically from the beginning of the repetitive-loading test (16). However, in the majority of the samples in series 3 and 4, a decrease in M_r was evident during the early part of the repetitive loading; M_r reached a minimum value mostly within the first 100 repetitions and was accompanied by an increase thereafter. This is attributed to a small time-dependent increase in the rigidity of the soil structure during the moisture-extraction process, which extended over a period of 4-12 months. After several applications of the repetitive load, the memory effects were removed. The considerable scatter in the rate of increase in M_r (Figure 3) as determined beyond 1000 repetitions by the slope of the curves of M_r versus log N shows that apparently identical compacted soil samples may display significantly different resilient moduli at large numbers of load repetitions even though the resilient response may be comparable at low repetitions during a repetitive-load test.

Resilient Modulus Versus Matrix Suction

Samples of series 1 and 2 were tested at different matrix suction values by repetitive loading without any total-suction measurements. In series 3 and 4, the measured total-suction curve showed a decreasing osmotic suction component within the range of test moisture contents when superimposed on the curve of moisture content versus matrix suction and eventually approached it at higher induced matrix suction values. The osmotic suction measured on the pore-water extracts obtained during pressure equilibrium, on the other hand, remained fairly constant with increasing extractor pressure. In general, the contribution of the soluble salts in pore water to the changes in soil behavior did not seem to be clearly reflected by the magnitude of the measured osmotic suction due to the apparently more complicated effects of the ionic distribution around the particles than can be deduced by osmotic suction measurements alone. If we consider the obvious changes taking place in soil behavior after moisture equilibration under increasing extractor pressure, the matrix suction was adopted as the meaningful soil-moisture stress parameter for the purpose of this study.

The differences in the resilient modulus of dry- and wet-of-optimum specimens at 5000 repetitions in all four series were relatively small below 100 kPa (Figures 4 and 5). Afterwards, an increasing range of M_r in series 1 and 2 was observed, more significantly in series 2, whereas it remained comparatively small in series 3 and 4 throughout the suction range used (Figure 5). The same range of compaction moisture content ($w_{opt} \pm 2$ percent) was used in all series. The difference in resilient modulus between dry- and wet-of-optimum specimens and the average value of the resilient modulus increase with decreasing plasticity (or optimum moisture content of the soil) is shown in Figure 6.

The maximum resilient modulus in all series was found to lie at a matrix suction value of approximately 800 kPa; there is a drop at 1500 kPa. The indication is that M_r increases again at matrix suction values beyond 1500 kPa as shown in the table below, which gives a set of samples tested after air drying that gave significantly higher resilient moduli:

Specimen	M_r (kPa·10^{-3})	w (%)
Series 3, wet of optimum	236.9	2.9
Series 3, wet of optimum	197.6	2.2
Series 4, dry of optimum	152.2	2.5

Therefore, all the evidence suggests the form of M_r versus log ψ_m relationship as given qualitatively in Figure 7.

High resilient modulus is rather expected at very high suction values and increasing rigidity of the soil skeleton. The hump occurring at 800 kPa represents a change more likely in the role of soil moisture than in the mechanical behavior of the soil. Increasing the dry unit weight with suction should also be considered as a contributing factor, although it does not explain the decrease in M_r after 800 kPa. Buildup of residual deformation is very small above 400 kPa, which is indicative of the more-elastic character of soil deformations under repetitive loading (see Figure 12).

A desaturation initiated at 800 kPa (Figure 8) is thought to have resulted from emptying of relatively large pores as mentioned earlier. This confines the soil moisture to extremely small pores, particle surfaces, and interparticle contacts under very high tension and possibly results in microcrack formation. This distribution of moisture is believed to give the soil structure a more elastically deformable character while the development of residual strains is resisted. The eventual development of particle-to-particle bonds beyond a certain suction level, then, results in a stiff soil structure that displays high resilient modulus as observed in oven-dried tested samples at very high suction values.

The advantage of relating the resilient modulus of soil suction instead of moisture content is evident in Figure 9 due to the fact that the matrix suction fixes the position of the maximum resilient modulus at 800 kPa for all soils tested, whereas no such trend is evident when moisture content is used as the main moisture variable. Furthermore, the use of moisture content results in considerable scatter of the data.

Because of the small differences in moisture content along the desorption and sorption branches of the moisture-retention curve, the samples tested at 400 and 100 kPa suction on the sorption curve did not provide significant insight into the effects of moisture hysteresis on the resilient behavior of the samples in series 3 and 4 and were not included in Figure 5. Series 1 and 2 samples were equilibrated only along a desorption curve.

Effects of Dry Unit Weight and Deviator Stress Level on Resilient Modulus

The samples compacted on the same side of the optimum moisture content and tested at matrix suction values up to 800 kPa indicate approximately a linear variation between M_r and γ_d within the suction range used; samples compacted dry of optimum exhibit a somewhat higher resilient modulus (Figure 10). However, this situation is believed to be due as much to generally higher soil suction in dry of optimum at a given unit weight as to the differences in the soil structure. Also, any possible relation between M_r and γ_d breaks down after 800 kPa due to the change in soil behavior.

After the termination of the repetitive loading, axial deformation-load curves were taken at increas-

Figure 4. Resilient modulus versus matrix suction in series 1 and 2 samples.

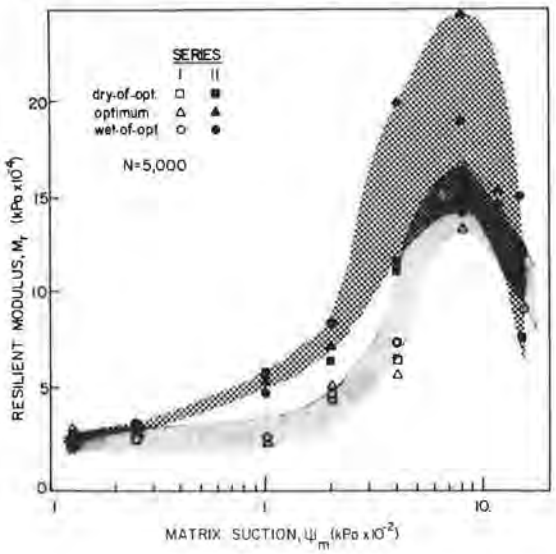

Figure 5. Resilient modulus versus matrix suction in series 3 and 4 samples.

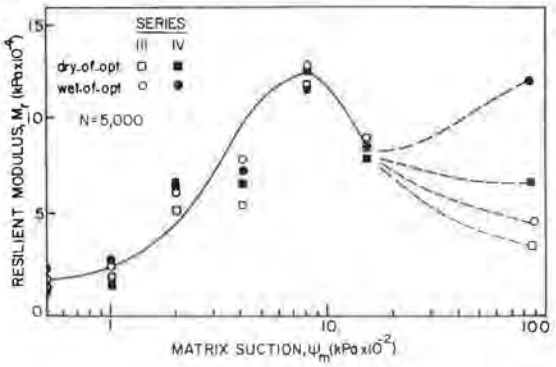

Figure 6. Range of resilient modulus values as function of plasticity index of soil.

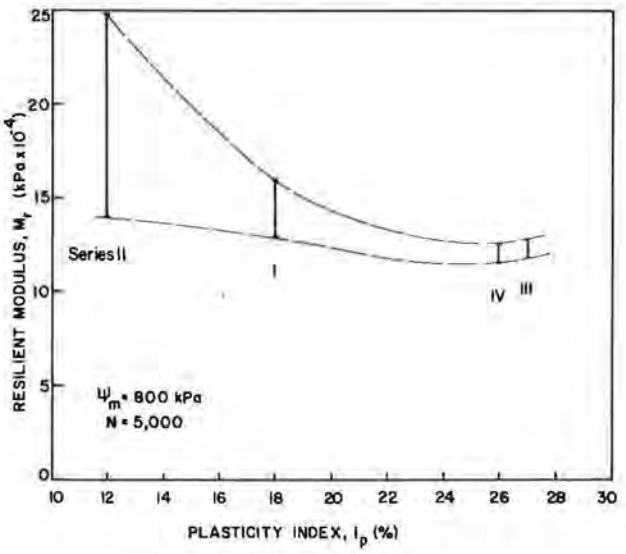

ing deviatoric stress levels above the maximum repetitive deviatoric stress. At suction values less than 1500 kPa, M_r decreased with increasing deviator stress. However, in some of the 1500-kPa specimens, M_r increased initially, reached a maximum, and decreased thereafter. This leads to the argument that the maximum M_r measured at 800 kPa may occur at a higher suction or it may disappear completely with increasing repetitive deviatoric stress levels.

Relative Energy Absorption Capacity Versus Matrix Suction

The ratio of the area inside the hysteretic load-deformation curve (A_1) to the area of the triangle (A_2) in Figure 11 is defined as the relative energy absorption capacity of the soil. It decreases rapidly with increasing suction up to 400 kPa in series 3 and 4; the minimum is in the vicinity of 800-1500 kPa. Desiccator-equilibrated samples had an absorption capacity somewhat higher than the minimum for both soils, which signified a delayed elastic response of the soil within a suction zone beyond 1500 kPa and attainment of a nearly perfect elastic response afterwards.

Estimation of this ratio at different stress levels and suction values for a soil profile underlying a structure subject to vibratory loading may help in assessing the degree of damping offered by the soil against vibration effects. A similar, suction-dependent relationship expressed in terms of shear stresses will be useful in computing the soil

Figure 7. Qualitative relationship of resilient modulus versus matrix suction including extremely high matrix suction range.

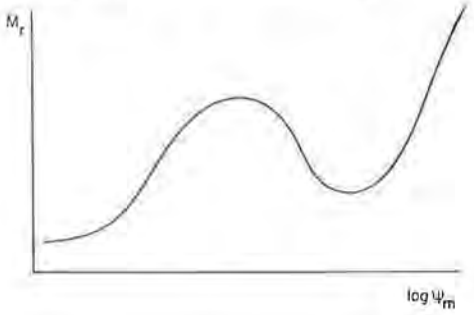

Figure 8. Degree of saturation in series 3 and 4 samples as function of matrix suction.

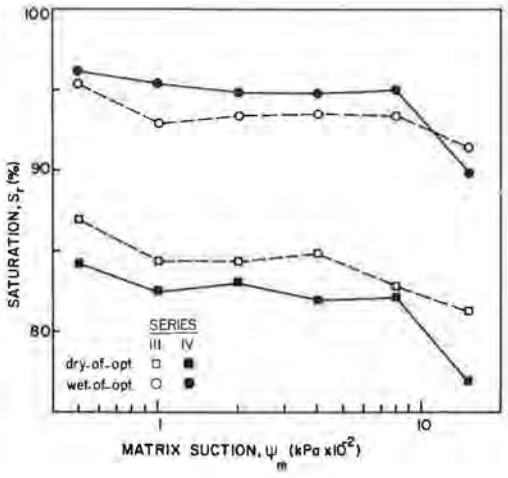

response to earthquake excitation whether there is an already established steady state or a transient suction profile.

Residual Deformation Versus Matrix Suction

Total residual strain decreased sharply in series 1 and 2 up to 100-kPa suction; it remained approximately constant afterwards (Figure 12). The same trend was observed in series 3 and 4, and the residual strain evened out after 200-kPa suction (Figure 13). There was not a clearly defined indication as to which side of the optimum compaction yielded higher residual deformation.

The increase in residual strain with the number

Figure 12. Total residual strain versus matrix suction in series 1 and 2 samples at 5000 load repetitions.

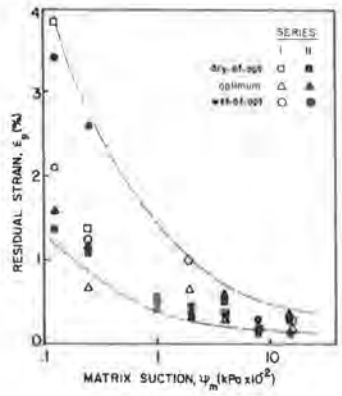

Figure 9. Resilient modulus versus moisture content in series 3 and 4 samples.

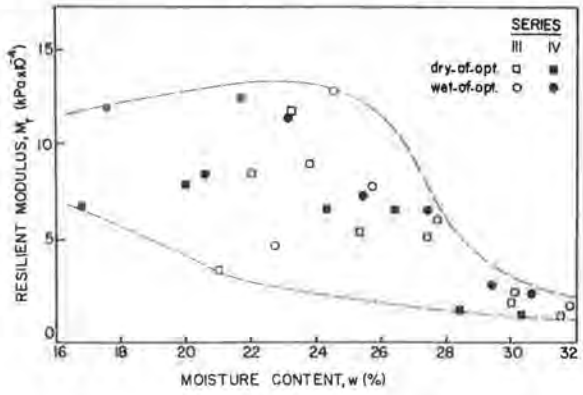

Figure 10. Resilient modulus versus dry unit weight in series 3 and 4 samples.

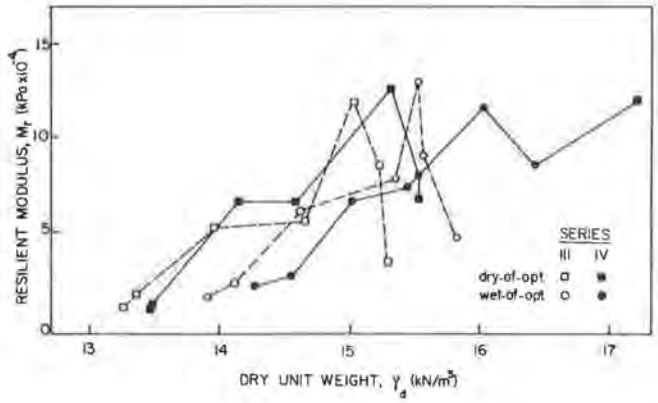

Figure 11. Relative energy absorption capacity versus matrix suction in series 3 and 4 samples.

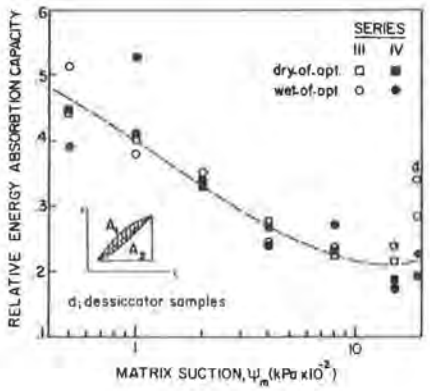

Figure 13. Residual strain versus matrix suction in series 3 and 4 samples beyond 100 load repetitions.

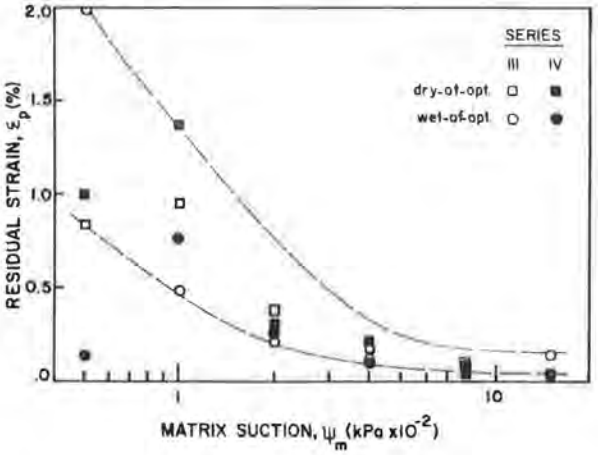

Figure 14. Rate of increase in residual strain with number of load repetitions versus matrix suction in series 3 and 4 samples.

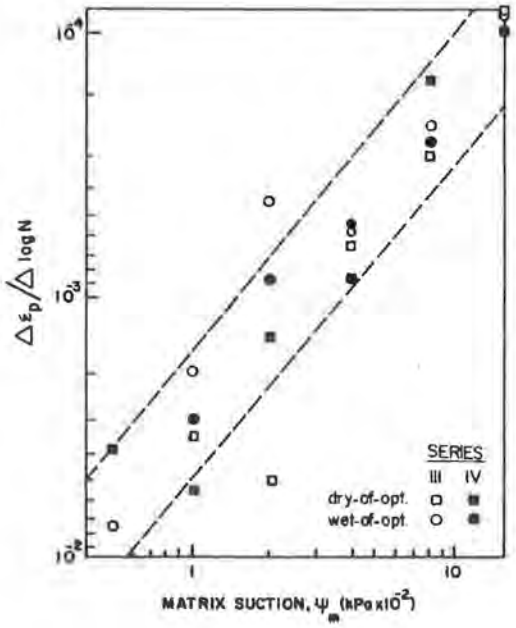

Figure 15. Postrepetitive loading unconfined compressive strength versus matrix suction in series 1 and 2 samples.

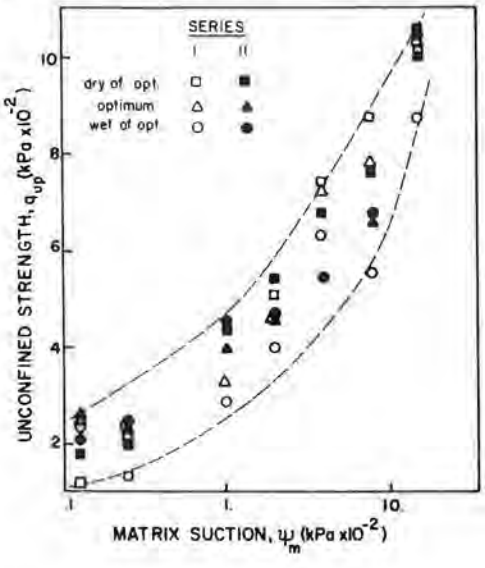

Figure 16. Postrepetitive loading unconfined compressive strength versus matrix suction in series 3 and 4 samples.

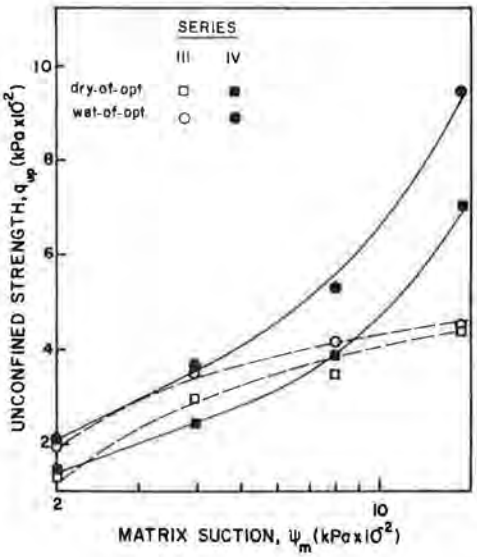

of load repetitions ($\Delta\epsilon_p/\Delta$ logN) on a logarithmic plot against the soil suction is approximately a straight line, although some scatter at suction values less than 400 kPa is evident (Figure 14). In other words, the rate of increase of residual strain is a transcendental function of suction. This suggests that the following relationship may be helpful in evaluating the buildup of residual strain with an increasing number of load repetitions:

$$\log(d\epsilon_p/d\log N) = a + b\log\psi \quad (1)$$

If we integrate Equation 1, the residual strain is obtained as follows:

$$\epsilon_p = ab\int_{\psi_i}^{\psi_f}\int_{N_i}^{N_f}(\psi^{b-1}/N)\,dN\,d\psi + C \quad (2)$$

Figure 17. Postrepetitive loading unconfined compressive strength versus test moisture content in series 3 and 4 samples.

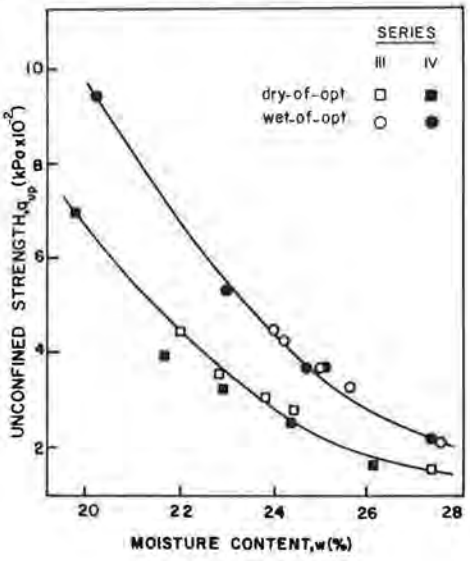

where

a and b = empirical coefficients,
ψ_i and ψ_f = initial and final matrix suction values,
N_i and N_f = initial and final numbers of load repetitions, and
C = value of ϵ_p at ψ_i and N_i.

However, considering the complexity of the field conditions, in the absence of supporting data, Equation 2 should be regarded only as a first approximation to the actual residual settlement.

Postrepetitive Loading Unconfined Compressive Strength

Unconfined compressive strength increases with increasing matrix suction in series 1 and 2; dry-of-optimum samples generally yield higher strength (Figure 15). Variation of the unconfined compressive strength in series 3 and 4 with matrix suction is given in Figure 16. The wet-of-optimum specimens yield higher strength throughout the moisture-content range; the difference between series 3 and series 4 specimens increases with increasing matrix suction. However, as is evident from the comparison of Figures 16 and 17, unconfined compressive strength correlates better with moisture content than with matrix suction. Since the data presented in Figures 15 and 16 do not indicate the type of decrease observed in the resilient modulus beyond a suction value of 800 kPa, no interdependence between the unconfined compressive strength and the resilient modulus of the soil exists after 800 kPa. Therefore, the static unconfined compression test results should not be taken as indicative of the resilient modulus of the soil at high suction and at relatively low repetitive-stress levels.

SUMMARY AND CONCLUSIONS

The changes in the deformation characteristics of a number of cohesive soils as a function of the initial matrix suction have been investigated for repetitive unconfined loading. The following conclusions are drawn from an evaluation of the data:

1. The rate of change in the resilient modulus with the number of load repetitions in samples tested at the same initial matrix suction can be significantly different even for soils with similar grain size, plasticity, and compaction characteristics.

2. The resilient modulus displayed a maximum at a matrix suction of about 800 kPa followed by a drop and a subsequent increase for the soils tested at the repetitive deviator-stress level used. However, it is possible that both the magnitude of the maximum modulus and the corresponding critical matrix suction change at a different stress level.

3. The similarity of the curves of resilient modulus versus matrix suction obtained on different soils supports the use of matrix suction as the basic soil-moisture parameter rather than the moisture content for indexing the deformation behavior of cohesive soils.

4. The scatter in the curves of resilient modulus versus matrix suction can be minimized by normalizing the resilient modulus with respect to a parameter related to the plasticity index of the soil. Another parameter, which involves the difference between the dry- and wet-of-optimum compaction moisture contents compared with the optimum compaction moisture content, can possibly be used for this purpose.

5. The effects of dry unit weight on the resilient behavior of soil with increasing matrix suction can meaningfully be investigated for compaction only on one side of the optimum moisture content, either dry or wet, because of the fabric effects.

6. Unconfined compressive strength does not prove to be a good indicator of the resilient behavior of cohesive soils tested at matrix suction values above 800 kPa, since it continues to increase while the resilient modulus decreases. Strength appears to be correlated with moisture content better than soil suction, whereas the opposite is true for the resilient modulus.

REFERENCES

1. G.B. Aitchison. The Strength of Quasi-Saturated and Unsaturated Soils in Relation to the Pressure Deficiency in the Pore Water. Proc., Fourth International Conference on Soil Mechanics and Foundation Engineering, London, 1957, pp. 135-139.
2. G.B. Blight. Strength Characteristics of Desiccated Clays. Journal of the Soil Mechanics and Foundation Engineering Division of ASCE, Vol. SM 6, 1966, pp. 19-37.
3. C.R. Camp and W.R. Gill. The Effects of Drying on Soil Strength Parameters. Proc., Soil Science Society of America, Vol. 33, No. 5, 1969, pp. 641-644.
4. T.B. Edil and R.J. Krizek. Influence of Fabric and Suction on the Mechanical Behavior of a Kaolinitic Clay. Geoderma, Vol. 15, 1976, pp. 323-341.
5. K. Majidzadeh, H.R. Guirguis, and G.S. Joseph. Fundamentals of Soil Compaction. Ohio State Univ. Transportation Research Center, Columbus, Final Rept. EES248, 1971.
6. J. Williams and C.F. Shaykewich. The Influence of Soil Water Matrix Potential on the Strength Properties of Unsaturated Soil. Proc., Soil Science Society of America, Vol. 34, No. 6, 1970, pp. 835-840.
7. R.N. Yong, R.D. Japp, and G. How. Shear Strength of Partially Saturated Clays. Proc., Fourth Annual Regional Conference on Soil Mechanics and Foundation Engineering, Bangkok, Thailand, 1971, pp. 183-187.
8. E.K. Sauer and C.L. Monismith. Influence of Soil Suction on Behavior of Glacial Till Subjected to Repeated Loading. HRB, Highway Research Record 215, 1968, pp. 18-23.
9. B.G. Richards, H.W. Murphy, C.Y.L. Chan, and R. Gordon. Preliminary Observation of Soil Moisture and Dry Compaction in Pavement Design on the Darling Downs, Queensland. Proc., Fifth Conference of Australian Road Research Board, 1970, pp. 116-142.
10. B.C. Richards and R. Gordon. Prediction and Observation of the Performance of a Flexible Pavement on an Expansive Clay Subgrade. Third International Conference on the Structural Design of Asphalt Pavements, London, England, 1972, pp. 133-143.
11. B. Shackel. Changes in Soil Suction in a Sand-Clay Subjected to Repeated Triaxial Loading. HRB, Highway Research Record 429, 1973, pp. 29-39.
12. D.G. Fredlund, A.T. Bergan, and E.K. Sauer. Deformation Characterization of Subgrade Soils for Highways and Runways in Northern Environments. Canadian Geotechnical Journal, Vol. 12, No. 2, 1975, pp. 213-223.
13. D.G. Fredlund, A.T. Bergan, and P.K. Wong. Relation Between Resilient Modulus and Stress Conditions for Cohesive Subgrade Soils. TRB, Transportation Research Record 642, 1977, pp. 73-81.
14. E.V. Edris and R.L. Lytton. Climatic Material Characterization of Fine-Grained Soils. TRB, Transportation Research Record 642, 1977, pp. 39-44.
15. G.-F. Luh. An Experimental Study of the Dynamic Behavior of Soils. Univ. of Wisconsin-Madison, Ph.D. thesis, 1980.
16. T.B. Edil and E.S. Motan. Soil-Water Potential and Resilient Behavior of Subgrade Soils. TRB, Transportation Research Record 705, 1979, pp. 54-63.
17. B. Shackel. The Compaction of Uniform Replicate Soil Specimens. Journal of Australian Road Research Board, Vol. 4, No. 5, 1970, pp. 12-31.

Publication of this paper sponsored by Committee on Mechanics of Earth Masses and Layered Systems.

Solar Radiation Effects on Frost Action in Soils

CHESTER W. JONES

Engineers should be aware of solar radiation effects of frost action in soil foundations on the performance of surface structures. Damage to concrete canal drop structures and lining from frost heave on shaded sides in contrast to sun-exposed sides is described. To demonstrate passive solar effects on frost penetration, winter temperatures were measured on the concrete surfaces and in the soil subgrade beneath black-painted and unpainted concrete linings on shaded and sun-exposed sides of a small canal. Periodically, data on air temperatures, snow cover, and cloudiness were collected and incident radiation and radiation reflected from the different concrete surfaces were measured. Frost penetrated 37 percent less on the painted, sun-exposed side than on the unpainted, sun-exposed side. Because of longwave, nighttime radiation, frost penetrated 28 percent more on the painted shaded side than on the unpainted shaded side. For the unpainted concrete, frost penetrated 9-13 percent less on sun-exposed than on shaded sides.

In the current emphasis to develop solar energy for many purposes, the possibility of its use to reduce frost action in soil foundations and consequent damage to overlying structures should not be overlooked. For frost-susceptible soils in cold climates, the effects of passive solar energy are often apparent; it is common knowledge that frost heave is often greater in shaded than in sun-exposed areas, other surface and climatic conditions being equal. For example, this has been observed along highways shaded by trees, bluffs, buildings, or overpasses where frost penetration has been deeper than in unshaded areas. Although there are many factors that affect frost heave, a general correlation has been established between shadow zones beneath east-west oriented overpasses and the magnitude of frost heave; in extreme cases, differential pavement movement has presented a hazard to fast-moving traffic (1).

Differences in performance due to solar influences have also been apparent on concrete lining and other structures of irrigation canals. This paper will first mention three instances in which damage to concrete canal structures has been greater on shaded than on sun-exposed sides in areas where frost heave has been unusually high. The main part of the paper will describe a small field experiment where frost penetration was measured in the soil foundation beneath black-painted and unpainted concrete lining on shaded and unshaded canal side slopes (2). The experiment was conducted adjacent to a site where previous research on polystyrene insulation for lining had been completed and a major part of the temperature-measuring instrumentation was already in place. With a small amount of additional work, the test site provided an opportunity to demonstrate solar effects in soil under different surface and shading conditions, even though in this instance no damage occurred and painting of canal linings as a general practice to control frost heave would not be practicable. However, the attention of engineers should be directed to potential problems and beneficial effects from solar action on soil foundations of structures. Besides the avoidance of problems, there are opportunities to devise new ways to use passive or active solar energy to control frost heave in soil foundations. Some research in this direction has been started with experiments such as those on earth heat pipes with solar augmentation to control preferential icing on highway pavements and bridges (3).

EXAMPLES OF FROST DAMAGE

Figure 1 shows a rectangular inclined canal drop of reinforced concrete affected by frost action. This canal runs east-west and the inward deflection of concrete walls has been mostly on the south side where shading occurs in winter; the lateral force of soil frost action on the wall is apparent from the bending of the 75-mm-diameter steel pipes added for support. Some of the wall backfill on the shaded side has been removed to relieve pressure, and weep holes have been drilled to lower the water table. The sun-exposed wall is relatively undamaged although the drainage from weep holes shows the presence of groundwater. The reinforced concrete floor of the chute has also been damaged from differential frost heave; greater heave occurred in the south half than in the north half.

Frost damage on the outlet of a rectangular inclined drop of reinforced concrete is shown in Figure 2. Here the top of the south wall of the east-west oriented structure has tipped inward about 200 mm. As a maintenance procedure, a concrete cap superimposed with soil has been added to prevent

Figure 1. Damage caused by frost action in soil on shaded south side of canal drop structure.

Figure 2. Wall deflected inward by frost pressures in soil.

Figure 3. Breakage during spring thawing period of concrete canal lining on south side of east-west oriented canal.

possible collapse of the wall.

Figure 3 shows frost-heave damage to a 65-mm-thick slip-formed concrete lining in a small canal. At the crack in the side slope, the upper portion of the lining is offset upward an amount about equal to the lining thickness. This canal is oriented east-west and the greatest damage by far is on the south-side slope, which is completely or partly shaded at times when the sun is low over the southern horizon in winter. The damage occurred mostly during a two-week period in March after a particularly cold winter. Apparently, during the winter, frost action in the soil subgrade heaved the concrete relatively uniformly without causing noticeable cracks. When thawing occurred in March, the soil under the north slope, exposed more or less directly to the sun, thawed faster than that on the south side and the concrete was broken by the differential settlement. Although other factors such as the insulating effects of snow may have been involved, a study of the angle of the sun on the lining in winter (Figure 4) offers a possible basis for explaining the slow uni-

Figure 4. Cross section of concrete lining and angle of sun on sun-exposed slope.

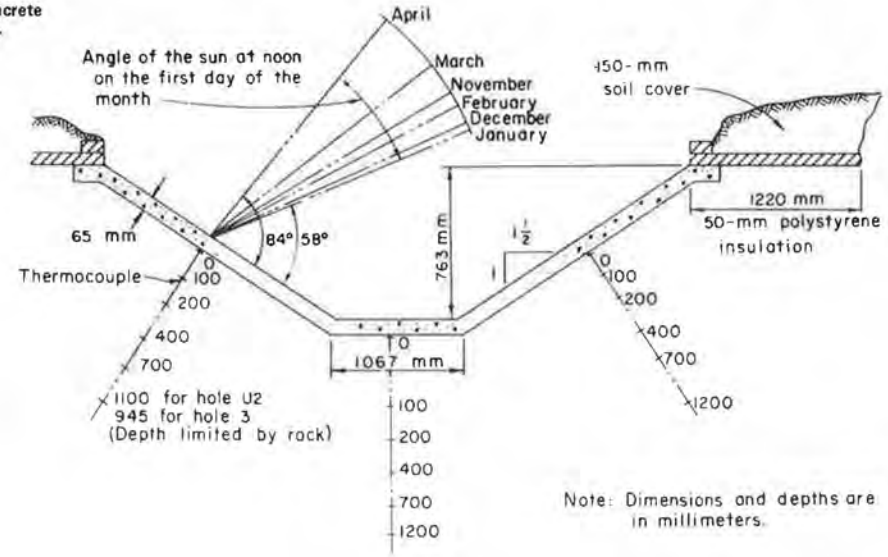

Figure 5. Plan of frost test section.

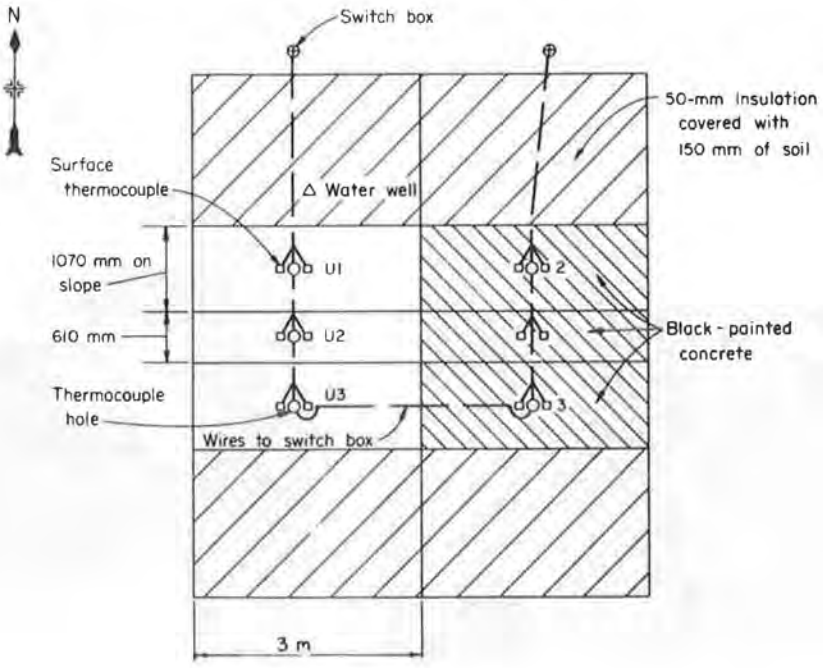

form heave and the faster differential settlement; in March the angle is greater than at any other time, since significant freezing temperatures started at the onset of winter.

Exploration at the end of March showed ice lenses still under the south slope. Subsequently, after complete thawing of the soil, the offset was reduced to about 25 mm. For north-south oriented canals, insolation is more even on both sides of the canal and damage from frost heave is usually much less.

Past damage such as that noted above has led to improved design and construction practices to avoid damage. In one special instance, a chute 1950 m long replaced a series of drop structures located down a hillside where extensive damage to the drop structures had recurred. The base of the chute was located near the ground surface, and shallow subsurface drains on each side were provided.

FROST INVESTIGATION

Test Program

This solar experiment was conducted during one winter. The purpose was to determine what effect radiation from the sun would have on frost penetration beneath a particular black-painted concrete canal lining with its soil conditions compared with penetration for an adjacent unpainted section. Incident radiation and radiation reflected from the concrete surfaces were measured. Temperatures were also measured on the concrete surfaces and at six depths in the soil beneath the lining to monitor the progress of frost. Climatic data were gathered and the groundwater level was recorded at intervals during the winter.

Test Site

The canal investigation site was located on the Riverton Unit, Pick-Sloan Missouri River Basin Program, on lateral 15.1 about 1.5 km west of the town of Pavillion, in west-central Wyoming. It was at one of two sites on the project where previous tests with polystyrene insulation had been made (4;5, p. 17).

The test section was oriented due east-west, which provided shaded south and unshaded north side slopes. The soil at the test site ranged from a silty or clayey sand to a lean clay; the liquid limit was between 26 and 36 and the plasticity index between 12 and 20. The soil dry density was 1650-1675 kg/m³ and the relative mass density, 2.67. The moisture content ranged from about 6 percent near the ground surface to 25 percent below the bottom of the canal where the groundwater table was encountered.

Test Installation

The test sections consisted of two adjacent sections of concrete lining, each about 3 m in length (Figure 5). Polystyrene insulation 50 mm in thickness with a 150-mm soil cover was placed on each side of the canal lining to prevent frost penetration from outside the lining.

After a thorough cleaning of the concrete surface, one section of lining was covered with one coat of primer and two coats of black vinyl acetate paint (Figure 6). Surface thermocouples were installed in pairs on the sides (Figure 7) and bottoms of the painted and unpainted test sections. The thermocouple tips were attached to the concrete with screws and black or clear silicone sealant.

A cross section of the lining with the location of thermocouples beneath the concrete is shown in Figure 4. Thermocouples were installed by (a) coring a 100-mm hole through the concrete; (b) augering a hole in the soil below, perpendicular to the concrete surface; (c) placing the thermocouples, which were loosely attached at the desired spacing to a lath in the hole; (d) refilling the hole around the thermocouples with a soil-water slurry; and (e) filling the concrete hole with fresh concrete. The thermocouple wires were of the polyvinyl-coated, copper-constantan type. They were connected to multiple-position switches mounted on steel posts. A thermocouple to record air temperature was located about 1 m from the ground surface in a specially constructed wooden box attached to one of the switchbox posts. When temperatures were to be measured, a digital thermometer was connected to one of the switches and the temperature at each thermocouple was read by switching from one to another.

Radiation Equipment

At the Midvale Irrigation District yard in Pavillion, a stationary radiometer was installed on top of a post. A digital readout of the total insolation for any period of time was provided by an ampere-hour meter. A separate meter on the radiometer indicated the instantaneous rate of insolation.

At the canal test site, incident radiation and radiation reflected from the concrete lining surfaces were measured by a small portable radiometer.

MEASUREMENTS AND OBSERVATIONS

About once a week and for one day each month at 2-h intervals between 6:00 a.m. and 6:00 p.m., project personnel measured (a) radiation in the general area and that reflected from the painted and unpainted concrete surfaces, (b) air temperatures, and (c) temperatures on the concrete surfaces and in the soil beneath. At the time of these measurements, clouds were described as high, medium, or low and thin or heavy; and degree of cloud cover was estimated (clear, less than 0.3; partly cloudy, 0.4-0.7; and cloudy, greater than 0.8). Wind direction and speed were estimated and records of snow and ice in the canal made. About once a month, the groundwater level in a well beside the canal was measured.

Pavillion is located at 43°50' north latitude and 108°41' west longitude at an elevation of 1660 m. A cumulative degree-days curve, based on air temperatures recorded at Pavillion, is given in Figure 8; this type of curve is useful for comparing temperatures in different locations (6). This shows that the freezing index was 706 Celsius degree-days; each degree-day is the algebraic difference between the average of maximum and minimum daily temperatures and 0°C. The freezing duration for the winter of 1977-1978 was 108 days.

Snowfall during the winter of 1977-1978 was light. The following data on snow and ice in the canal at the test site were recorded:

Date	Snow and Ice Conditions
Dec. 9	0.3 cm snow, shaded side
Jan. 4	1 cm snow, shaded side
Jan. 13	Trace of snow, shaded side
Jan. 20	8 cm snow, test area
Jan. 25	2 cm snow, ground, and 15 cm drifted in lateral bottom
Feb. 2	15 cm snow, in bottom
Feb. 13	15 cm snow, test section
Feb. 17	15 cm snow, shaded side
Feb. 24	6 cm ice, on bottom
March 1	6 cm ice, on bottom

DISCUSSION OF RESULTS

Radiation

The radiation measurements and the cloud conditions are shown in Table 1. A comparison of radiation on the black and unpainted concrete sections can be made from the albedo, which is the percentage of reflected radiation based on the incident or total incoming radiation. As expected, the black surface usually absorbed more daytime radiation than did the unpainted surface. Varying cloud conditions sometimes affected radiation readings within short time intervals.

The intensity of insolation on a plane surface depends on the angle of the sun's rays with the surface; the highest intensity is when the angle is 90°. A plot of sun angles on the sun-exposed north side of the canal lining is shown in Figure 4; these were computed from the angle of the side slope and with the latitude and the declination of the sun.

Temperature and Frost Penetration

Averages of all temperatures measured at each thermocouple beneath the concrete are plotted in Figure 9. The temperatures of both black-painted and unpainted concrete were higher on the sun-exposed side than on the shaded side by about 6°C at zero depth (bottom of the concrete) and less than 1°C at 1000 mm. Compared with the unpainted concrete, the higher average temperatures beneath black-painted concrete on the sun-exposed side and lower temperatures beneath this type of surface on the shaded side are also seen.

An example of a one-day record of concrete surface and soil subsurface temperatures is shown in Figures 10 and 11. On clear days or when clouds were not heavy, the plots of temperatures during the day show a wide variation between temperatures at

Figure 6. Black-painted concrete lining with unpainted control section in foreground.

Figure 7. Thermocouples for measurement of surface temperatures on unpainted concrete lining.

Figure 8. Cumulative degree-days curve for Pavillion, Wyoming, for winter of 1977-1978.

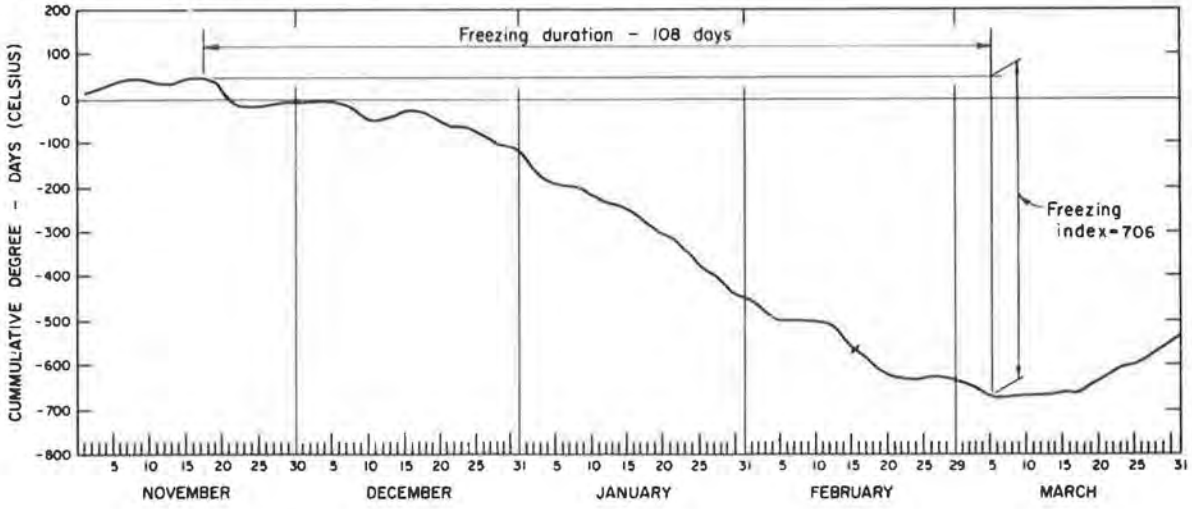

the surface and beneath the concrete on the sun-exposed side. As would be expected, this was much less on the shaded side.

A plot of maximum frost penetration is shown in Figure 12. Although the black surface generally absorbed more radiation than the unpainted concrete during the day, this was offset by the longer-wave radiation from the black surface at night. Therefore, although the black surface reduced frost penetration 37 percent on the sun-exposed side, it caused an increase in penetration of 28 percent on the shaded side.

For the unpainted section, frost penetration was 9 percent less on the sun-exposed side of the canal compared with that on the shaded side. During the preceding winter, temperatures on the same section indicated that frost penetration was about 700 mm on the sun-exposed side compared with 800 mm on the shaded side; the difference was 13 percent.

Although there were no thermocouples installed beneath the painted concrete at the bottom of the canal, those installed under the unpainted bottom showed that frost had penetrated about 340 mm; during the previous winter the penetration at this location was 400 mm. This penetration was probably influenced by the presence of the water table and, at times, by snow and ice in the lateral. The depth of the water table below the lining ranged between 140 mm on November 17, 1977, to 325 mm on March 8, 1978. Thus, the frost penetrated to approximately the water-table elevation.

Frost heave on the lining was not measured during this experiment. However, during the previous winter, adjacent lining heaved a maximum of about 20 mm

Table 1. Solar radiation at Pavillion, Wyoming, and at concrete lining test site on lateral 15.1.

		Pavillion Station Incident (W/m^2)			Test Site Reflected (W/m^2)								
					Shaded				Unshaded				
					Black		Unpainted		Black		Unpainted		
Date	Time	Instantaneous	Cumulative	Incident (W/m^2)	Reading	Albedo	Reading	Albedo	Reading	Albedo	Reading	Albedo	Sky Condition
1977													
12/13	1200	279	103 689	439	31	7	47	11	47	11	98	22	Cloudy, thin, of medium height[a]
12/13	1400	265	103 758	-	31	-	31	-	77	-	126	-	Cloudy, thin, of medium height
12/13	1600	14	103 827	31	16	51	31	100	16	51	16	51	Cloudy, thin, of medium height
12/21	1300	349	105 711	300	31	10	62	21	77	26	77	26	Cloudy, high, thin[b]
									98	28	174	50	Clear, high, thin clouds
1978													
1/4	1330	397	110 383	349	62	18	62	18	126	33	174	46	Clear, no clouds
1/13	1330	384	112 544	377	62	17	47	13	174	40	223	51	Clear, high, thin clouds
1/25	1330[c]	432	116 519	439	47	11	98	22	188	38	188	38	Clear, high, thin clouds
2/2	1330	474	121 330	502	62	12	112	22	488	97	502	100	Clear, high, thin clouds
2/13	1400	432	126 420	502	188	37	202	40	126	78	126	78	Clear, no clouds
2/17	0800	195	-	160	98	61	98	61	223	48	286	52	Clear, no clouds
2/17	1000	307	-	460	126	27	126	27	251	50	251	50	Clear, no clouds
2/17	1400	502	130 325	502	139	28	160	32	160	68	59	59	Clear, no clouds
2/17	1600	209	-	237	77	32	98	41	188	38	223	44	Cloudy, high, thin; varied cloud cover
2/24	1340	418	135 694	502	77	15	126	25	126	29	139	32	Cloudy, high, thin; varied cloud cover
3/1	1330	-	-	439	98	22	139	32	160	35	223	48	Clear, high, thin
3/8	1250	-	-	460	77	17	98	21	126	53	139	59	Clear, no clouds
3/15	0800	-	-	237	31	13	77	32	188	31	223	37	Clear, high, thin
3/15	1000	-	-	600	31	5	112	19	188	31	202	33	Cloudy, heavy, of medium height
3/15	1200	-	-	614	62	10	126	20	223	29	300	39	Cloudy, heavy, of medium height
3/15	1400	-	-	774	112	14	139	18	126	33	174	46	Clear, high, thin clouds
3/15	1600	-	-	377	49	13	98	26	62	25	98	39	Cloudy, heavy, of medium height
3/22	1300	-	-	251	49	19	77	31					

[a]Sun out more when instantaneous reading was taken. [b]Sun covered with clouds part of time. [c]Fresh snow; some ice on radiometer.

and settled back to 4 mm above the prewinter level without causing any noticeable cracking (5).

For any permanent installation of this sort to benefit from solar heat absorption, the surface would need to retain its capacity for absorption. A dark-surface concrete canal lining, whether painted or with pigment incorporated in the concrete, would no doubt lose much of its color and effectiveness for this purpose because of weathering action and the sediment and other material that normally collects in a canal. Furthermore, any scheme for adapting active or passive solar systems to canals would need to be reliable when unattended in relatively remote areas and require a minimum of maintenance.

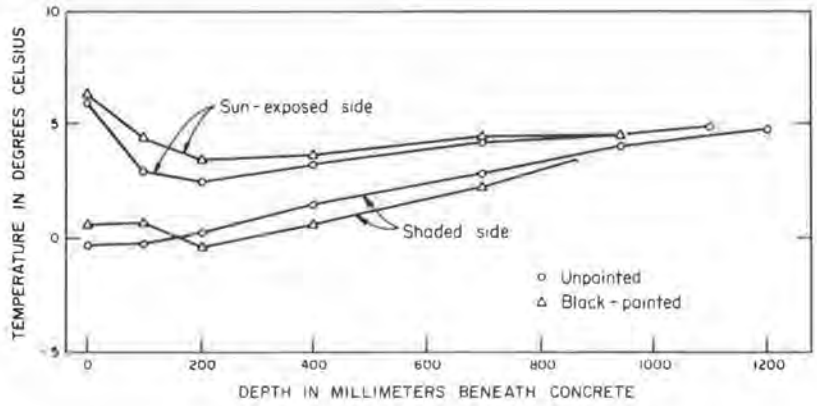

Figure 9. Averages of temperatures measured below concrete canal lining during winter of 1977-1978.

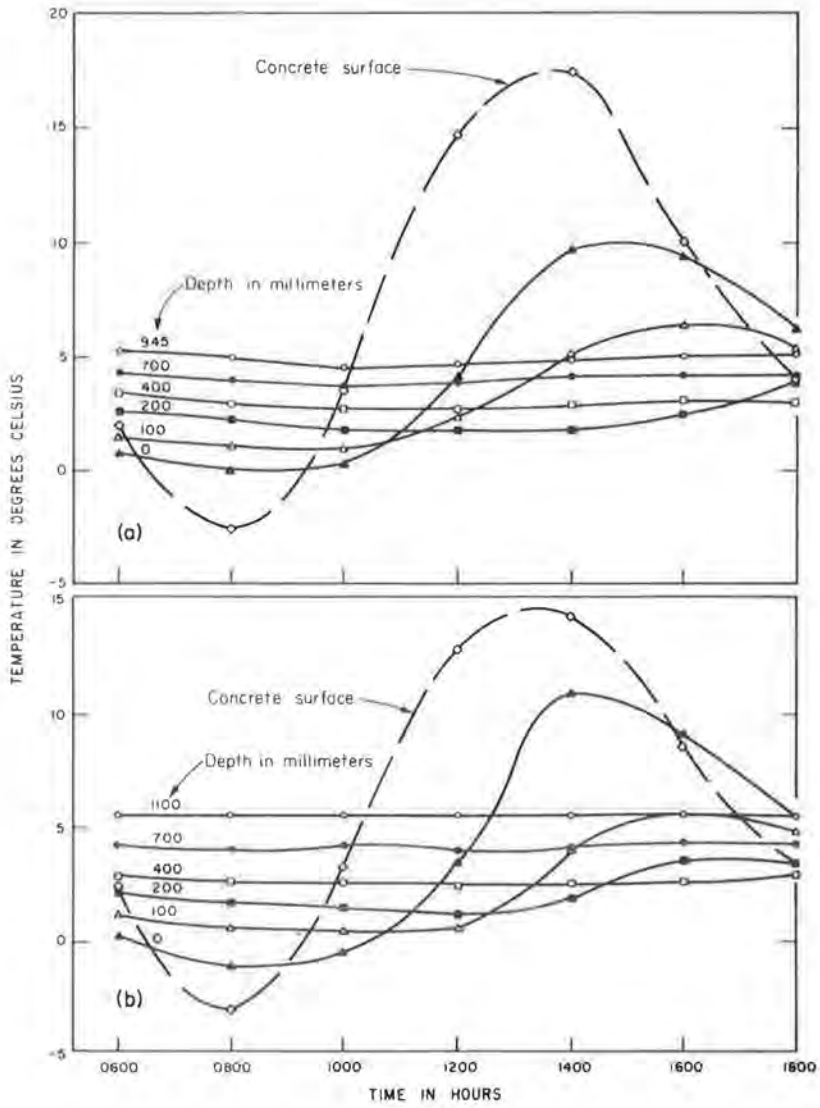

Figure 10. Temperatures on surfaces and in soil beneath (a) painted and (b) unpainted concrete canal lining, December 13, 1977.

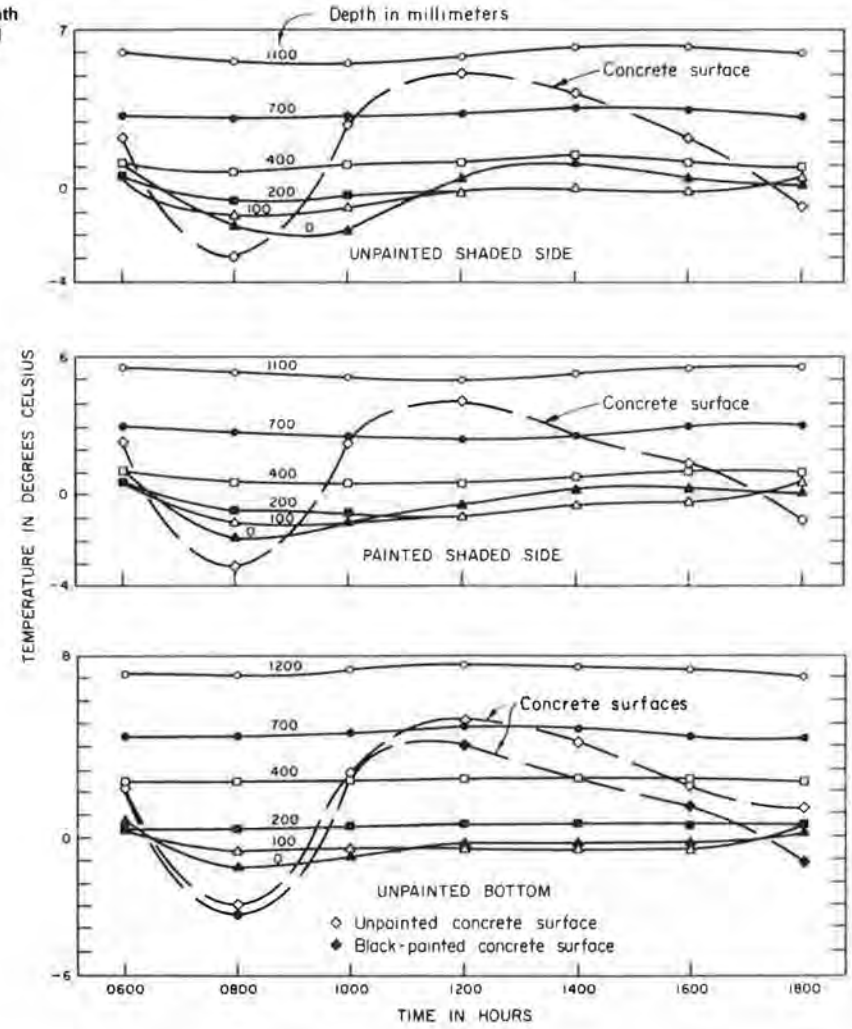

Figure 11. Temperatures on surfaces and in soil beneath painted and unpainted concrete canal lining on shaded sides and on unpainted bottom, December 13, 1977.

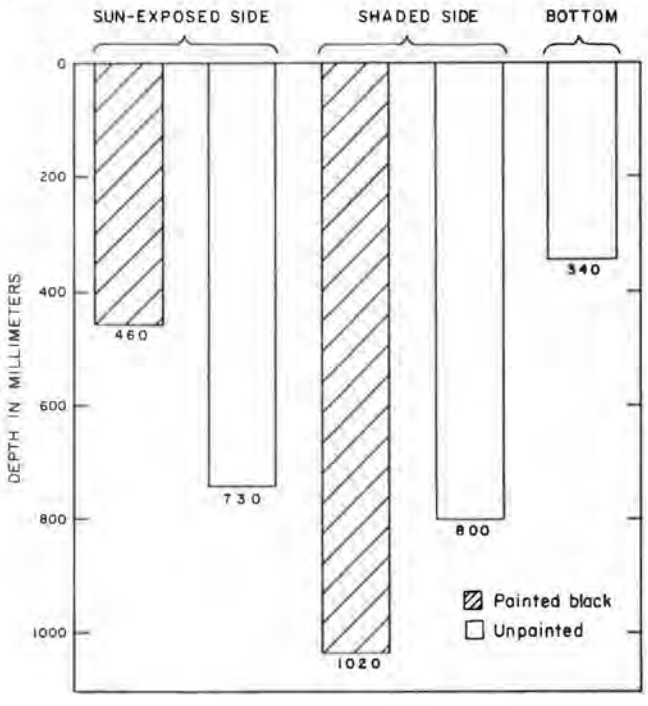

Figure 12. Maximum frost penetration beneath concrete canal lining.

SUMMARY AND CONCLUSIONS

Frost-heave damage to concrete canal structures can be significantly greater on shaded than on unshaded sides due to differences in solar effects on frost action in the soil foundation.

A field experiment was conducted during one winter to determine depth of frost penetration beneath black-painted and unpainted concrete canal lining on the north and south side slopes of an east-west oriented canal. The experiment showed that on the north sun-exposed slope, maximum frost penetration was 37 percent less beneath black-painted than unpainted concrete. On the shaded to partly shaded south side slope, frost penetration was 28 percent deeper beneath the black-painted concrete than for the unpainted concrete, which shows the effect of the long-wave, nighttime radiation. For the unpainted concrete during two successive winters, frost penetration was 13 and 9 percent less on the sun-exposed side than on the shaded side.

REFERENCES

1. Interstate Overpass Frost Heave Study. Maine State Highway Commission, Augusta, Materials and Research Tech. Paper 67-10R, Sept. 1967.
2. C.W. Jones. Frost Penetration Beneath Black-Painted Concrete Canal Lining. Bureau of Reclamation, Denver, CO, Rept. REC-ERC-79-5, April 1979.

3. M.F. Pravda, W.B. Bienert, D.A. Wolf, J.E. Nydahl, K.M. Pell, and S.R. Ownbey. Executive Summary for Augmentation of Earth Heating for Purposes of Roadway Deicing. FHWA, Rept. DTM-78-6, Dec. 1978.
4. C.W. Jones. Frost Heave and Polystyrene Insulation at a Canal Drop Structure. Bureau of Reclamation, Denver, CO, Rept. REC-ERC-78-3, Feb. 1978.
5. C.W. Jones and B.M. Laymon. Polystyrene Insulation for Concrete Canal Lining. Bureau of Reclamation, Denver, CO, Rept. REC-ERC-78-10, Nov. 1978.
6. T.C. Johnson, R.L. Berg, K.L. Carey, and C.W. Kaplar. Roadway Design in Seasonal Frost Areas. Corps of Engineers' Cold Regions Research and Engineering Laboratory, Hanover, NH, Tech. Rept. 259, March 1975, pp. 15-17.

Publication of this paper sponsored by Committee on Frost Action.

Factors Affecting Coating of Aggregates with Portland Cement

O.E.K. DAOUD, H.R. GUIRGUIS, AND S.K. HAMDANI

The Kuwaiti experience in applying the technique of cement coating the smoothly textured aggregates in the production of high-quality asphaltic mixtures has been that the success of the resulting cement treatment was not always certain. It was influenced rather by a number of material and processing variables. The effect of four such variables is investigated by preparing a number of cement-coated sand samples at different levels of treatment and under controlled laboratory conditions. Cement coats produced in these samples were then evaluated by analyzing and comparing the results from a close visual examination, a particle-size analysis, a specific-surface analysis, and a chemical analysis for cement content of the various fractions. The study indicated two extreme and identifiable states of coating within which successful treatments were attainable. At the lower levels of water and cement contents, the added cement failed to adhere permanently to the surface of particles, resulting in a poorly coated sand of a higher fines content. At the higher levels of water and cement, the finer fractions of the sand started forming weakly cemented lumps, thus effecting a coarser gradation that lacked the finer sizes. By applying certain limits on the amount of added cement to avoid arriving at these objectionable extremes, a practical relationship was developed expressing the amount of cement required for proper coating in terms of the specific surface of the sand intended for treatment.

Surface texture of aggregates is an important property influencing the behavior of asphalt pavements. It can be said in general that asphaltic mixtures made with rough-textured aggregates have better resistance to stripping (1), higher Marshall and Hveem stability values at optimum asphalt (2), and longer fatigue lives in stress-controlled tests (3,4).

In Kuwait, the technique of coating aggregates with portland cement to enhance surface texture is widely used at the present time in the production of high-quality asphaltic mixtures (5). Under the severe weather conditions of the region, these mixtures are believed to be superior in resisting such common types of failure as surface corrugations (developed particularly at traffic intersections), fatting up or bleeding, and premature distortion in the wheel tracks of heavy and channelized traffic. Experience in applying the cement-coating technique has indicated that the quality and effectiveness of the resulting treatment are not always satisfactory and depend on a number of material and processing variables. Among such variables are the type of aggregate, the amount of added cement, the quantity of water, the time of mixing, and the type of mixer used in the process.

Experience has also showed that the effect of the above variables in coating fine aggregates is much greater than in coating coarse aggregates, where good results were readily obtainable. The large mass of individual particles in this case and consequently the higher-impact forces they produce in the mixer during the process of coating leave only a secondary role for the smaller forces due to surface tension, water viscosity, cohesion, etc., to play in distributing the added cement. With sand-size aggregates this latter role becomes more important and perhaps dominant. A knowledge of the levels at which the variables in the coating process would produce optimum results becomes highly necessary, since an arbitrary selection of these levels may produce inferior results.

A particular difficulty often encountered in the cement coating of sand is a significant and uncontrollable change in its gradation after treatment. Either an abundance of fines or severe deficiency may result, depending on the values selected for various parameters. In addition to reducing the effectiveness of the added cement, such extreme conditions often necessitate subsequent corrective measures to satisfy job-mix requirements for gradation.

The purpose of this paper is to investigate the effect of four factors on the quality of the cement coat obtained in the treatment of sand: the gradation of the sand, its initial surface characteristics, the amount of added cement, and the quantity of added water.

Guirguis, Daoud, and Hamdani (6) have dealt with the effect of coating the aggregates with cement on laboratory performance of asphaltic mixes.

METHODOLOGY

The approach adopted here was to prepare samples of cement-coated sand by several treatments and under controlled laboratory conditions. Each treatment represented a particular combination of the four variables adopted in the study. The cured samples were then analyzed by four methods, including granulometric and gravimetric measurements. Results from these analyses were compared and discussed, and the quality of the different cement treatments was appraised accordingly.

Figure 1. Program for coating sand with portland cement.

SAND TYPE	GRADATION	WATER/CEMENT	6	7	8	9	10	11	12	13	14	15
NATURAL	G1	0.35	X		X		X		X		X	
		0.45	X		X		X		X		X	
CRUSHED	G2	0.35		X		X		X		X		X
		0.45		X		X		X		X		X
	G3	0.35		X		X		X		X		
		0.45		X		X		X		X		
	G4	0.35		X		X		X		X		
		0.45		X		X		X		X		

[1] CEMENT CONTENT (%)

[1] see Figure 2.

Figure 2. Gradation of sand used in study.

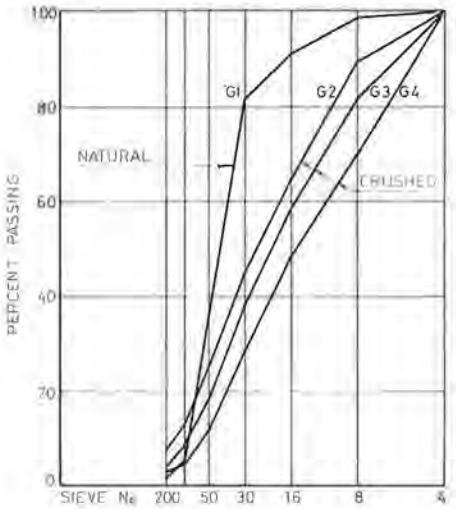

EXPERIMENTAL PROGRAM

Figure 1 shows the levels of the variables and their combinations considered in preparing the samples. The selected levels of cement content and the water-cement ratio (W/C) were based on previous experience with the technique (5) and on results of a few pilot trials. Minimum water requirements for aggregate absorption and cement hydration were also taken into consideration (7). The optimum conditions of coating were believed to lie within these selected levels.

The aggregates procured for the investigation were natural sand and crushed sand, which had particles of distinctly different shapes. Particles of the natural sand were rounded and very smooth, whereas those of the crushed sand were angular and slightly rougher in texture. Some of their properties are given below, and more information on the characteristics of the aggregates in the Arabian peninsula can be found elsewhere (8):

Property	Natural Sand	Crushed Sand
Sand equivalent (AASHTO T176)	58	41
Sodium sulfate soundness (AASHTO T104) (%)	9	6
Mineral composition (%)		
Quartz	90	87
Albite	2	5
Microcline	8	5
Calcite	--	3

As seen in Figure 2, one gradation (G1) was selected for the natural sand and three (G2, G3, and G4) for the crushed sand. These gradations represent the range within which sand is locally supplied for the production of cement-modified asphaltic concrete. The cement used for coating is an ordinary portland-pozzolan cement conforming to ASTM C595.

The techniques applied to evaluate the conditions of coating obtained in each sample will be described later.

SAMPLE PREPARATION

The steps followed in preparing the coated samples are summarized below:

1. The natural and the crushed sands brought to the laboratory were first separated into seven fractions each (ASTM Sieve Nos. 4, 8, 16, 30, 50, 100, 200) by dry sieving (ASTM C136).
2. By recombining the fractions on a weight basis, samples of natural sand and of crushed sand (2 kg each) were prepared according to the gradations shown in Figure 2. A sufficient number of samples was prepared to satisfy the requirements of the experimental program adopted in Figure 1.
3. Samples were oven-dried for 24 h at 70°C. Higher drying temperatures were avoided due to the presence of unstable constituents in the natural sand.
4. Cement coating was performed for each sample independently by using a kitchen-type mixer with a 5-L bowl. The cement was added to the aggregate first, and after 30 s of dry mixing, the predetermined amount of potable water was slowly added. Wet mixing was continued for 90 s. This sequence was selected to comply with that followed on site (5).
5. The treated samples were then transferred to trays and covered with plastic sheets for a curing period of 48 h, which is the minimum period specified in the local road construction documents (5).
6. After curing, each sample was air-dried at room temperature and then separated into seven fractions by using the same set of sieves as in step 1. The fractions thus obtained were kept, after weighing, in separate containers for subsequent analyses.

TECHNIQUES OF ANALYSIS

The cement coatings obtained at different treatments were compared and judged for relative quality by applying the following methods.

Visual Examination

Separated fractions of each sample after coating were visually examined and compared with corresponding fractions of other samples and of uncoated sand. This simple method, though subjective and qualitative, allowed useful differentiation among various sand fractions regarding cement distribution. Extreme states of coating were readily discernible to the trained eye. Thicker coats obviously acquired the distinctive gray color of the cement itself and appeared darker. Thinner coats, on the other hand, appeared lighter in shade, allowing the color of aggregate minerals to be partly visible. The visual examination was aided by a magnifying lens and was performed by the same oper-

Table 1. Characteristics of sand fractions used in specific-surface determination.

Characteristic	Sieve No. 4	8	16	30	50	100	200	Pan
Natural sand								
Bulk specific gravity	-	2.63	2.64	2.65	2.66	2.68	2.71	2.76
Maximum voids (%)	-	43.1	45.8	42.8	44.7	47.8	55.6	66.3
Minimum voids (%)	-	36.4	37.7	34.5	35.4	39.2	46.0	55.9
Shape factor	-	1.19	1.22	1.24	1.26	1.22	1.21	1.19
Crushed sand								
Bulk specific gravity	2.48	2.71	2.67	2.60	2.67	2.71	2.75	2.79
Maximum voids (%)	42.0	49.6	49.8	50.3	51.4	56.3	59.9	66.8
Minimum voids (%)	36.9	45.3	46.4	41.6	43.0	47.3	52.4	53.2
Shape factor	1.14	1.09	1.07	1.21	1.21	1.19	1.14	1.25

Table 2. Effect of cement content on gradations of natural sand.

Sieve No.	Gradation (% passing) Added Cement (%) 0	6	8	10	12	14
Natural Sand, W/C = 0.35						
4	100	100	100	100	100	100
8	98.2	98.3	98.5	98.6	98.9	98.3
16	93.2	93.6	94.0	94.0	94.2	93.9
30	82.5	84.5	85.2	85.0	85.7	84.6
50	36.6	45.5	45.8	44.2	42.6	34.9
100	5.4	8.7	8.7	7.5	5.9	4.7
200	1.6	4.1	4.0	3.0	2.0	1.7
Natural Sand, W/C = 0.45						
4	100	100	100	100	100	100
8	98.2	98.5	98.5	98.6	98.6	98.4
16	93.2	93.7	93.7	93.8	94.0	93.2
30	82.9	84.2	84.2	84.8	83.2	74.6
50	36.6	44.7	43.5	39.8	33.3	20.9
100	5.4	6.8	5.0	4.0	2.7	2.3
200	1.6	2.7	1.5	1.2	0.9	0.8

Table 3. Effect of cement content on gradations of crushed sand.

Sieve No.	Gradation (% passing) Added Cement (%) 0	7	9	11	13	15
Crushed Sand, W/C = 0.35						
4	100	100	100	100	100	100
8	89.1	89.6	90.1	90.1	90.6	90.6
16	64.0	66.1	67.0	67.0	67.3	67.1
30	45.0	48.2	48.8	48.9	48.6	47.2
50	25.6	29.6	29.9	29.1	27.6	24.9
100	13.3	17.6	17.4	15.3	12.6	9.6
200	6.4	10.4	8.7	6.3	4.1	3.2
Crushed Sand, W/C = 0.45						
4	100	100	100	100	100	100
8	89.1	89.7	89.0	89.9	90.3	90.2
16	64.0	66.4	66.3	66.1	65.8	64.6
30	45.0	48.2	47.9	46.8	45.5	41.9
50	25.6	28.5	27.6	25.1	21.8	16.2
100	13.3	15.3	17.1	9.0	6.2	4.7
200	6.4	7.7	4.4	3.0	2.3	1.8

ator to enhance consistency in judgments.

Particle-Size Distribution

The particle-size distributions of the coated samples were compared with each other and with the distribution before coating. The pattern of divergence in these gradations signified whether the added cement has actually coated the particles, remained mostly as free hydrated cement powder, caused the formation of concretions by cementing smaller particles together, or any combination of these effects.

Specific Surface

The specific surface (i.e., surface area per unit weight) was used as a characterizing parameter of the sand samples and as an indicator of their state of coating after treatment with cement. Samples of finer gradations or those with increased content of fines automatically resulted in higher values of specific surface.

The surface area of each fraction A was first calculated by assuming spherical particles, as follows:

$$A = 6W/G \cdot D_m \quad (1)$$

where

W = weight of aggregate fraction retained on particular sieve,
G = density of aggregate, and
D_m = mean diameter of aggregate fraction = (D_1 + D_2) ÷ 2, D_1 and D_2 being sizes of two successive sieves within which aggregate fraction lies.

The total surface area of a particular aggregate gradation A_t, taking surface irregularity of the particles into consideration, is as follows:

$$A_t = \sum_{i=1}^{n} [6W_i/(G_i \cdot D_{mi})] (CF)_i \quad (2)$$

where n is the number of sieves used in the analysis and CF is a correction factor representing the effect of particle angularity.

A specific gravity and a correction factor for each fraction of the crushed and the natural sand were determined separately. Determinations of the specific gravity were made according to AASHTO T84, T85, and T100, depending on the size of the particles considered.

Since there is no simple test available to correct for the effect of surface angularity (9), an empirical shape factor was calculated as the quotient of the maximum void ratio at the loosest state and the minimum void ratio at the densest state (10). Perfectly spherical particles of equal size were considered to have the same value for the maximum and minimum voids and thus a shape factor of a unity. Void ratios at the loosest and densest states were determined experimentally according to AASHTO T20. Results of specific-gravity and shape-factor determinations are given in Table 1.

Chemical Analysis

A quick chemical test was performed to determine the weight of cement in each fraction of the treated sand. The technique is based on dissolving the hydrated cement coat in diluted hydrochloric acid and observing the resulting change in the weight of the sample. Since the acid dissolves part of the original sand particles as well, this part had to be determined before the net weight of the cement coat could be obtained. This was done by adding the acid also to a blank sample of uncoated sand. Twelve pilot tests by using aggregates coated with predetermined amounts of cement have shown that this technique produced sufficiently accurate results for the purpose of this study, provided that each case is represented by a three-test average. It was found unnecessary, therefore, to apply the more sophisticated and time-consuming titration method of cement content determination (AASHTO T211).

The chemical analysis was performed on sand samples of gradations G1 and G2 only.

RESULTS AND DISCUSSION

By applying the above methods for evaluating the coated sand samples, the following results and observations were obtained.

The visual examination was first made on the whole sample (i.e., before sieving). It was found difficult in this way to identify sample-to-sample or fraction-to-fraction variation in the quality of the cement coat produced. Accordingly, observations were subsequently made on the basis of individual fractions after sieving. The descriptions obtained indicated that the uniformity of the resulting coats among various fractions of a particular sand sample depends highly on the amount of the cement added in the process. The higher the added cement was, the better were its distribution and the coating of the particles. A critical percentage, however, was visually identified beyond which particle agglomeration seems to occur. Such an optimum cement content was found to vary slightly with the quantity of added water and the initial gradation of the sand. Cement optima for natural sand at W/C ratios of 0.35 and 0.45 were observed at approximately 14 and 12 percent, respectively. Corresponding optima for crushed sand at the same levels of W/C ratio were observed at 15 and 13 percent for G2, 14 and 13 percent for G3, and 12 and 11 percent for G4. In other words, the coarser the sand, the less cement is needed to produce an optimum distribution.

Results of the particle-size-distribution analysis for the natural sand and for one gradation, G2 (as an example), of the crushed sand are listed in Tables 2 and 3. A comparison of the figures in these tables shows that the size distributions of the coarser fractions were minimally affected by the introduction of the cement. For the finer fractions, however, the effect of coating on gradation was tangible and had a definite pattern. At the lowest cement treatments of 6 percent and 7 percent, gradations were significantly finer than before coating. As the cement content increased, the divergence progressively narrowed, and at 14 and 15 percent, respectively, the gradations became coarser than before treatment. This trend is clarified in Figure 3 by plotting the percentage of added cement versus the amount of material passing the No. 200 sieve for the treated sand. It is believed that most of the increase in this fraction is due to the fact that free hydrated cement is unable to adhere permanently to surfaces of larger particles because of the mechanical agitation they received during or after treatment. The increased fines therefore indicate a waste of cement. The effect of increasing the W/C ratio to 0.45 was a reduction in the cement level at which this finest fraction reached its original value, as indicated by the horizontal dashed lines.

A typical set of calculations involved in surface-area analysis is given in Table 4; the following results were obtained for total surface area and specific surface:

Coating Cement (%)	Total Surface Area (cm^2)	Specific Surface (cm^2/g)
0	8 194	81.9
7	10 064	100.6
9	9 665	96.6
11	8 780	87.8
13	7 842	78.4
15	7 100	71.0

The consistently falling trend of the relationship between cement content and specific surface, shown in Figure 4, seems implausible, since by adding more cement the particles would become rougher and presumably of higher specific surface. However, this is true assuming that all the added cement would form a permanent coating on the particles of sand without changing the original number of these particles. Such an ideal coating was unobtainable because of two effects:

1. Not all the added cement contributed to the formation of a permanent coat. Under conditions of low cement and low water content, most of the cement was left free, which obviously increased the value of the specific surface of the whole sample, as seen on the left-hand side of Figure 4.
2. The actual number of individual particles of the sand is often reduced after the process of coating. While the sample was still wet, the finer particles, due to their light weight, were held together in groups or to surfaces of larger particles by the comparatively larger forces of water viscosity and surface tension. After hydration of the cement, many of these particles became inseparable; the net effect was a reduction in the total surface area of the sand sample. This behavior appeared to prevail at conditions of high cement and water contents as seen on the right-hand side of Figure 4. The final value of the specific surface of a treated sample would therefore depend on the extent to which each of the above conflicting effects takes place in the process.

Results of the chemical analysis are presented in Figures 5 and 6 for the natural sand and in Figures 7 and 8 for the finest of the three crushed-sand samples (G2). A sample of the computations involved is shown in Table 5.

At the lower level of W/C ratio, Figure 5 shows that the distribution of the added cement among the fractions of natural sand is most uniform at its highest content of 14 percent. At this level the concentration of the cement coat (grams per square centimeter) varied by 20 percent within most of the particle size range. As the amount of cement was reduced, its distribution became increasingly nonuniform. Particles between sieves No. 30 and No. 100 received the thinnest coatings, while disproportionate thicker coats were attracted by the finer material passing sieve No. 200. At the lowest treatment of 6 percent, the concentration of coating corresponding to this minus No. 200 sieve fraction is approximately 17 times that for the coarser fraction retained on sieve No. 50. Obviously this pattern is rather wasteful. It should be remembered

that the ultimate objective of the coating process is to make possible the production of better-quality asphaltic mixtures, largely by improving the surface texture of the aggregates used. A desirable pattern of cement distribution would accordingly be that producing preferential coating for those fractions of aggregate whose contribution to the frictional component of mix stability is maximum. The coarser particles of sand do contribute to this component; they are part of the load-bearing skeleton of aggregates in dense asphaltic mixtures. Consequently, the added cement should, in our view, mainly coat these coarser fractions rather than the finer particles whose function is more of filling the smaller voids within the structural matrix. Distributions similar to this were obtained generally at the higher levels of cement and water content as seen in Figures 6 and 8. Ryan (11), however, states in discussing aggregates for bituminous plant mixtures, "Particle shape and surface characteristics are just as important in the fine aggregate, even down to the minus 200 mesh or flow size as in the coarse aggregates...."

Generally the added cement produced better coatings for the crushed sand than for the natural sand. The variation in the concentration of the cement coat for most crushed fractions is negligible at the higher cement treatments (Figure 7). Moreover, the coarser particles retained on sieve Nos. 8, 16, and 30 received heavier coatings in this case compared with corresponding sizes of natural sand (Figure 5).

The effect of increasing the W/C ratio was beneficial in almost all the cases. Cement treatment of the natural sand at 8, 10, and 12 percent levels produced more uniform coatings (Figure 6), while for crushed sand the cement produced consistently heavier coats as the size of fraction increased (Figure 8).

From the results obtained in this investigation, it was found possible to define desirable minimum and maximum cement contents for each gradation and W/C ratio. The criterion for selecting a minimum cement content was the production of a coated sand that had basically the same gradation and specific surface as before coating. The maximum cement content was defined as the minimum percentage that would produce the most uniform coating on the sur-

Figure 3. Effect of cement content on fraction passing No. 200 sieve.

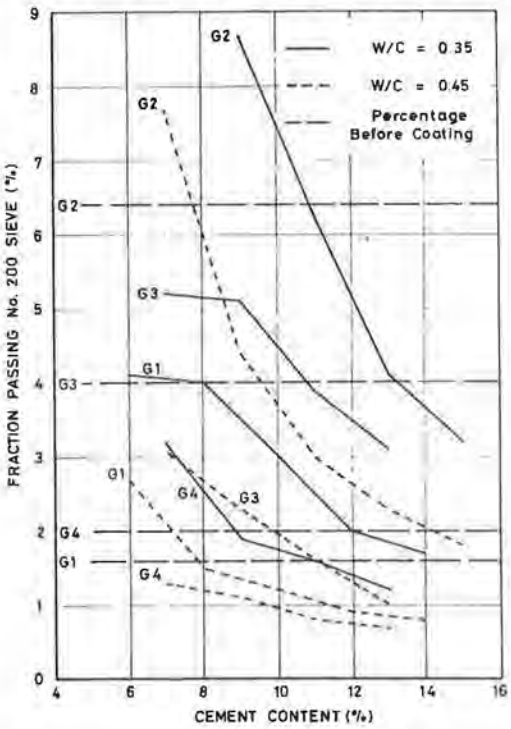

Figure 4. Effect of cement content on specific surface of sand.

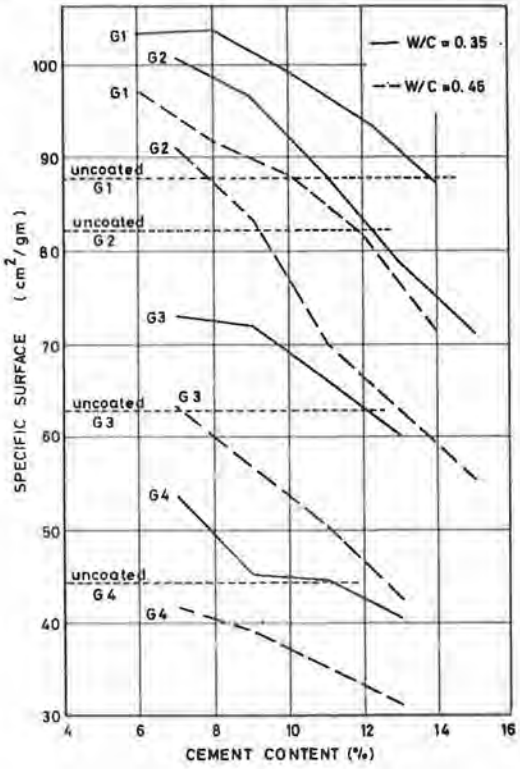

Table 4. Sample computations in determining specific surface of cement-coated sand.

Sieve No.	D_m (cm)	$[6(SF)/D_m(G)]$	Particle Surface Area[a] (cm^2) Coating Cement (%) 0	7	9	11	13	15
4	0.3555	-	-	-	-	-	-	-
8	0.1777	6.79	75	71	67	67	64	64
16	0.0890	13.54	339	317	313	313	316	318
30	0.0450	31.36	596	564	569	568	586	624
50	0.0225	60.48	1173	1122	1147	1198	1270	1349
100	0.0112	117.14	1476	1407	1458	1617	1757	1792
200	0.0056	221.06	1459	1600	1930	1990	1879	1415
Pan	-	480.63	3076	4984	4181	3028	1970	1538

[a]Based on the percentage retained on each sieve for an original sample of 2.0 kg.

face of different fractions of the sand. By using such limits, a useful form of presenting the results of the study is demonstrated in Figure 9. The three gradations of crushed sand (G2, G3, and G4) provided three points for defining each of the lines in Figure 9. Obviously, a similar presentation for the natural sand was not possible since only one gradation (thus, one value of specific surface) was investigated in this case.

CONCLUSIONS

1. The direct method of visually examining the treated sand allowed a satisfactory and a rapid evaluation of the quality of the cement coat produced, provided that the samples examined were first separated into a number of fractions by sieving.

2. In the treatment of sand with portland cement, two extreme states are distinguishable within which effective coating can be found. In one, often observed at low water and/or cement content, the added cement failed to adhere permanently to the surface of particles, and thus produced a poorly coated sand with an unnecessarily high content of fines. In the other, observed at high water and/or cement content, the finer fractions of the sand

Figure 5. Effect of cement content on its distribution among sand fractions: natural sand, W/C = 0.35.

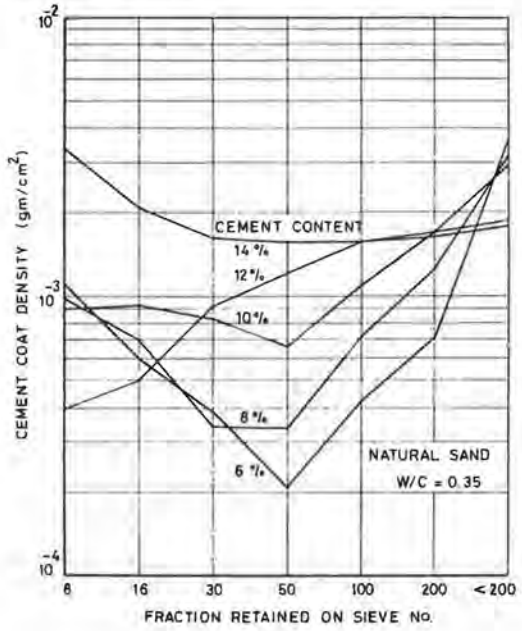

Figure 6. Effect of cement content on its distribution among sand fractions: natural sand, W/C = 0.45.

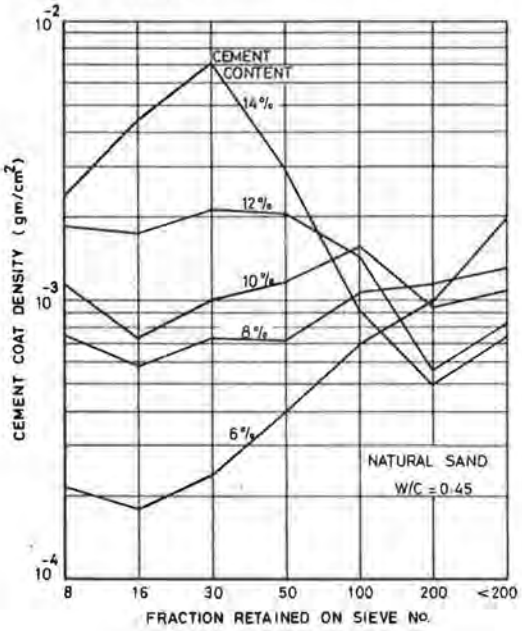

Figure 7. Effect of cement content on its distribution among sand fractions: crushed sand, W/C = 0.35.

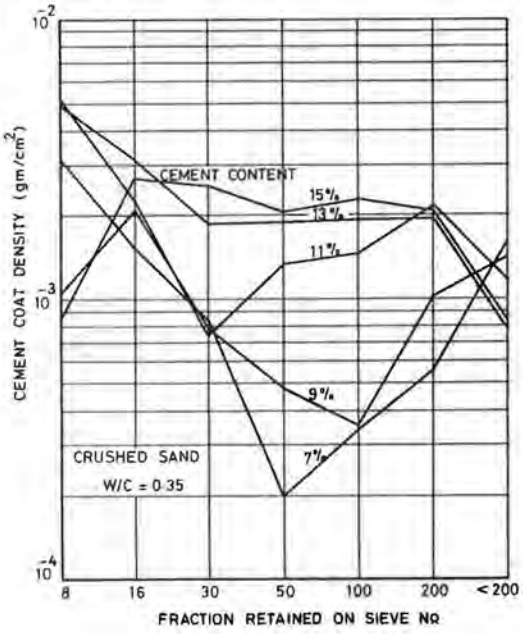

Figure 8. Effect of cement content on its distribution among sand fractions: crushed sand, W/C = 0.45.

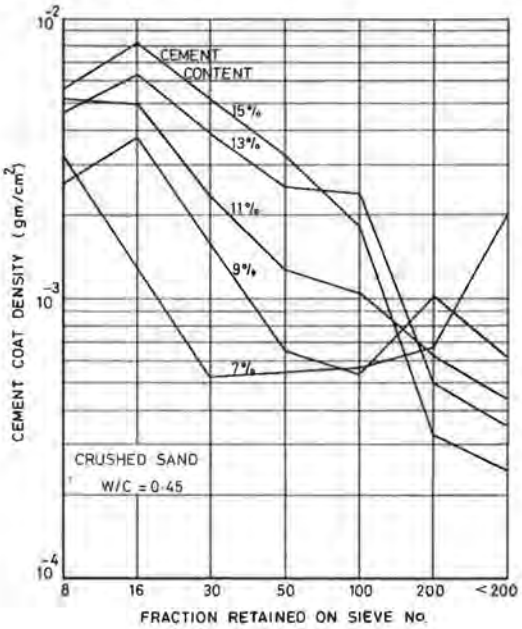

Table 5. Sample computations in determining cement distribution by chemical analysis.

Sieve No.	Coated Sample		Uncoated Sample				
	Weight (g)	Soluble Matter (%)	Weight (g)	Soluble Matter (%)	Cement Coat[a] (g)	Surface Area (cm^2)	Cement Coat Density[b] (g/cm^2) 10^{-4}
8	32.3	1.83	36.0	1.71	0.04	275	1.4
16	103.2	2.84	99.4	1.44	1.44	1 548	9.3
30	201.6	3.30	206.8	0.55	5.54	6 529	8.5
50	915.8	4.91	925.8	0.59	39.56	58 566	6.7
100	822.7	11.13	625.2	0.88	84.33	75 981	11.1
200	101.3	35.13	75.7	4.14	31.40	18 028	17.4
Pan	65.6	78.70	31.5	11.13	44.32	14 573	30.4

[a]Column 3 minus column 5 multiplied by 2, all of which is divided by 100.
[b]Column 6 divided by column 7.

Figure 9. Limits of cement content for coating crushed sand.

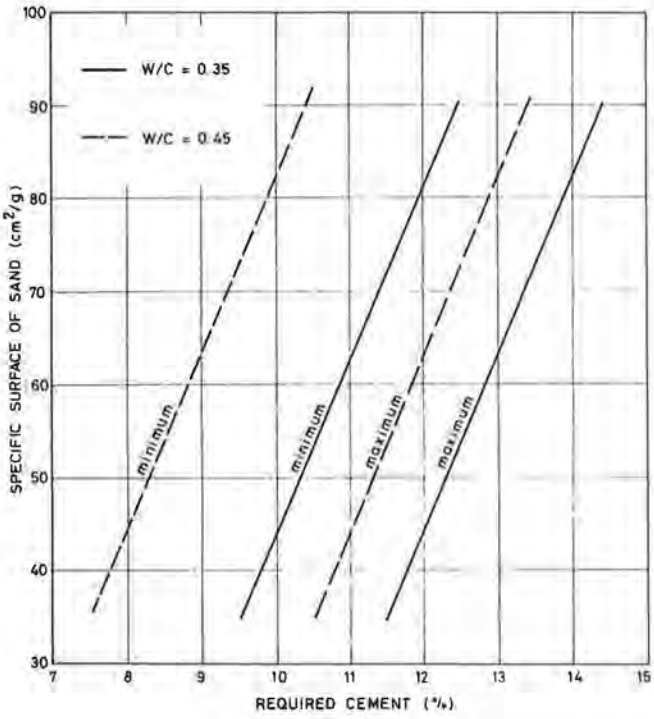

tended to form weakly cemented agglomerations that resulted in coarser gradations lacking in fines.

3. The investigation has shown that the amount of cement required for a proper coating needs to be rationally expressed by relating it to the surface area of the sand to be coated.

4. By defining limiting criteria for the percentage of added cement in the coating process (to avoid the objectionable extremes mentioned above), such a relationship as suggested in paragraph 3 above can be developed. In this study a relationship thus developed is shown in Figure 9 for the crushed sand.

5. For a particular value of specific surface of sand, the quantity of cement required for an optimum coating is found to reduce with an increase in the W/C ratio, within the extremes mentioned above.

ACKNOWLEDGMENT

This study was conducted at the Roads Research Center under the sponsorship of the Ministry of Public Works (Roads and Drainage Department), Kuwait.

We would like to thank S. Al-etr for her technical assistance; A. Allam, who did most of the laboratory work; and Y. Elfarra for conducting the chemical analysis.

REFERENCES

1. H.F. Winterkorn. Progress in Research on the Adhesion Between Mineral Fractions and Bituminous Materials. Proc., Montana National Bituminous Conference, 1938.
2. J.M. Griffith and B.F. Kallas. Influence of Fine Aggregates on Asphaltic Concrete Paving Mixtures. HRB Proc., Vol. 37, 1958.
3. R.A. Jimenez. An Apparatus for Laboratory Investigations of Asphaltic Concrete Under Repeated Flexural Deformations. Texas Transportation Institute, Texas A&M Univ., College Station, 1962.
4. C.L. Monismith. Influence of Shape, Size, and Surface Texture on the Stiffness and Fatigue Response of Asphalt Mixtures. HRB, Special Rept. 109, 1970.
5. Specifications for Road Works. Department of Roads and Drainage, Ministry of Public Works, Salmya, Kuwait, 1980.
6. H.R. Guirguis, O.E.K. Daoud, and S.K. Hamdani. Asphalt Concrete Mixtures made with Cement-Coated Aggregates. TRB, Transportation Research Record 843, 1982, pp. 80-85.
7. O.E.K. Daoud. Cement Hydration Effect on the Properties of Cement-Treated Asphalt Mix. Roads Research Center, Ministry of Public Works, Salmya, Kuwait, Internal Rept. 79/2, 1979.
8. D.M. Coulson. A Study of Concrete in the Middle East Using Local Aggregates and Hellenic Portland Cement. SRI International, Menlo Park, CA, Aug. 1979.
9. A.M. Neville. Properties of Concrete. Pitman Publishers, Ltd., London, 1975.
10. I. Kamel. Design of Mixes for High Quality Concrete Using Surface Analysis. Ain Shams Univ., Cairo, Egypt, M.S. thesis, 1964.
11. A.E. Ryan. Discussion of Plant Mixes. Crushed Stone Journal, Vol. 29, No. 1, March 1954.

Publication of this paper sponsored by Committee on Mineral Aggregates.

Rock Aggregate Management Planning for Energy Conservation: Optimization Methodology

FONG-LIEH OU, WALLACE COX, AND LEE COLLETT

A mixed-integer programming approach is used to develop a rock aggregate management planning process. The basic objective is to minimize the use of aggregate materials and energy in transportation construction. Two models developed by the U.S. Forest Service are adopted for developing the planning process. Model 1, a minimum-path model, is used to evaluate the need of aggregate materials based on the least combined cost of vehicle operation, road maintenance, road construction and reconstruction, and environmental protection. Model 2, a rock aggregate shipment model, is utilized to allocate aggregate materials from the source to the project based on the least combined cost of transporting materials and material production. Since fuel cost accounts for more than 20 percent of the cost for hauling materials and material production, the process is considered to be energy-sensitive. The process is applied to the plan for developing and allocating aggregate materials in the Mount St. Helens volcano area of the Gifford Pinchot National Forest. The aggregate is used to reconstruct the system for transporting the timber from the forest's recurring annual harvest, as well as the salvage timber resulting from the Mount St. Helens volcanic eruption of May 18, 1980. The process is an extension of the urban transportation planning system process and can be applied to areas other than the forest land.

The construction of transportation facilities consumes billions of tons of rock aggregate annually. Like many other materials, the aggregate is in finite quantity and quality. It is nonrenewable and, depending on local geology, may be extremely limited. As a consequence, geographic distribution and quality often do not match requirements. The result is that hauling aggregate can consume large quantities of energy, and thus aggregate that is normally inexpensive can become quite costly.

The use of energy to transport aggregate materials has not been explicitly considered in aggregate management planning. However, energy consumption has become a significant factor in transportation planning because of transportation's heavy reliance on apparently inadequate oil supplies as a primary source of energy. Since expected oil supplies will probably not satisfy projected oil consumption in the future, conservation is considered as an appealing means for overcoming the fuel shortage.

The purpose of this paper is to develop a rock aggregate management planning process based on mixed-integer linear programming (MILP) techniques. The process would lead to minimizing the use of aggregate materials and energy in transportation construction. Its applicability has been demonstrated by a case study for the development of a rock aggregate management plan for the Mount St. Helens volcano area.

ENERGY SAVINGS AND AGGREGATE MANAGEMENT PLANNING

The objective of rock aggregate management planning is to establish a basic planning policy for evaluation, utilization, and conservation of rock aggregate resources in support of public needs. Aggregate resources are those occurrences of rock, gravel, sand, silt, and clay materials that are of sufficient quality to be utilized as construction materials. These resources exist in varying quantity and quality on U.S. lands and provide the major material source for road metal, concrete aggregate, asphalt pavement, and structural foundation reinforcement. They cannot be regenerated or replaced at a rate comparable with that of their extraction.

The rock aggregate management program as shown in Figure 1 indicates that the first step toward effective aggregate management is to make an inventory of all aggregate sources within the area of interest. It includes the determination of past activity for each site, estimation of quantity and quality remaining, assignment of a use potential for the future, and estimation of the work needed for continued resource development. Concurrently, a step is taken to identify the present and potential demand. Based on the quantity and quality of both supply and demand, the distribution pattern of the aggregate may be determined. The performance of these three steps in the first phase facilitates the necessary information for developing the master plan. The next phase of the program is to monitor the aggregate management plan and determine how well the plan meets the established land-management objectives and planned targets. This assessment provides information for improving the management plan. The last two phases are to develop a pit or quarry operating plan and specify requirements for surface restoration and temporary erosion measures needed to protect the aggregate resources. The major concern of this study is to develop a planning process for optimal use of aggregate and energy as shown in the first phase of the planning program. The costs of energy consumption of other phases are to be used as inputs to this process.

Since energy cost accounts for about one-third of rock aggregate transportation cost, the distance between the source and the project plays a key role in conserving energy. One way to reduce the haul distance is the optimization of road design for aggregates to make the best use of local materials. This can be achieved by providing alternatives for use of different levels of base, subbase, and asphalt pavement materials.

After the location, quantity, and quality of both supply and demand are identified, the plan for further energy conservation relies on the selection of the path with the least consumption of energy (or with the least haul cost) for transporting materials. The least-haul-cost algorithm then directs the material distribution pattern and will not allow aggregate cross haul. The selection of least-cost path depends on the vertical profile, horizontal alignment, and roadway characteristics, such as designed surfacing and system reliability, which all influence the fuel consumption of vehicles using a particular road. However, route characteristics are different from one path to another. Improving road conditions of a particular route may change another path selection in favor of that route. Thus the system improvement should be included in the path-selection process. Since the social and environmental impacts are of concern, the selection of a particular mode and a least-cost path should be subjected to both social and environmental constraints.

Beside transporting materials, material production also consumes fuel. As indicated by Kirby and Lowe (1), production activity can be divided into three components: site development, site restoration, and manufacturing process. Site development

Figure 1. Rock aggregate management planning program.

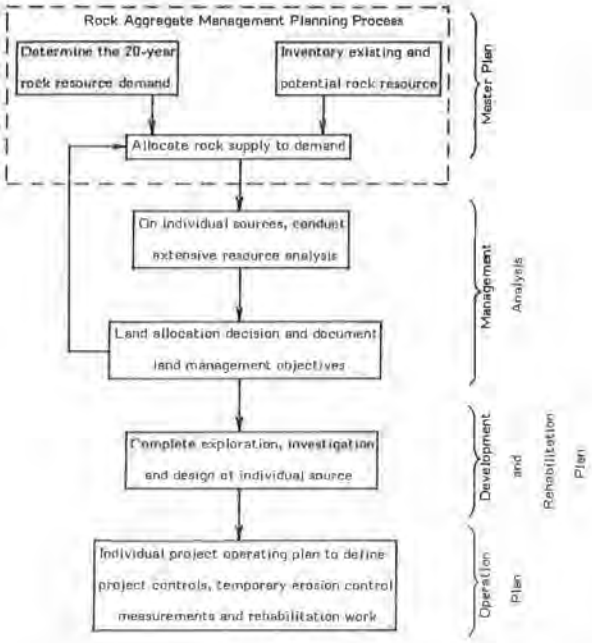

consists of providing an access road, clearing vegetation, removing overburden for opening a pit or a quarry, and transporting and setting up equipment that remains on site. Site restoration includes removing all equipment, cleaning and smoothing up the area, restoring a required thickness of topsoil, reestablishing vegetation, and obliterating the access road. The manufacturing process consists of pit or quarry development, material processing, and pit or quarry restoration. Fuel costs account for 15-20 percent of total costs involved in each of the above activities. Energy conservation in the manufacturing process can be achieved by the optimization of road design as indicated previously. The fuel consumption for site development and site restoration may be reduced if the demand is temporally and spatially continuous. Under this condition the number of pits or quarries needed to be open is minimal and the frequency of equipment movement may be reduced. Thus the time period of road construction becomes one of the important features in determining energy conservation. Note that action to reduce environmental impact also should be considered in each of the above activities.

The foregoing discussion indicates that almost all decisions concerning location, basic design, schedule, travel path, and materials used in constructing a roadway have profound implications for energy consumption. Decisions made today in which one alternative is chosen over another influence energy consumption now and, perhaps more important, have ramifications that will affect energy consumption for years to come. There is a pressing need to use an optimization technique developed in accordance with the aforementioned factors in making an effective aggregate management plan. This need has been recognized by the panel of a three-day workshop, Optimizing the Use of Materials and Energy in Transportation Construction, November 12-14, 1975, which was sponsored by the Federal Highway Administration, the Energy Research and Development Administration, and the Federal Energy Administration and conducted by the Transportation Research Board (2).

PLANNING METHODOLOGY

Current Approaches

The formulation of an aggregate management planning process involves two major tasks. Given an existing network, the first task is to select a least-cost path based on a list of improvement options for various links, the projected traffic volume between various origin and destination pairs, and the selected optimal set of links to be improved or added to the existing network. In other words, based on the least combined cost of vehicle operation, system improvement, and road maintenance, the first task of the process chooses the optimal set of links to be improved or added and assigns the projected traffic to the new system simultaneously.

Various network design models have been developed to solve the least-cost-path problem (3,4). The present study selected a network model developed by Kirby, Wong, and Cox for single-commodity applications (5) and expanded by Ou, Cox, and Collett for multicommodity applications (6). Kirby's model is an MILP model that allows the project cost, vehicle operation cost, road maintenance cost, and the cost of environmental protection to be considered simultaneously to obtain an optimal solution. It has been used by many national forests across the country for timber sale appraisal. This model is referred to as Model 1 in the rest of this paper.

In Model 1, the network connectivity is modeled by a set of arcs. The nodes are numbered, and contiguous arcs are defined by common node numbers. Since the model represents the actual movement of vehicles through defined physical areas, both pits or quarries and roads for construction are also represented by nodes and arcs. In addition to connectivity, the arcs are defined by the following network parameters: length (miles or kilometers), capacity (vehicles), average speed (miles or kilometers per hour), nominal travel time (minutes), and average cost.

The second task in developing the aggregate management planning process is to derive an algorithm by which the process is able to allocate rock supply to demand based on the least cost of transporting materials and material production (including environmental protection). A rock aggregate shipment model developed by Kirby and Hager (7) was selected for this purpose. The model is still in the experimental stage and is referred to as Model 2. It is an integer linear programming model and employs a 0,1 type of variable that behaves as an integer variable.

The concepts and mathematical formulations of Models 1 and 2 as discussed above were adopted to develop a rock aggregate management planning process, presented in the next section.

Mathematical Programming Approach for Aggregate Management Planning

Based on the above discussion of factors related to a rock aggregate management plan, the mathematical derivation of an aggregate material allocation process follows. Let F be the set of destinations and G the set of origins for aggregate material type a. Let t be the index number of the time period and $a_{am}X_{amijht}$ be the amount of type-a aggregate hauled from origin i to destination j via path h during period t [where a is the load per vehicle; X is the traffic volume; m (number of modes) = 1,2,3,...,M; i = 1,2,3,...,I; j = 1,2,3,...,J; and t = 1,2,3,...,T]. Finally, let $F_t \subseteq F$ be the set of destinations for which the material can be developed from the set of origins $G_t \subseteq G$ in the period of t.

Note that F_t and G_t will not necessarily contain all the elements of F and G, respectively. For example, if all types of needed aggregate materials are at destination j at time t, then $i \subseteq G$ and $j \subseteq F$ but $i \notin G_t$ and $j \notin F_t$.

The selection of origin i for developing $\alpha_{am} X_{amijht}$ and hauling it to destination j in time t is based on an objective function that minimizes the costs of total material, which includes transportation, site development, periodic fixed items, manufacturing process, site restoration, project construction, road maintenance, and environmental protection. An MILP formulation can be made by considering multiorigins, multidestinations, multimodes, and multiple time periods. The formulation may also take into account options of timing, location, quality and quantity of material development, as well as road construction and maintenance operations. It takes the following form:

$$\text{Minimize } Z = \sum_t WP_t \left[\sum_i \left(Y_i \phi_{it} + U_{it} \pi_{it} + W_i \psi_{it} + \sum_{amj} C_{ait} \alpha_{am} X_{amijt} + \sum_{amjh} C_{mijht} \alpha_{am} X_{amijht} \right) + \sum_{bmijh} C_{mijht} \alpha_{bm} X_{bmijht} + \sum_r K_{rt} \theta_{rt} \right] \quad (1)$$

Subject to supply constraints:

$$\sum_{mjh} \alpha_{am} X_{amijht} \leq V_{ait} \pi_{it} \quad (2)$$

Subject to:

$$\phi_{it} \leq \pi_{it} \quad \text{for all resource a, origin i, time period t} \quad (3)$$

Demand constraints:

$$\sum_{ihm} \alpha_{am} X_{amijht} = V_{ajt} \quad \text{for all resource a, destination j, time period t} \quad (4)$$

Link-capacity constraints:

$$\sum_{amijh \in \{L_{nt}\}} \beta_{it} (X_{amijht} + X_{bmijht}) \leq X_{nt} \quad \text{for all link n, capacity period t} \quad (5)$$

Project-construction-requirement constraints:

$$\sum_{amijh \in \{P_r\}} X_{amijht} + \sum_{bmijh \in \{P_r\}} X_{bmijht} \leq \sum_{\tau=1}^{t} g_r \theta_{r\tau} \quad \text{for project r, time period t} \quad (6)$$

Site-development constraints:

$$\sum_{\lambda=1}^{t} \phi_{i\lambda} \geq \pi_{it} \quad \text{for all origin i, time period t} \quad (7)$$

$$\sum_{\lambda=t}^{T} \psi_{i\lambda} \geq \pi_{it} \quad \text{for all origin i, time period t} \quad (8)$$

$$\sum_{amjh} \alpha_{am} X_{amijht} \geq \phi_{it} \quad \text{for all origin i, time period t} \quad (9)$$

$$\sum_{amjh} \alpha_{am} X_{amijht} \geq \psi_{it} \quad \text{for all origin i, time period t} \quad (10)$$

The variables are as defined below:

Notation	Variable
Z	Sum of material production cost and transportation cost
WP_t	Present value of 1 expended at beginning of time period t
Y_i	Fixed site-development cost at site i
U_{it}	Periodic fixed cost at supply site i for every operation period t
W_i	Fixed site-restoration cost (including environmental-protection cost) at site i
C_{ait}	Manufacturing-process cost per unit of aggregate material a at site i during time period t
X_{amijht}	Traffic volume between origin i and destination j hauling aggregate material a via route h by mode m during time period t
X_{bmijht}	Traffic volume between areas i and j for transporting commodity b via route h by mode m during time period t (where b = 1,2,3, ..., B and commodity b includes persons when mode m represents passenger vehicles)
C_{mijht}	Round-trip vehicle operating cost of mode m in time period t and route ijh including user's cost and operator's road-maintenance cost
K_{rt}	Sum of construction cost and environmental-impact cost of project r if the project is selected in time period t
π_{it}	1 if site i is operational in period t, 0 otherwise
ϕ_{it}, ψ_{it}	Continuous nonnegative variables that behave like integers; that is, ϕ_{it} = 1 if the first operation period of site is period t, 0 otherwise, and ψ_{it} = 1 if the last operation period of site i is period t, 0 otherwise
α_{am}, α_{bm}	Load per vehicle of mode m for aggregate material a and commodity b, respectively
θ_{rt}	1 if project r is built in period t, 0 otherwise
V_{ait}	Amount of aggregate material a available at site i during period t
V_{ajt}	Amount of aggregate material a required at destination j during period t
β_{it}	Portion of traffic flow from origin i in time period t that occurs during link capacity period
X_{nt}	Maximum permissible traffic over a period of time on link n in time t
$\{L_{nt}\}$	Set of routes ijh that use link n during time period t
$\{P_r\}$	Set of routes ijh that require the construction of project r
g_r	Arbitrary large constant greater than the overall traffic volume in all periods that use links covered by project r

In words, Equation 1 is an objective function that aims to minimize the sum of costs of resource-site development, periodic fixed items, fixed site restoration, manufacturing process, transportation, road construction, and related environmental protection. The transportation cost accounts for both vehicle-operating and road-maintenance costs. The road-construction cost considers any expense for improving the transportation system, including constructing new facilities and reconstructing existing facilities. The periodic fixed cost includes royalties, while the costs of other items are as defined previously.

Equations 2, 3, and 4 are constraints on the traffic generated in origins and attracted to destinations in time t. Equation 5 describes constraints

on the capacity of a particular link in time t, while constraints related to project construction in terms of construction cost and environmental-protection cost are shown in Equation 6. Finally, Equations 7, 8, 9, and 10 present the site-development constraints that allow the site development to be a factor for determining the resource-site selection.

The purpose of considering multiple time periods is twofold. First, it provides an option for estimating project-construction cost with discount rate. In a regionwide transportation system improvement, the road construction or reconstruction usually takes place during more than one period of time. Second, the multiple time period allows the estimation of rock aggregate needs in different periods of time that could be used to determine the economic feasibility of opening a new pit (or quarry) or reopening an old pit (or quarry). The site-development costs are substantially different between a new pit (or quarry) and an old one.

It should be noted that in the development of Model 1 for minimum-path network analysis, both lower bounds and higher bounds of the resource quantity in terms of supply and demand were considered. Such a consideration is a requirement to achieve an optimization solution. The first minimum user's cost path through the transportation system is generated by Martin's standard labeling algorithm (8), while the next minimum paths are found by a modified Hoffman-Pavely algorithm (9).

The derived optimum path must be included in the set of paths derived from the n best user-path algorithms. The best or second-best user path may not be the optimum path subject to other costs and constraints. The relationship of the best user path to the optimum path is a function of user numbers or traffic volume and its ability to offset other costs and constraints. In a low-volume or short-planning-horizon situation it may be difficult to obtain this route by utilizing a minimum-user-cost algorithm. Kirby and others have suggested a simultaneous solution to this type of problem by utilizing conservation-of-flow equations within the MILP application (3). In a multimode, multitrip-purpose, multitime-period situation, this usually creates a very large and unyielding problem. The advantage of using a minimum-user-cost-path algorithm is that it causes many superfluous or spurious combinations to be pared off.

Aggregate Management Planning Process

In accordance with the above theoretical framework, a rock aggregate management planning process was developed. It consists of the following steps:

1. Inventory (land use, rock aggregate and other resources, population, traffic, and transportation facilities);
2. Land-use forecast;
3. Trip generation;
4. Modal split;
5. Trip distribution, network assignment, and project selection;
6. Estimation of rock aggregate demand;
7. Examination of the impact of rock haul on general traffic and repetition of steps 3-6 if the impact is significant;
8. Estimation of fixed cost, manufacturing cost, transportation cost, and placement cost;
9. Allocation of rock aggregate supply to demand; and
10. Evaluation of the difference between the resultant rock-haul traffic and that estimated in step 7 and repetition of steps 3-9 if the difference is significant.

The sequence of these steps is shown in Figure 2.

The first step includes an inventory of existing traffic throughout the whole region of interest together with inventories of land use, rock aggregate and other resources, socioeconomic characteristics of the population, and the existing transportation facilities. The second step is to forecast the land use that should occur in the forecast period. The next two steps are to predict the traffic demand by mode that may be anticipated and the way in which this will occur throughout the region. The fifth step is composed of an optimization procedure of trip distribution, network assignment, and project selection. It is carried out by Model 1, the minimum-path model that uses the least combined cost in terms of vehicle operation, road maintenance, road construction, and environmental protection. Step 6 is to estimate the rock aggregate demand by types of material such as plant-mix, base, subbase, and subgrade alteration and by periods of project construction. The option of subgrade alteration is to use native material for the substitution of base and/or subbase. It is designed to conserve high-quality rock and reduce fuel consumption. The seventh step is to examine the impact of traffic generated by hauling rock aggregate on the general traffic flow. If the impact is significant, it may change the system improvement and therefore the need for rock aggregate. This would require a repeat of the process from steps 3 to 6. The eighth step includes estimating various costs related to rock aggregate allocation, such as fixed items, manufacturing, rock hauling, and placement. As indicated previously, the fixed costs are the sum of costs for developing, maintaining, and restoring a quarry or pit as well as for setting up and removing equipment. Manufacturing, rock hauling, and placement are costs per unit volume of a specific type of material. As shown in Figure 2, the haul cost is estimated by using Model 1 in accordance with the proposed network and the future traffic (including rock haul).

The ninth step is to allocate the rock supply to demand by using Model 2, the rock aggregate shipment model. The inputs of the model are the cost items as mentioned together with the quantity and quality of rock aggregate supply and demand. The outputs of Model 2 include both cost and material summaries. The cost summaries contain material manufacture, material transportation, and the sum of the two. They are specified by type and period for each road. The material summaries include (a) material manufactured at each quarry or pit by type and period, (b) flow of material from quarry or pit to road by type and period, (c) amount of material placed on each road by type and period, and (d) amount of subgrade alteration on each road and period during which the treatment is done.

The last step is to examine the actual impact of traffic generated from hauling rock aggregate on the general traffic flow. If the actual impact is significantly different from that estimated in step 7 and used in step 8, the iteration of the process from steps 3 to 9 must continue. However, if data for both rock aggregate supply and demand are available, the execution of steps 8 and 9 may result in a primary rock aggregate allocation.

Note that steps 1 to 5 are consistent with the Urban Transportation Planning System (UTPS) process. Thus the rock aggregate management planning process can be considered as an extension of the UTPS process.

The case study below demonstrates the application of the rock aggregate management planning process to the Mount St. Helens volcano area of the Gifford Pinchot National Forest, Skamania County, Washington.

Figure 2. Rock aggregate management planning process.

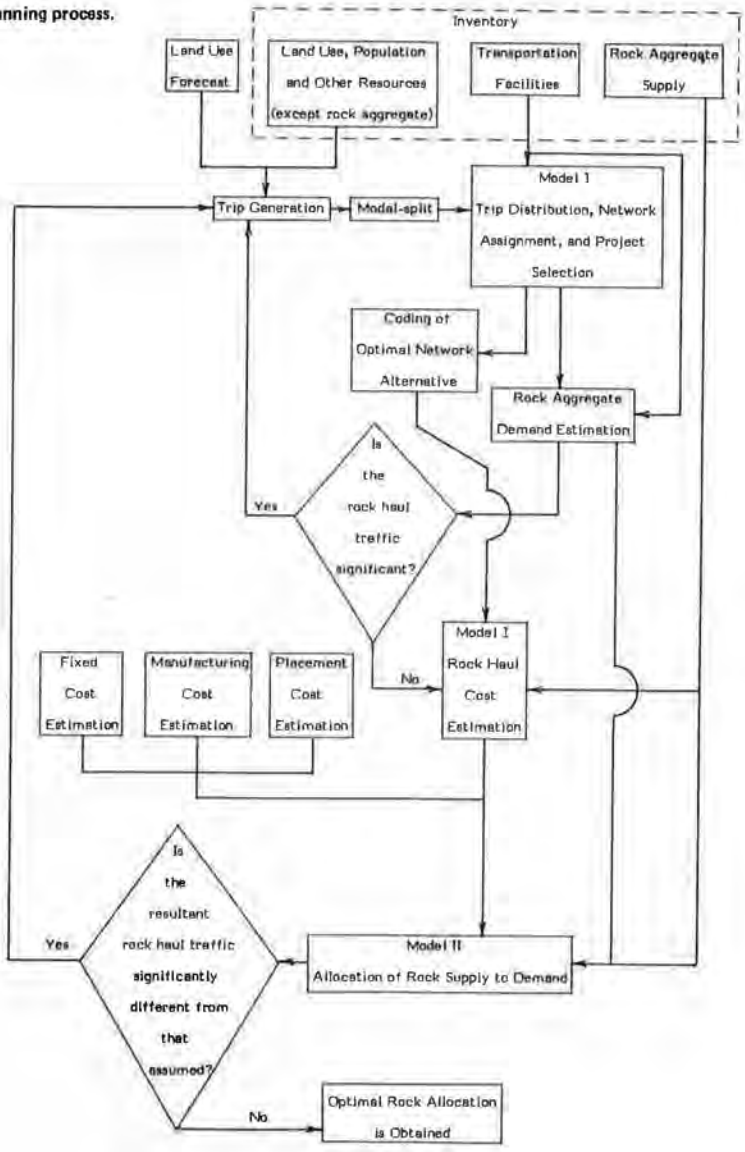

CASE STUDY

Figure 3 shows the forest transportation system in the Mount St. Helens volcano timber salvage area. A great portion of this system was damaged by the volcanic eruption of May 18, 1980. In order to provide access for transporting salvage timber and other land-management activities, the system must be improved. The plan for system reconstruction was carried out by using the rock aggregate management planning process.

Three items for the inventory were timber harvest, transportation system, and rock aggregate resources. It was estimated that 1250 million board feet (mmbf) of timber with 700 mmbf of salvage sale, 300 mmbf of green sale, and 250 mmbf of private sale are to be hauled through the volcano-area transportation system in the next two seasons. The examination of road conditions found that the system requires 44.1 miles (71 km) of asphalt pavement overlay and 103.1 miles (165.9 km) for rock aggregate surfacing. In addition, 62.5 miles (100.6 km) of forest road may require new asphalt pavement. The need for pavement was justified by the economic feasibility of construction costs versus savings of vehicle-operating and road-maintenance costs. The primary investigation of rock aggregate supply indicated that there are 18 candidate quarries with a total of 1 263 000 yd^3 (965 627 m^3) including 240 000 yd^3 (183 492 m^3) of plant-mix, 482 000 yd^3 (368 513 m^3) of base, and 541 000 yd^3 (413 622 m^3) of subbase.

Since the main purpose of improving the system in the volcano area is to haul salvage timber, the second step of the planning process, the land-use forecast, becomes unnecessary. By using Model 1, steps 3 to 5 of the process were performed to determine the road segments of the 62.5 miles for pavement. The result of an optimal solution indicated that 25 miles (40.2 km) of the 62.5 miles would be more economically efficient if they were paved. However, 4.5 miles (7.2 km) of the road recommended for pavement was considered infeasible from the point of view of road management. It should be noted that prior to the analysis of steps 3 to 5, two policy options can be made to improve the 62.5-mile system. The first option is the "do-nothing" alternative, i.e., leave the system as it is and without improvement. Based on this scenario, it would cost $15 million (including both vehicle-operating and road-maintenance costs) for hauling 700 mmbf of salvage timber. The second option is to

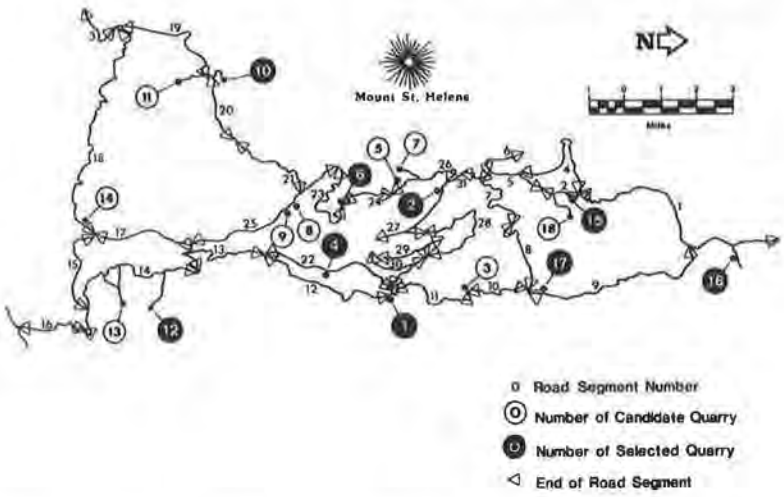

Figure 3. Location of quarries and road segments in Mount St. Helens volcano timber salvage area.

Table 1. Aggregate demand by roads and aggregate supply by quarries.

Project Demand by Road Segment	Source Supply by Quarry	Rock Aggregate (yd^3)			
		Total	Plant-Mix	Base	Subbase
R01	Q16	22 950	22 950	0	0
R02	Q15	6 200	0	1 450	4 750
R03		0	0	0	0
R04	Q15	28 200	0	9 800	18 400
R05	Q15	10 750	0	6 250	4 500
R06	Q02	6 050	0	3 750	2 300
R07		16 800	11 600	0	5 200
	Q07	11 600	11 600	0	0
	Q07	5 200	0		5 200
R08	Q17	4 250	4 250	0	0
R09	Q17	26 100	26 100	0	0
R10	Q17	5 700	5 700	0	0
R11	Q04	3 200	3 200	0	0
R12	Q04	14 600	0	14 600	0
R13	Q04	25 600	9 530	16 070	0
R14	Q12	5 700	0	5 700	0
R15		0	0	0	0
R16	Q12	18 800	8 800	10 000	0
R17	Q04	9 300	9 300	0	0
R18		0	0	0	0
R19	Q10	6 450	0	6 450	0
R20	Q10	4 150	0	4 150	0
R21	Q10	4 150	0	4 150	0
R22	Q04	6 300	6 300	0	0
R23	Q06	9 850	0	5 750	4 100
R24	Q06	14 750	0	3 000	11 750
R25		0	0	0	0
R26	Q06	2 900	0	2 900	0
R27	Q02	16 800	0	5 100	11 700
R28		19 200	0	9 000	10 200
	Q01	10 200	0	0	10 200
	Q04	9 000	0	9 000	0
R29		11 930	0	7 730	4 200
	Q01	4 200	0	0	4 200
	Q04	7 730	0	7 730	0
R30		8 040	0	6 050	1 990
	Q01	1 990	0	0	1 990
	Q04	6 050	0	6 050	0
R31	Q02	8 300	0	3 800	4 500
Total		317 020	107 730	125 700	83 590

Note: 1 yd^3 = 0.764 55 m^3.

pave all of the 62.5 miles of forest roads. This option would require $6 250 000 of pavement cost and $9 659 000 of haul cost, or a total of about $16 million of transportation cost to haul the timber volume mentioned. However, with consideration of 20.5 miles (33 km) for pavement, it only costs $14 049 000 for timber haul and road reconstruction. The savings of the selected alternative compared with the "do-nothing" and "pave-all" alternatives are $943 000 and $1 860 000, respectively. Since fuel cost accounts for more than 20 percent of haul cost and road-construction cost, the selected alternative would conserve from $188 600 to $372 000 worth of fuel.

In step 6, estimates were made for the rock aggregate demand of system improvement including 44.1 miles (71 km) for asphalt overlay, 103.1 miles (165.9 km) for rock aggregate surfacing, and 20.5 miles (33 km) for new asphalt pavement. The projected demand would be 395 000 yd^3 (302 000 m^3) of aggregate with 107 730 yd^3 (82 365 m^3) of plant-mix, 125 700 yd^3 (96 104 m^3) of base, and 83 590 yd^3 (63 909 m^3) of subbase. The result of the analysis in step 7 indicated that the traffic demand of hauling aggregate is relatively small when compared with the traffic generated by transporting timber. Thus the effect of rock haul on aggregate demand was considered to be insignificant. Based on the estimated supply and demand, haul costs per unit of aggregate from each candidate quarry to road segments were estimated by using Model 1.

After completion of step 8, the estimated costs, including fixed items, manufacturing, transportation, and placement along with the quantities of demand and supply, were used as the inputs to Model 2 for rock aggregate allocation. The results of step 9 are presented in Table 1.

As shown in Table 1, nine quarries were selected from the 18 candidate quarries. This material allocation pattern would result in $592 000 of haul cost, $1 209 000 of placement cost, $2 000 000 manufacturing process cost, $94 000 of site-development cost, and $4500 of site-restoration cost, for a total of $3 899 500. This total is approximately 20 percent of the $20 million project for constructing and reconstructing the transportation system in the Mount St. Helens volcano timber salvage area. In this study the fourth type of material, the subgrade alteration, which would use native material as a substitute base and/or subbase, was not considered. The system improvement was scheduled for one point of time; therefore only one time period was used in this particular application. The traffic of rock haul was found to be insignificant when compared with the general traffic. Thus step 10 of the process was not executed. The result of this study provided a general guideline for improving the volcano-area transportation system, which is planned to be reconstructed in spring 1982.

CONCLUSION

As part of the planning process to develop a forest

rock aggregate management plan, the Gifford Pinchot National Forest, of the U.S. Department of Agriculture, Forest Service, used the available techniques from the Forest Service and developed a rock aggregate management planning process that can be applied to areas other than the forest land. The process could generate an optimal rock aggregate allocation pattern based on the least cost as well as least fuel consumption.

The planning process has been applied to the Mount St. Helens volcano timber salvage area to determine the rock aggregate needs and to allocate them for transportation system construction. The result of the application indicated that the process allows the examination of complex options and alternatives conveniently. The planner may use it to develop an aggregate management plan for a specific project or for a region under a pressing deadline. Its consideration of fuel consumption may increase the planner's confidence in optimal use of aggregate materials and energy.

ACKNOWLEDGMENT

We wish to express our appreciation to Peter Wong, Malcolm W. Kirby, and Allan J. Hessell for their helpful comments. The provision of necessary data for this project by William Powell and Allen Morrissette is acknowledged. Special thanks go to Melroy H. Teigen and David B. Trask for their support. We of course accept sole responsibility for the contents of this paper.

REFERENCES

1. M.W. Kirby and R.J. Lowe. Optimal Policies for Transporting Rock Aggregate to Low-Volume Roads. In Low-Volume Roads, TRB, Special Rept. 160, 1975, pp. 296-304.
2. Optimizing the Use of Materials and Energy in Transportation Construction. TRB, Special Rept. 166, 1976.
3. E.K. Morlock, N.L. Nihan, and R.F. Sullivan. A Multimode Transportation Network Design Model. Research Department, Northwestern Univ., Evanston, IL, 1970.
4. F. Ochoa-Ross and A. Silva. Optimum Project Addition in Urban Transportation Network via Descriptive Traffic Assignment Models. In Search and Choice in Transport System Planning, MIT Press, Cambridge, MA, Vol. 5, 1968.
5. M.W. Kirby, P. Wong, and W. Cox. Optimization of Rural Road Networks--An Application of the Timber Transshipment Model. In Roads of Rural America, U.S. Department of Agriculture, 1979, pp. 17-26.
6. F.-L. Ou, W. Cox, and L. Collett. An Optimization Approach for Transportation System Analysis. Proc., 12th Modeling and Simulation Conference, Pittsburgh, PA, 1981, pp. 1579-1584.
7. M.W. Kirby and W. Hager. Resolving Conflicts in Transport of Rock Aggregate--A Cost Analysis. Journal of Forestry, Vol. 76, No. 5, May 1978, pp. 286-289.
8. B.V. Martin. Minimum Path Algorithm for Transportation Planning. Department of Civil Engineering, Massachusetts Institute of Technology, Cambridge, Res. Rept. R63-52, 1963.
9. W. Hoffman and R. Pavely. A Method for the Solution of the Nth Best Path Problem. Journal of the Association of Computing Machinery, Vol. 6, 1959, pp. 506-514.

Publication of this paper sponsored by Committee on Mineral Aggregates.

Soil Support Value—A New Horizon

GILBERT Y. BALADI AND TESFAI GOITOM

The soil support value of the American Association of State Highway Officials interim guide for the design of flexible pavement is given a new horizon. It is shown that the soil support scale can be expressed in terms of a normalized model. This model relates the dynamic load capacity of a subgrade soil to its static strength. The model was verified by using five different materials that ranged from gravel, sand, and clay to clayey silt.

The determination of a flexible pavement structural thickness (surface, base, and subbase) depends on two major factors--traffic and subgrade strength. Existing design procedures call for different subgrade strength parameters or strength-scaling factors [elastic modulus, resilient modulus, California bearing ratio (CBR), soil support value (SSV), etc.]. The American Association of State Highway Officials (AASHO) design method, in particular, uses a subgrade strength-scaling factor called an SSV. This factor was assigned an empirical scale with values from 3 to 10. Point 3.0 on the soil support scale represents the roadbed soils at the AASHO Road Test. As pointed out by the AASHO interim guide, the units of the SSV have no direct relationship to any procedure for testing soils. Therefore, it is necessary for each design agency to establish a correlation between SSV and some testing procedure before this guide can be used for flexible pavement design.

In this paper, it is shown that the empirical soil support scale is related to a significant physical property of the subgrade material in question. This relationship is independent of sample and test variables and it is unique in its nature for the particular subgrade material under consideration.

BACKGROUND

The basic design equation, developed from the results of the AASHO Road Test, is valid for one SSV, which represented the roadbed soils and the conditions that existed at the test site and during the time of test. Consequently, it was necessary to assume an SSV scale to accommodate the variety of soils that could be encountered at other sites (1,2). This led different highway engineers to assume different SSVs for the same subgrade materi-

als. Further, the assumed SSV bore no relationship to any of the subgrade physical parameters. This problem has led researchers, highway engineers, and several agencies and highway departments to develop several correlations relating the SSV to different test results. These correlations include the following:

1. Correlation between CBR and SSV: The Utah State Department of Highways (1) conducted several CBR tests on compacted samples of the AASHO Road Test roadbed soils, the crushed-stone base materials, and other soil types. An empirical logarithmic scale, shown in Figure 1, was then assumed to relate the CBR and the estimated SSV of these materials. The same correlation plotted on arithmetic scales is also shown.
2. Correlation between modulus of deformation and SSV: Chou (3) presented a procedure for subgrade evaluation to estimate the SSV. He conducted triaxial tests on subgrade soil samples at field densities and moisture contents. The moduli of de-

Figure 1. Correlation between SSV and CBR.

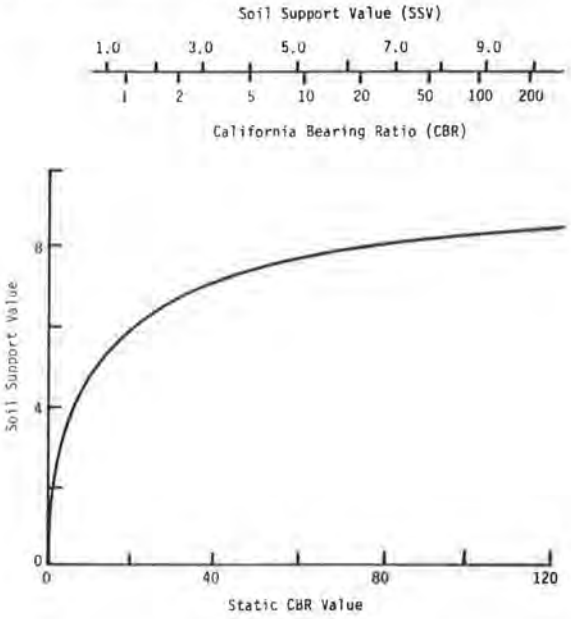

Figure 2. Design chart for terminal serviceability index of 2.5.

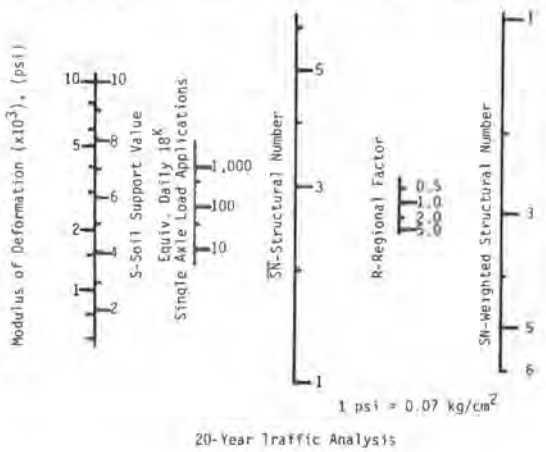

Figure 3. Correlation chart for estimating SSV.

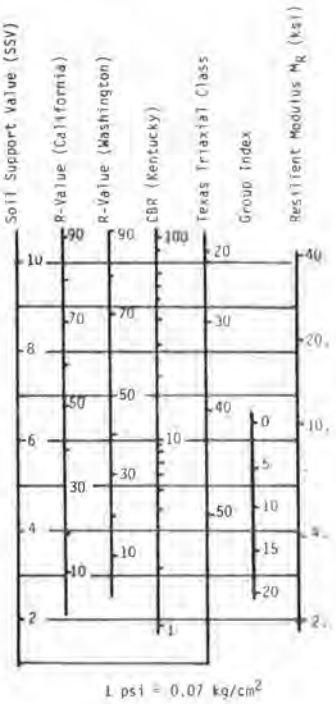

Figure 4. Resilient modulus versus SSV for recompacted and undisturbed cohesionless soils for first stress invariant of 15 psi.

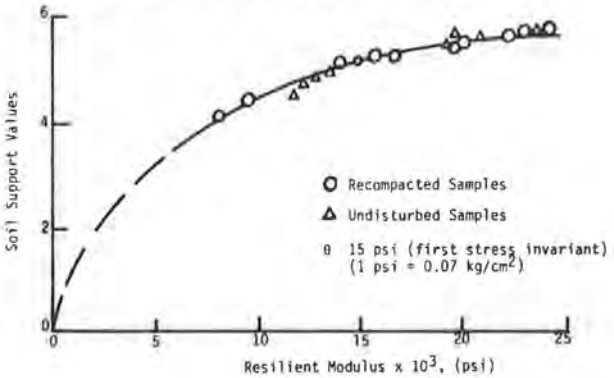

Figure 5. Average grain size distribution curves for Lorraine and Aberdeen subballast and under-tie materials.

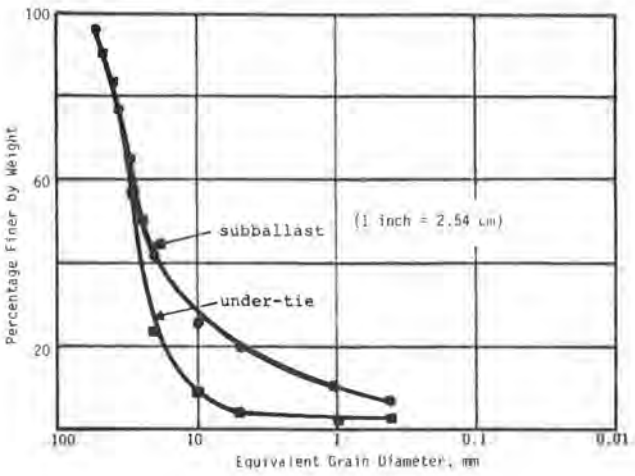

formation were then calculated and correlated to an assumed SSV scale as shown in Figure 2 (based on the AASHO interim guide except for the addition of the modulus of deformation scale).

3. Correlation between SSV and resilient modulus: Van Til and others (4) were among the first researchers to establish a correlation between the SSV and the resilient modulus of the subgrade soil at the AASHO Road Test. They used 40 000 psi (2812 kg/cm²) (a maximum value) as the resilient modulus of the crushed-stone materials and 3000 psi (211 kg/cm²) (a minimum value) as the resilient modulus of the AASHO A-6 subgrade soils. These two values were the limiting resilient modulus values on their scale, as shown in Figure 3. Van Til and others recommended that an effort be made to strengthen the validity of the soil support scale as new analytical tools and methods of characterizing material properties become available.

Based on a recommendation by Van Til and others, Baladi and Boker (5) developed a relationship between SSV and the resilient modulus of Michigan cohesionless soil. This relationship was dependent on the stress intensity and is given by the following equation:

$$SSV = 1.96 \log M_R + (M_R/19\,750) - 3.98 \quad (1)$$

where M_R is the resilient modulus.

Figure 4 shows this relationship for recompacted and undisturbed Michigan cohesionless subgrade soil tested under the first stress invariant (θ) of 15 psi (1.05 kg/cm²). Similar correlations were obtained for first stress invariants of 20 and 30 psi (1.4 and 2.1 kg/cm²).

TEST MATERIALS

Five different types of materials that ranged from gravel to silty clay soils were used in this study. The gradation curves of the test materials are shown in Figures 5 through 8. It should be noted that types one and three materials (under tie and subballast) were tested by J.T. Siller at the University of Massachusetts, Amherst (6). The other three materials were tested at Michigan State University under the direction of Baladi.

TEST RESULTS

All five types of materials were tested by using static and repeated-load triaxial tests. Figure 9 shows a typical plot of the logarithm of accumulated axial permanent strain as a function of the logarithm of the number of load repetitions (N) for samples consolidated under a confining pressure of 5 psi (0.35 kg/cm²) and tested by using different cyclic stress ratios. Typical results of the static tests are shown in Figure 10.

DISCUSSION

Lentz (7) and Lentz and Baladi (8-10) provided the technical guidance for the early phase of this work. They reported that the plastic strain of sand subgrade materials could be predicted by using triaxial test results. They concluded that the predic-

Figure 6. Grain size distribution of highway subgrade sand.

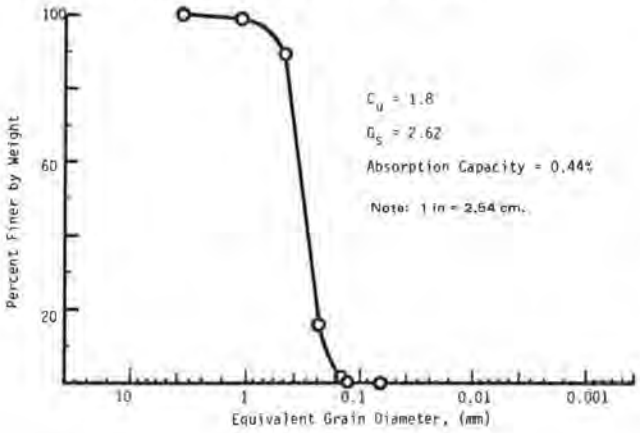

Figure 7. Grain size distribution curves for sites 1 and 2, Lower Peninsula.

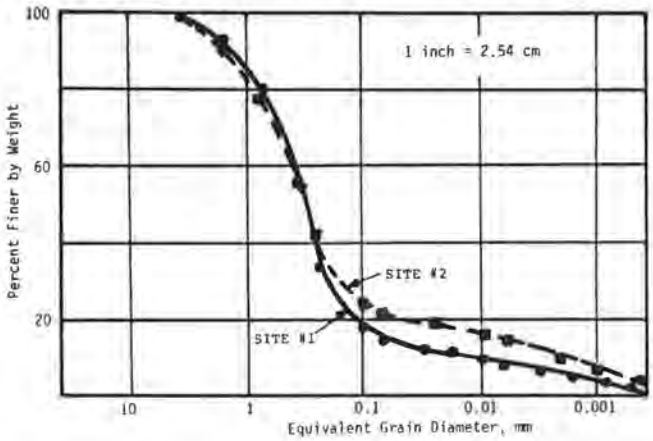

Figure 8. Grain size distribution curve for the AASHO roadbed soil.

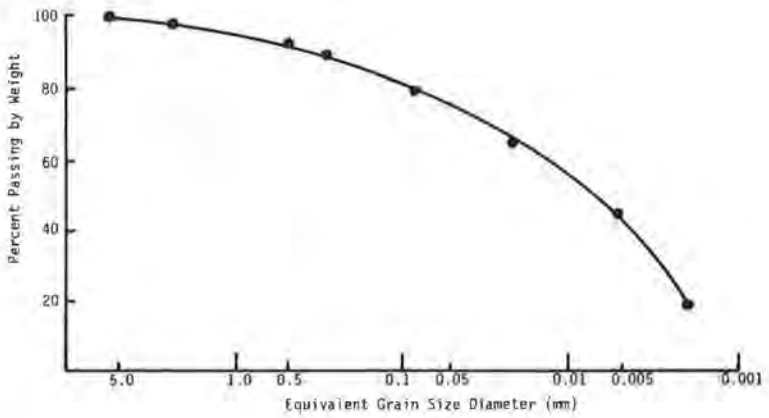

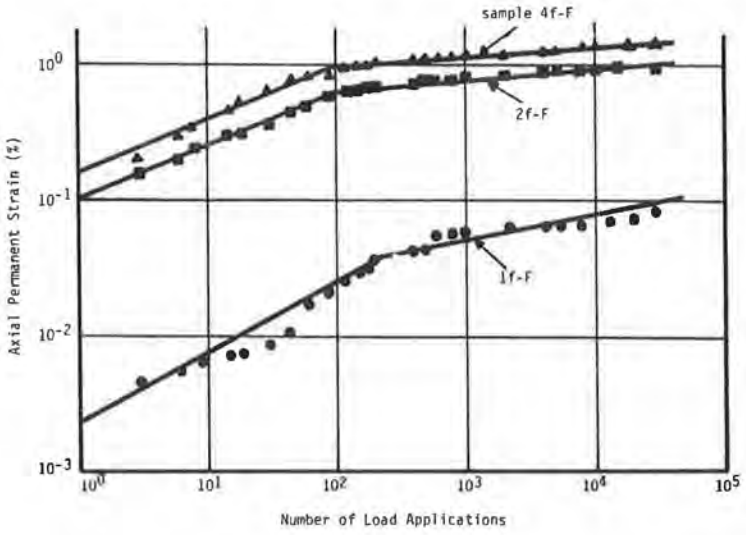

Figure 9. Typical axial permanent strain versus number of load applications (site 2, Lower Peninsula).

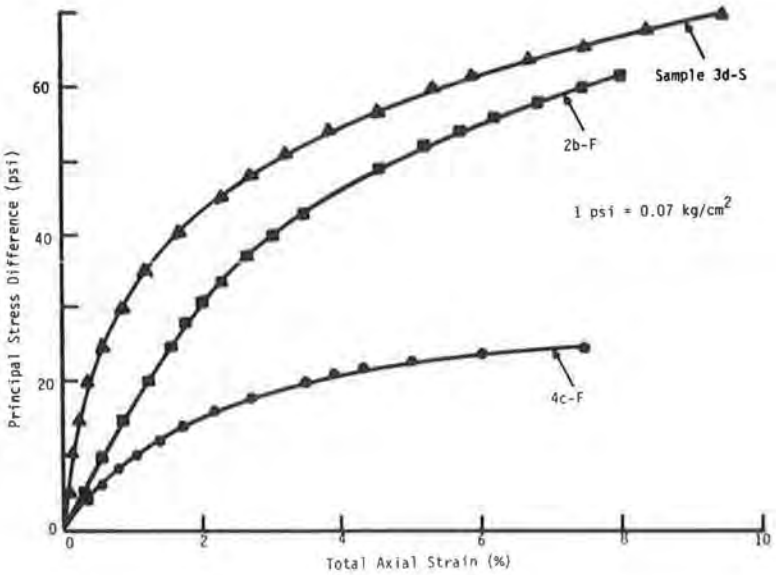

Figure 10. Principal stress difference versus total axial strain from incremental creep tests (site 2, Lower Peninsula).

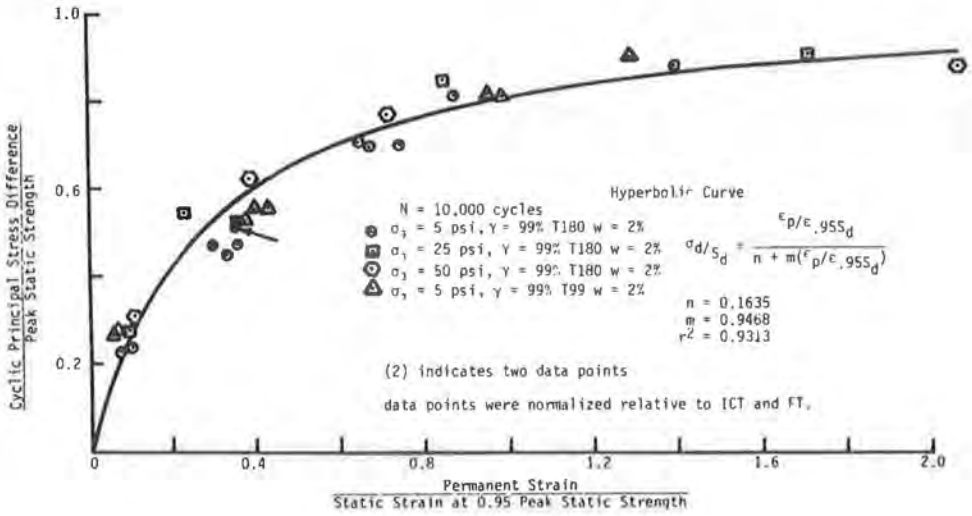

Figure 11. Normalized cyclic principal stress difference versus normalized permanent strain.

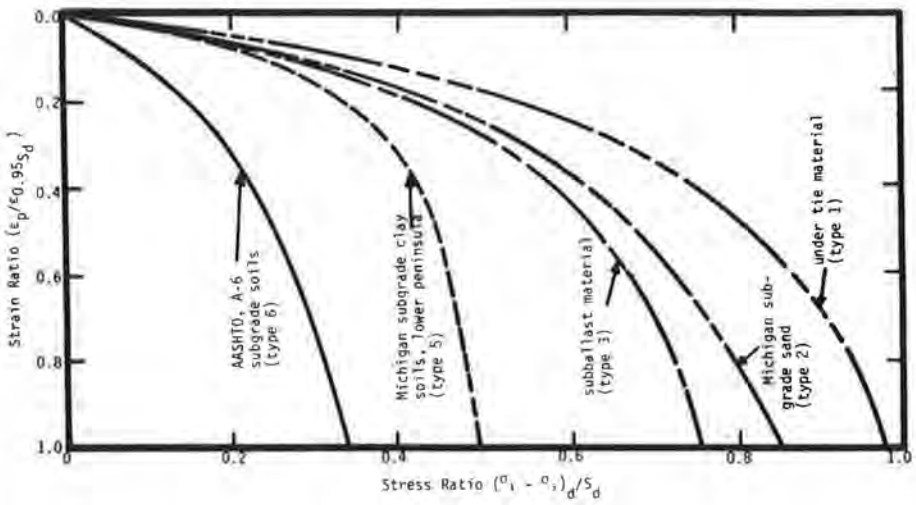

Figure 12. Normalized cyclic stress-strain ratio for five different materials subjected to 1 000 000 load repetitions.

tion model is dependent on the number of load applications and independent of the test variables (confining pressure, stress level) and sample variables (compaction effort and moisture content). They observed that the cyclic and static tests are highly dependent on the same test and sample variables. Consequently, they rationalized that the data from both tests could be normalized to minimize the effects of the sample and test variables. Their normalization process could be summarized as follows:

1. The cyclic principal stress difference $(\sigma_1 - \sigma_3)_d$ was expressed in terms of the peak static strength (S_d) of an identical soil sample tested under the same confining pressure by using static triaxial tests. [The term "static triaxial tests" indicates either incremental creep test, ramp test, or conventional triaxial test (11).]
2. The cumulative permanent strain (ε_p) at the desired number of load repetitions (N) was normalized relative to the static axial strain at 95 percent of the sample strength $(\varepsilon_{0.95S_d})$ of an identical sample tested under the same confining pressure by using the incremental creep test. Figure 11 shows their normalized data for a natural-sand deposit as well as that for manufactured sand (12). For more information on their data and normalization procedure, the reader is referred to a paper by Lentz and Baladi (9).

Figure 12 shows a plot of the normalized stress ratio as a function of the normalized strain ratio for all five materials. These normalized curves were modeled by using a hyperbolic function (Equation 1). As was expected, this function was found to be independent of confining pressure, principal stress difference, and water content:

$$\varepsilon_p/\varepsilon_{0.95S_d} = n/[S_d/(\sigma_1 - \sigma_3)_d] - m \quad (2)$$

where

ε_p = cumulative permanent strain at desired number of load repetitions;
$\varepsilon_{0.95S_d}$ = total axial strain at 95 percent of static strength;
S_d = static strength from incremental creep test, ramp test, or conventional triaxial test (5);
n,m = regression parameters; and
$(\sigma_1 - \sigma_3)_d$ = cyclic principal stress difference, density and water content.

The value of parameters n and m of Equation 2 is dependent only on material type and number of load repetitions.

Study of the AASHO interim guide has indicated that the SSV of one particular subgrade material is independent of lateral stress, stress level, water content, regional factor, and method of compaction. The SSV, however, is dependent only on the soil type. This could be restated as follows: the SSV of one material is fixed and constant unless some stabilizing agent is introduced and thus the soil type is changed. Indeed, the A-6 material, according to the AASHO soil classification, is assigned an SSV of 3.0. An SSV of 10.0 was assigned to the A-1 materials. These observations suggested that the physical parameter of the subgrade material to be related to the SSV should possess the following properties: (a) be independent of lateral stress; (b) be independent of stress level; (c) be independent of ambient and moisture conditions; (d) be independent of density, void ratio, and consolidation; and (e) be dependent only on soil type. To the best of our knowledge, such a physical parameter does not exist. Consequently, a new search to explain the SSV and relate it to a mathematical and/or physical model rather than one single parameter was initiated. The requirements of the model should be the same as those of the physical parameter.

At this time, the normalization process discussed above was finalized and proved to be valid for a wide range of materials. Recall that the normalized curve (stress ratio versus strain ratio) was found to be independent of (a) confining pressure; (b) stress level; (c) moisture content; and (d) density, void ratio, and consolidation; it was dependent on soil type and the number of load applications. These requirements appeared to be adequate except for the dependency of the normalized model on the number of load applications. These observations suggested that if the normalized model is fixed at a certain number of load repetitions (N = 1 000 000), it could be used to examine its relation to the SSV.

In reference to Figure 12, if it is assumed that for each soil type, failure occurs when the strain ratio reaches 100 percent, it follows that for the same number of load repetitions, a different stress ratio is required for different materials to fail. These stress ratios for the five materials in Figure 12 are 0.33 for A-6 subgrade soils, 0.49 for Michigan clay subgrade, 0.76 for the subballast materials, 0.85 for Michigan sand subgrade, and 0.98 for under-tie materials. These values could be obtained from Equation 2 by using a strain ratio of 1.0 and

solving for the stress ratio:

$$(\sigma_1 - \sigma_3)_d/S_d = 1/(n + m) \quad (3)$$

The value of the stress ratio of Equation 3 represents the dynamic load capacity that the soil in question can be subjected to so that failure will occur at 1 000 000 load repetitions. If the predesignated SSV is superimposed on the above data (SSV = 3.0 for A-6 soils and SSV = 10.0 for the under-tie materials), it follows that the SSV can be expressed by using the following equation:

$$SSV = 10\,[(\sigma_1 - \sigma_3)_d/S_d]_{(f,\,N=10^6)} = [10/(n + m)]_{(f,\,N=10^6)} \quad (4)$$

where the subscript (f, $N = 10^6$) indicates failure at 1 000 000 load applications. Equation 4 can be generalized as follows:

$$SSV = \alpha\,[(\sigma_1 - \sigma_3)_d/S_d]_{(f,\,N)} = [\alpha/(n + m)]_{(f,\,N)} \quad (5)$$

where α is constant depending on the number of load repetitions (N) and the subscript (f, N) indicates failure at N load applications.

CONCLUSIONS

A normalized and predictive model of the plastic strain of pavement materials was developed. The ability of the model to evaluate and predict the plastic behavior of several materials subjected to cyclic loading had previously been demonstrated. In this paper, a new understanding of the AASHO SSV scale is presented and it is based on the developed normalized and predictive model. A correlation between the SSV and the ratio of dynamic stress to static strength of the soil in question is shown.

ACKNOWLEDGMENT

We wish to acknowledge the Michigan Department of Transportation and the Federal Highway Administration for their financial assistance and support during the course of this investigation. The contents of this paper reflect our views and opinions and do not necessarily reflect the official view or policy of the sponsoring agencies.

REFERENCES

1. Committee on Design. AASHO Interim Guide for Design of Pavement Structures 1962. AASHO, Washington, DC, 1962.
2. The AASHO Road Test. HRB, Special Rept. 61E, 1962.
3. V.T. Chou. Analysis of Permanent Deformation of Flexible Airport Pavements. U.S. Army Corps of Engineers Waterways Experiment Station, Vicksburg, MI, Tech. Rept. S-77-8, 1977.
4. C.J. Van Til, B.F. McCullough, B.A. Vallerga, and R.G. Hicks. Evaluation of AASHO Interim Guides for Design of Pavement Structures. NCHRP, Rept. 128, 1972.
5. G.Y. Baladi and T.D. Boker. Resilient Characteristics of Michigan Cohesionless Roadbed Soils in Correlation to the Soil Support Values. Division of Engineering Research, Michigan State Univ., East Lansing, Final Rept., 1978.
6. J. Siller. Properties of Railroad Ballast and Subballast for Track Performance Prediction. Univ. of Massachusetts, Amherst, 1980.
7. R.W. Lentz. Permanent Deformation of Cohesionless Subgrade Material Under Cyclic Loading. Michigan State Univ., East Lansing, Ph.D. dissertation, 1979.
8. G.Y. Baladi and others. Shear Strength of Cohesionless Soils. ASTM Special Publ. STP 740, Sept. 1981.
9. R.W. Lentz and G.Y. Baladi. Simplified Procedure to Characterize Permanent Strain in Sand Subjected to Cyclic Loading. Proc., International Symposium on Soil Under Cyclic and Transient Loading, Swansea, Great Britain, 1980.
10. R. Lentz and G.Y. Baladi. Permanent Deformation of Cohesionless Subgrade Material Under Cyclic Loading. Proc., International Symposium of Soil Under Cyclic and Transient Loading, Swansea, Great Britain, 1980.
11. G.Y. Baladi and T. Goitom. The Resilient and Plastic Characteristics of Michigan Subgrade Soils and Their Soil Support Values. FHWA, Final Rept. MI-RD-80-02, 1981.
12. G.Y. Baladi. Mechanistic Pavement Deformation Model for Unbounded Pavement Materials. FHWA, Rept. FHWA/RD-82/029, 1982.

Publication of this paper sponsored by Committee on Mechanics of Earth Masses and Layered Systems.

The **Transportation Research Board** is an agency of the National Research Council, which serves the National Academy of Sciences and the National Academy of Engineering. The Board's purpose is to stimulate research concerning the nature and performance of transportation systems, to disseminate information that the research produces, and to encourage the application of appropriate research findings. The Board's program is carried out by more than 270 committees, task forces, and panels composed of more than 3300 administrators, engineers, social scientists, attorneys, educators, and others concerned with transportation; they serve without compensation. The program is supported by state transportation and highway departments, the modal administrations of the U.S. Department of Transportation, the Association of American Railroads, the National Highway Traffic Safety Administration, and other organizations and individuals interested in the development of transportation.

The National Research Council was established by the National Academy of Sciences in 1916 to associate the broad community of science and technology with the Academy's purpose of furthering knowledge and of advising the federal government. The Council operates in accordance with general policies determined by the Academy under the authority of its Congressional charter, which establishes the Academy as a private, nonprofit, self-governing membership corporation. The Council has been the principal operating agency of both the National Academy of Sciences and the National Academy of Engineering in the conduct of their services to the government, the public, and the scientific and engineering communities. It is administered jointly by both Academies and the Institute of Medicine.

The National Academy of Sciences was established in 1863 by Act of Congress as a private, nonprofit, self-governing membership corporation for the furtherance of science and technology, required to advise the federal government upon request within its fields of competence. Under its corporate charter, the Academy established the National Research Council in 1916, the National Academy of Engineering in 1964, and the Institute of Medicine in 1970.